Computer-Aided Understanding of Perturbations in Soft Matter Systems

Betul Uralcan

A Dissertation
Presented to the Faculty
of Princeton University
in Candidacy for the Degree
of Doctor of Philosophy

Recommended for Acceptance
by the Department of
Chemical and Biological Engineering
Adviser: Professor Pablo G. Debenedetti

January 2019

© Copyright by Betul Uralcan, 2019.

All rights reserved.

Abstract

This dissertation aims to advance the fundamental knowledge on the structure and dynamics of condensed matter, focusing on systems relevant to emerging problems in biotechnology and energy. We aim to do this using tools and techniques derived from statistical mechanics with the aid of computer simulations, and when appropriate, combined with principles from experimental science.

In the first part, we study the effects of solution composition on the electrochemical response of a double layer capacitor using electrical impedance spectroscopy measurements and molecular dynamics simulations in a constant potential ensemble. We find that capacitance first increases with ion concentration following its expected ideal solution behavior but decreases upon approaching the pure ionic liquid limit.

In the second part, we use atomistic replica-exchange molecular dynamics simulations and thermodynamic analysis to investigate the effects of ionic liquid-induced perturbations on the folding/unfolding thermodynamics of the Trp-cage miniprotein, and compare our findings to circular dichroism measurements. We find that ionic liquid-induced denaturation resembles cold unfolding, where unfolded states are populated by compact, partially folded structures in which elements of the secondary structure are conserved, while the tertiary structure is disrupted.

In the third part, we perform a fully atomistic computational study of Trp-cage in explicit water, and construct the complete stability diagram in the (P,T) plane. At ambient temperature, we find that application of pressure shifts the equilibrium of conformational states towards denaturation. Below 250K, the stability of the native fold depends non-monotonically upon pressure. Our simulations also show while cold unfolding and thermal denaturation mechanisms differ significantly at ambient pressure, they exhibit progressive similarity at elevated pressures.

In the final part, we consider three commonly used molecular water models (ST2, TIP4P/2005, and TIP5P) that support the existence of the metastable liquid-liquid

transition. We demonstrate that a corresponding-states-like rescaling of pressure and temperature results in a significant degree of universality in the pattern of thermodynamic response function extrema. We also report an intriguing correlation between the location of the liquid-liquid critical point, the density extrema locus, and the liquid-vapor stability limit, and demonstrate a similar correlation for two theoretical models.

Acknowledgements

There are many people and many events that have led to my choosing and pursuing this path. Chemical engineering may not sound like a field, which can arouse passion or excitement in most people, but for me it has been more than just luck which has carried me to this point, to a field and a career so well-suited to my life and personality. I could attribute my decision to pursue an academic career in chemical engineering foremost to my father, who was my hero growing up, and to my mother whose unconditional love and support gave me the courage to follow my dreams. I am enormously grateful for the individuals who have supported me throughout my studies. To those named here and many others, thank you. I could not have made it without you.

First and foremost, I thank my advisor Professor Pablo G. Debenedetti, who has guided and mentored me throughout my graduate studies, helped me through many important decisions and milestones, which were crucial to both my professional and personal development. I have greatly benefited from his relaxed yet attentive approach to advising which allowed me to discover my interests and capabilities, and also to have a formative and productive PhD experience. Pablo was able to provide considerable amounts of time to discuss research with me, even with the time consuming demands of his administrative position. When I joined the PGD group as a second year graduate student, he blocked chunks of his time to give me an intensive Introduction to Statistical Mechanics course, which helped me immensely during the transition process to his group. For me, and for many others who have been lucky enough to interact with him, Pablo is and will always be a role model as a passionate researcher, skillful manager and a caring, genuine person who touches the lives of people with small acts of kindness and understanding. For me, Pablo is also the person to look up to when I have to identify challenges and make important

decisions. I will try to benefit from his wisdom by asking "What would Pablo say?" in tough situations throughout my life.

I am also very grateful to Professor Mikhail Anisimov, with whom I had the privilege to collaborate on a project. I very much appreciated Mikhails hands-on approach to mentorship, and I have learned a lot through my interactions with him. Professor Anisimov is an exceptional person and scientist, and I am extremely appreciative of all the time, advice and knowledge he shared with me. I would like to send special thanks also to David T. Limmer who has been an unocial mentor throughout my graduate studies. David always provided me with guidance and mentorship for my research and career, even after he left Princeton. I thank Professor Ilhan Aksay for his mentorship throughout the initial stages of my PhD as my co-advisor whose passion and enthusiasm have continued to motivate and inspire me. I would like to also acknowledge late Professor Christodoulos Floudas and the CASL group members with whom I had the privilege to work for a short time. I would like to also thank my committee members Robert K. Prudhomme and Thanos Panagiotopoulos for their questions, insight and guidance over the years.

I would like to acknowledge PGD lab members (Dan Kozuch, Gul Zerze, Amir Haji-Akbari, Sang Beom Kim, Elia Altabet, Rakesh Singh, Folarin Latinwo, Navaid Khan, Wick Hatch, Frankie Ricci, Joey Vella, Andreia Fenley), CML group (Daniel Dabbs, D.J. Bozym, Michaleis Aliferakis, Kevin Sallah, Michael Bozlar, Valerie Alain, Nicholas Szamreta) and our affiliate AZP group members for helping shape my experience as a graduate student. Thank you for, well, far too much to mention here. Suffice it to say that you enriched and enlivened my graduate school experience. Our discussions and interactions stimulated my mind and often sparked ideas which led me on the paths to scientific discovery. Your presence served as a pleasant distraction, when I was in need. I would like to offer special thanks to Gul and Dan for their fun company. I am especially grateful to Amir Haji-Akbari, who was a post-doctoral as-

sociate at PGD group and is now professor at Yale University. Amir has been always there for me to provide support and guidance on personal and academic matters.

I am thankful to all CBE administrative staff for helping me navigate the bureaucracy of administrative procedures. I am particularly indebted to Karen Oliver, a de-facto member of every research group in CBE, for being available to chat about anything and resolving all problems with her magic wand! Eric Paul and the Princeton Institute for Computational Science and Engineering (PICSIE) staffs were incredibly helpful in managing the computer clusters (Therminator and TIGRESS) that were essential to my dissertation research. I am also extremely grateful to the Facilities personnel for keeping up with our endless demands from the basement of A-wing. Whenever we had a maintenance issue in our ghost town, they dropped what they were doing immediately and resolved our problems.

I am indebted to my Princeton family, for their enduring companionship and support during my Ph.D. First, I would like to thank the Kortan family (Vildan Teyze, Refik Amca, Burcu and Deniz) for being there for me all the time. Tammy and Arif uncle, thank you for making me feel at home and for putting up with me during my final lap as a graduate student. I would not be able to make it here if it was not for Arif uncles endless supply of chocolate truffles, and Tammys healthy meals that balance out the bad stuff.

Alisya, Amanda, Anusha/Shahan, Dana, Deborah, Dwayne/Nick, Elif, Emre, Kamal/Rashda/little friends, Kubra, Lian, Melissa, Michaleis, Mohammad, Nadia, Nadirah, Orooj/Saud/Idris, Sarah and Zuby/Faizan/Aayan, thank you for your refreshing company outside the confines of my office. You have made my graduate school experience in the bubble so fulfilling: I am too lucky to have been given the opportunity to share my experiences with you. Nadirah, Sheeba, Sarosh, Cyrus and Ammara, I just can not wait to meet you in Istanbul!

My decision to pursue a PhD would not have been possible had it not been for my experience at Bogazici University. Bogazici has been not only an educational institute but also a home for me throughout my undergraduate studies. Along the way, I have been blessed with incredible mentors, teachers, colleagues, and friends (sometimes individuals have come to fit all four roles!). I send great many thanks to all of my professors whose commitment to excellence in teaching helped me maximize my potential. I owe much gratitude to Turkan Haliloglu, Kerem Uguz, Burak Alakent, and Ahmet Kerim Avci, professors of chemical engineering, who all inuenced me in different ways, and (among many things) gave me the confidence that going to graduate school was something I could commit myself to. I am especially grateful to Professor Ramazan Yildirim for introducing me to the passion of research, for giving me a shot at new experiences and opportunities (too much to list here) that I believe quiet literally altered the trajectory of my life.

Most of all, I would like to thank my family for their unconditional love and support for I am truly blessed to have you in my life. Busra, thank you for teaching me how to be kind, Beyza thank for your showing me what it means to be brave. Thank you both for reminding me to stay true to myself. Anne and Baba, thank you for every sacrifice you have made in order for me to reach this point. You are the kindest, most generous, loving people I know, and I can cofidently say that if there is any good in me today, it is because of you. Your love, passion, and enthusiasm have always inspired and motivated me more than anything else. I am wholeheartedly grateful to you, without whom none of my accomplishments would have been possible. Thank you for believing in me and supporting me to follow my heart and dreams. You are my role models, and I am so lucky to have you as my parents.

Dedicated to my parents and sisters with love.

Contents

Abstract iii

Acknowledgements v

List of Tables xiv

List of Figures xv

1 Introduction **1**

1.1 Electrolytes at Charged Interfaces 3

1.1.1 Electrical Double Layer for Dilute Electrolytes 4

1.1.2 Preliminary Studies to Incorporate Steric Constraints and Polarizability 7

1.1.3 Electrical Double Layer for Neat Room Temperature Ionic Liquids 7

1.1.4 Electrical Double Layer for Concentrated RTIL Solutions . . . 11

1.2 Protein Stability under Environmental Perturbations 12

1.2.1 Conformational Space of Proteins 12

1.2.2 Globular Proteins are Marginally Stable 13

1.2.3 Protein Folding 16

1.3 Liquid Water's Anomalies 18

2 Concentration Fluctuations and Capacitive Response in Dense Ionic Solutions **22**

2.1 Introduction 22

2.2 Results and Discussions 26
2.3 Conclusions 37
2.A Appendix 38
2.A.1 Simulation Details 38
2.A.2 Capacitance as a Continuous Function of Electrode Potential . 39
2.A.3 Bulk Charge Density 40

3 A Computational Study of the Ionic Liquid-Induced Destabilization of the Miniprotein Trp-Cage 42
3.1 Introduction 42
3.2 Methods 46
3.2.1 Computational Methods 46
3.2.2 Experimental Methods 51
3.3 Results and discussion 52
3.4 Conclusions 62
3.A Appendix 63
3.A.1 Convergence of REMD Simulations 63
3.A.2 Order Parameter for the Selection of Folded/Unfolded States . 64
3.A.3 Determination of the Representative Configurations 64
3.A.4 Analysis for [EMIM][Act] Systems 65

4 Computational Investigation of the Effect of High Pressure on Protein Stability 67
4.1 Introduction 67
4.2 Results and Discussions 70
4.2.1 Thermodynamics of Trp-cage 70
4.2.2 Pressure- and Temperature-Induced Effects on the Folding Landscape of Trp-cage 75

4.2.3 Conclusions 79
4.A Appendix 79
4.A.1 Simulation Details 79
4.A.2 Structural Analysis 82
4.A.3 Thermodynamic Analysis 83
4.A.4 Salt Bridge Profiles 85
4.A.5 Trp-cage's α-helical propensity 86
4.A.6 Hydrogen Bond Profiles 86

5 Pattern of Property Extrema in Supercooled and Stretched Water Models and a New Correlation for Predicting the Stability Limit of the Liquid State 90
5.1 Introduction 90
5.2 Results and discussion 93
5.2.1 Searching for Universality in the Pattern of the Property Extrema 93
5.2.2 Correlation with the Stability of the Liquid State 101
5.3 Conclusions 104
5.A Appendix 105
5.A.1 Simulation Details 105
5.A.2 Rescaling Analysis 114
5.A.3 Lattice-gas model 115

6 Concluding Remarks 118
6.1 Concentration Fluctuations and Capacitive Response in Dense Ionic Solutions 118
6.2 A Computational Study of the Ionic Liquid-Induced Destabilization of the Miniprotein Trp-Cage 120
6.3 Computational Investigation of the Effect of Pressure on Protein Stability 122

6.4 Pattern of Property Extrema in Supercooled and Stretched Water Models and a New Correlation for Predicting the Stability Limit of the Liquid State 124

Bibliography **127**

List of Tables

2.1 Force-field parameters for the electrolyte and the electrode 39

3.1 Fraction of the structures that belong to the main cluster of a free energy basin 65

5.1 Critical temperature (T_c) and pressure (P_c) for the water models . . 114

5.2 Rotation angle (θ) 114

List of Figures

1.1 Classical models of the electrical double layer 4

1.2 Probability distribution of the total charge Q on the electrodes . . . 8

1.3 Free energy surface of a protein as a function of rmsd and R_g 14

1.4 Example of a protein folding energy landscape 17

1.5 Schematic representation of waters anomalies at atmospheric pressure 20

2.1 Differential capacitancepotential curves of the GCelectrolyte interface 23

2.2 Capacitance as a function of ion concentration and potential for the charge-frustrated Ising model 25

2.3 Simulated capacitor 26

2.4 Capacitance as a function of ion fraction and potential 28

2.5 Composition dependence of electrolyte-electrode charge correlations . 31

2.6 Charge density correlation length as a function of ion concentration . 33

2.7 Ion surface adsorption free energies 36

2.A.1 Probability distribution of the total charge Q on the electrodes . . . 40

2.A.2 Charge density correlation length profile 41

3.1 Stability diagram of Trp-cage in (C-T) plane 52

3.2 Temperature dependence of fraction of folded Trp-cage from REMD and CD measurements 53

3.3 Temperature dependence of helix fraction of Trp-cage from REMD and CD measurements 54
3.4 Free energy change of unfolding for Trp-cage as a function of temperature and [Gdm][Act] concentration 55
3.5 Enthalpic and entropic contributions to the free energy change of unfolding for Trp-cage as a function of temperature and [Gdm][Act] concentration 56
3.6 The free energy surfaces associated with the order parameters Cα rmsd and W6-S14 distance as a function of solvent composition . . . 57
3.7 The free energy surfaces associated with the order parameters Cα rmsd and W6-S14 distance for (a) 230 K, and (b) 465 K at 0 M . . . 58
3.8 Probability distribution of (a) distance between residues W6 and S14 (1/nm), and (b) solvent accessible surface area (1/nm^2) at 300 K . . 59
3.9 Average number of water molecules (N_w), acetate ions (N_{Act}), and guanidinium ions (N_{Gdm}) within 0.4 nm of each residue at 300 K . . . 60
3.10 Probability distribution of the distance between salt bridge forming residues D9 and R16 at 300 K 60
3.11 Probability distribution of the number of (a) protein-protein, (b) protein-water, (c) protein-acetate, and (d) protein-guanidinium H-bonds at 300 K 61
3.A.1 Convergence of fraction of folded protein profiles 63
3.A.2 Probability distribution of (a) Cα rmsd (b) W6S14 distance at 300K 64
3.A.3 Fraction of folded Trp-cage as a function of temperature and [EMIM][Act] concentration 65
3.A.4 The free energy surfaces associated with the order parameters Cα rmsd and α-helix rmsd 66

4.1 Equilibrium folded fraction as a function of temperature 71

4.2 Stability diagram of Trp-cage in the (P,T) plane, obtained from simulation data 72
4.3 The free-energy change upon unfolding, and the corresponding enthalpic and entropic ontributions, as a function of temperature 73
4.4 The free energy surfaces associated with the order parameters Cα rmsd and W6-S14 distance 75
4.5 The change in solvent accessible surface area upon unfolding ($\Delta SASA_{\mathrm{u}}$) and the change in the number of water molecules around residue W6 upon unfolding (ΔNw_{u}) 78
4.A.1 REMD Simulation Convergence Tests 82
4.A.2 Order parameters for the selection of folded/unfolded states 84
4.A.3 Equilibrium folded fractions as a function of temperature 85
4.A.4 Equilibrium folded fractions as a function of temperature 86
4.A.5 Decomposition of the energy change upon unfolding. 87
4.A.6 Probability distribution of the distance between salt bridge-forming residues D9 and R16 88
4.A.7 The α-helical propensity of residue L2 88
4.A.8 Probability distribution of the number of H-bonds formed between water and (a) nonpolar amino acids (NonpolarAA), (b) polar amino acids (PolarAA) in Trp-cage 89
4.A.9 The free-energy surface associated with the order parameters Cα rmsd and W6S14 distance at 1 bar, 417.5K 89

5.1 Generic phase diagram for a polyamorphic fluid 93
5.2 Extrema lines of various thermodynamic properties 95
5.3 Extrema lines of various thermodynamic properties in the rescaled coordinates 96

5.4 The correlation between the location of the liquid-liquid critical points, the loci of density extrema and liquid stability lines in rescaled coordinates for water models 99
5.5 The correlation between the location of the liquid-liquid critical point, the locus of density extrema, and the liquid-vapor spinodal (LVS) upon tuning the location of the liquid-liquid critical point for the two-state van der Waals model 102
5.A.1 Density along isobars for the TIP5P water model 106
5.A.2 Isothermal compressibility (κ_T) along isobars for the TIP5P water model 107
5.A.3 Isobaric heat capacity (C_P) as a function of pressure along isotherms for the TIP5P water model computed from NPT simulations 108
5.A.4 Extrema of various thermodynamic properties for the TIP5P water model 109
5.A.5 Pressure as a function of temperature along isochores for the TIP5P water model 110
5.A.6 Extrema of various thermodynamic properties for the TIP4P/2005 water model 111
5.A.7 Extrema of various thermodynamic properties for ST2 water model . 112
5.A.8 Extrema lines of various thermodynamic properties in the rescaled coordinates T' and P' for water models 113
5.A.9 Consistency of computed liquid-vapor stability limits with the linear correlations between Δc and Δs 115
5.A.10 The correlation between the location of the liquid-liquid critical point, patterns of extrema and liquid vapor spinodal upon tuning the location of the liquid-liquid critical point for the lattice-gas model . . 116

5.A.11 The correlation between the location of the liquid-liquid critical point, patterns of extrema and liquid vapor spinodal upon tuning the location of the liquid-liquid critical point for the lattice-gas model . . 117

Chapter 1

Introduction

The liquid electrolyte in the battery of our smartphones (ionic liquids), the insulin pump used for a diabetic patient (biotherapeutics), the bacteria that reproduce in the rice from yesterdays meal (thermophilic proteins) are all common examples of condensed matter. We have made significant progress in understanding the isolated bulk behavior of these materials. However, their rational design and optimization for practical applications rely on gaining a fundamental level understanding of how these materials behave in complex environments: where environmental perturbations alter their response, the material itself perturbs its environment, and the interplay between these coupled interactions give rise to interesting behavior. This poses new questions to our understanding. This dissertation aims to advance the current fundamental knowledge on the structure and dynamics of condensed matter, focusing on systems relevant to emerging problems in biotechnology and energy. We aim to do this using tools and techniques derived from statistical mechanics with the aid of computer simulations, and when appropriate, combined with principles from experimental science.

This dissertation contains four chapters each of which constitute a self-contained study. The four chapters may be divided into three specific topics: capacitive response at electrode/electrolyte interfaces, thermodynamics and mechanisms of protein fold-

ing/unfolding, and liquid water under environmental perturbations. In Chapter 2, we report an anomalous capacitance enhancement upon dilution of dense ionic solutions using electrochemical impedance spectroscopy, and provide a fundamental basis for this observation using a coarse-grained model to relate structural variations at the double layer to the occurrence of the maximum. Then, using molecular simulations, we develop a framework to study the effects of solution composition on the electrochemical response of the electrical double layer. These results provide insights into the microscopic mechanisms that determine the electronic properties of the interface and enable means to examine how molecular features such as polarity, size, and shape affect the electrochemical response. In Chapter 3, we perform replica-exchange molecular dynamics simulations and use thermodynamic analysis to elucidate the effects of ionic liquid-induced perturbations on the stability of an α-helical globular protein, Trp-cage. In Chapter 4, we construct the complete stability diagram of the miniprotein Trp-cage by employing extensive fully atomistic replica exchange molecular dynamics simulations, and elucidate the effect of pressure and temperature perturbations on its folding/unfolding mechanisms. In Chapter 5, we analyze simulation results of water models that support the existence of a metastable liquid-liquid transition, and demonstrate that a corresponding-states-like rescaling of the thermodynamic property extrema of these models results in a significant degree of universality.

The remainder of this chapter provides the background and motivation for the topics considered in this thesis (capacitive response at electrode/electrolyte interfaces in Section 1.1, thermodynamics and mechanisms of protein folding/unfolding in Section 1.2, and water under environmental perturbations in Section 1.3). The chapters that follow are based in full or in part on the following publications:

- David J. Bozym, Betul Uralcan, David T. Limmer, Michael A. Pope, Nicholas Szamreta, Pablo G. Debenedetti, and Ilhan A Aksay. "Anomalous capacitance

maximum of the glassy carbonionic liquid interface through dilution with organic solvents." *J. Phys. Chem. Lett.*, **6(13)**, 2644-2648, 2015. [**Chapter 2**]

- Betul Uralcan, Ilhan A. Aksay, Pablo G. Debenedetti, and David T. Limmer. "Concentration fluctuations and capacitive response in dense ionic solutions." *J. Phys. Chem. Lett.*, **7(13)**, 2333-2338, 2016. [**Chapter 2**]

- Betul Uralcan, Sang Beom Kim, Chester E. Markwalter, Robert K.Prudhomme, and Pablo G. Debenedetti. "A computational study of the ionic liquid-induced destabilization of the miniprotein Trp-cage." *J. Phys. Chem. B*, **122(21)**, 5707-5715, 2018. [**Chapter 3**]

- Betul Uralcan, Pablo G. Debenedetti, "Computational investigation of the effect of high pressure on protein stability." (preprint available 2018). [**Chapter 4**]

- Betul Uralcan, Folarin Latinwo, Pablo G. Debenedetti, Mikhail Anisimov, "The pattern of property extrema in supercooled and stretched water models as a tool to predict the stability limit of the liquid state." (preprint available 2018). [**Chapter 5**]

1.1 Electrolytes at Charged Interfaces

Electrical double layers (EDLs) form at the interface of a fluid in contact with another phase, often a solid electrode[1]. The structure of the electrolyte at the EDL is considerably different than that of a bulk solution since the surface disrupts the electrolyte solution. The properties of the interface between a charged surface and an electrolyte plays a major role in energy storage applications[2]. Particularly, the potential distribution in the EDL and its response to charging determines the ca-

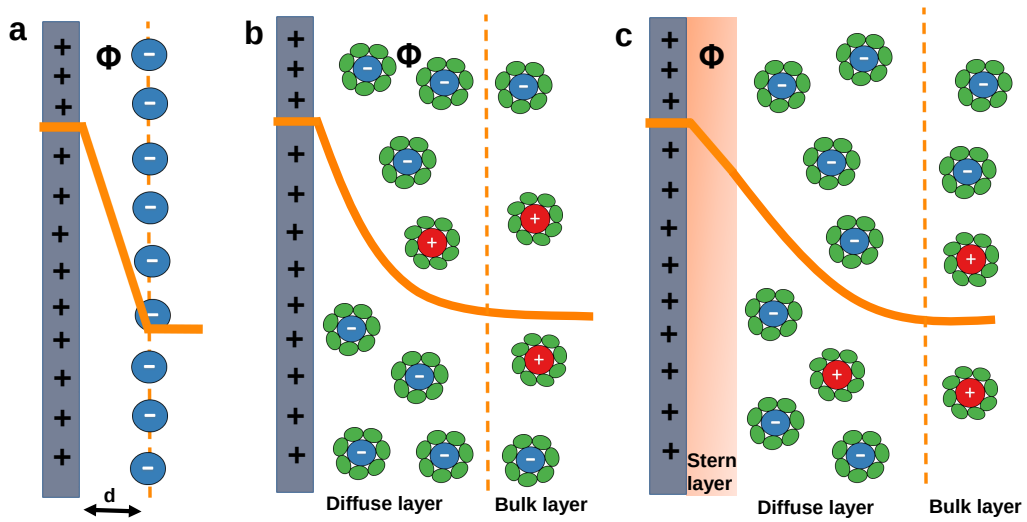

Figure 1.1: (a) Helmholtz, (b) Gouy-Chapman, and (c) Stern model of the electrical double-layer formed at a positively charged electrode in an aqueous electrolyte. The Stern layer marks the distance of closest approach of the ions to the charged surface. Blue, red and green spheres represent anions, cations, and solvent molecules, respectively.

pacitance of the electrode/electrolyte interface, thereby, the ability to store energy. Consequently, many models have been put forward to explain the EDL structure.

Below we provide a brief overview of the models that describe charge and potential disribution in electrolytes at the EDL. First, we present the classical electrical double layer theories for dilute electrolytes. Second, we give a brief overview on neat room temperature ionic liquids (RTILs) at solid/electrolyte interfaces. Finally, we discuss the relevance of concentrated ionic solutions in energy storage applications and the gap in the literature on understanding their properties at charged surfaces. These will form the basis for our work on the capacitive response of concentrated ionic solutions in Chapter 2.

1.1.1 Electrical Double Layer for Dilute Electrolytes

Helmholtz Model In an effort to understand EDLs, analytical continuum models have been developed to describe the electrode/electrolyte interface. The first EDL

model was developed in the context of ordinary dilute ionic solutions by Helmholtz[3]. In this model, the EDL is analogous to a plane dielectric capacitor. Assuming that counterions form the second plate of the capacitor to shield the charge on the electrode surface, the double layer capacitance in the Helmholtz model is given by

$$C_d^H = \frac{\epsilon *}{4\pi d} \tag{1.1}$$

where d is the distance between the plates and ϵ^* is the effective dielectric constant of the medium between them. The potential decays linearly over a distance equal to the closest approach of counterions as depicted in Figure 1.1(a).

Gouy-Chapman Model Although Helmholtz's model was ground-breaking at the time, it contained an intrinsic flaw as the model did not account for entropic considerations that would not allow the EDL to be one layer thick. In the early twentieth century, Gouy proposed that the ions in solution form a three-dimensional diffuse cloud of anions and cations[4] with a net charge equal and opposite to the charge at the surface of the electrode(Figure 1.1(b)). Chapman[5] developed this model into the Poisson−Boltzmann theory of diffuse EDL given by

$$C_d^{GC} = \left(\frac{\epsilon}{\lambda_D}\right) cosh\left(\frac{ze(\Phi_H - \Phi_s)}{2kT}\right) \tag{1.2}$$

where z is the ionic valence, e is the electric charge, c_o is the bulk ion concentration, ϵ is the solvent dielectric constant, Φ_H is the potential at the surface, and Φ_s is the bulk electrolyte potential. λ_D, the Debye length, is the characteristic length over which the potential decays from Φ_H at the wall to Φ_s in the bulk, and is given by

$$\lambda_D = \sqrt{\frac{\epsilon kT}{2z^2e^2c_o}} \tag{1.3}$$

The Gouy-Chapman model suggests a parabolic capacitance curve as a function of electrode potential(Figure 1.1(b)) and overestimates the double layer capacitance. In this model, the ions are treated as point-charges. Thus, the concentration of counterions near the surface reaches unphysical values when the surface potential is increased, and, consecutively, the model breaks down at high potentials. Equation 1.2 and 1.3 also show that the double layer capacitance increases with bulk ion concentration ($C_d^{GC} \propto \sqrt{c_o}$). This relation is important for Chapter 2 where we will discuss how this relation manifests itself in concentrated RTIL solutions.

Gouy-Chapman-Stern Model The problem of overestimating the capacitance was not solved until the early 1920s when Stern proposed a model combining the Helmholtz and Gouy-Chapman models[6]. In Stern's model, as the surface potential increases, a subset of ions adheres to the surface in an analogous form to the Helmholtz model, this prevents the capacitance from reaching unphysically large values. In particular, the potential is given by a piecewise function that has a linear component for the Stern layer and an exponentially decaying component for the diffuse layer (Figure 1.1(c)). The Gouy-Chapman-Stern (GCS) capacitance is given by the relationship

$$\frac{1}{C_d^{GCS}} = \frac{1}{C_d^{H}} + \frac{1}{C_d^{GC}} \tag{1.4}$$

where the smaller of the two capacitances dominates the overall capacitance.

Grahame modified Stern's model by dividing the Helmholtz layer into the inner Helmholtz layer comprised of specifically adsorbed ions and solvent molecules and the outer Helmholtz layer comprised of solvated ions[1]. His contribution accounted for the discrete presence of the solvent within the double-layer for the first time, instead of viewing the solvent in a continuum sense.

1.1.2 Preliminary Studies to Incorporate Steric Constraints and Polarizability

So far, we focused on the electrical double layer theory for traditional dilute electrolytes. In this section, we discuss preliminary attempts to introduce finite size and ions/solvent polarizability effects into the double layer theory. The principles of EDL in concentrated electrolytes with finite ion size effects go back to studies by Bikerman[7], Dutta and Bagchi[8], Freise[9] and, Eigen and Wicke[10]. Particularly, Bikerman modified the Gouy-Chapman-Stern theory to account for finite ion size and polarizability of ions/solvent molecules. His work depicted that the potential drop in the EDL is not concentration dependent at high potentials. Eigen and Wicke modified Debye-Hückel theory to include volume corrections for ions and their hydration shells, as well as partial dissociation effects[10]. In the late 1990s, Borukhov et. al[11] and Iglic et. al[12] independently proposed EDL theories that incorporate steric effects into the Poisson-Boltzman approach of Gouy[4] and Chapman[5]. Antypov also investigated the effect of excluded-volume on the layering of ions as a function of distance from an interface, using a modified Poisson-Boltzmann approach[13]. These further improvements on the GCS model are significant as they set the stage for studies on finite size and polarizability effects on the EDL structure which become significant in concentrated ionic solutions.

1.1.3 Electrical Double Layer for Neat Room Temperature Ionic Liquids

Room temperature ionic liquids (RTILs) and their concentrated solutions offer distinct advantages over conventional dilute electrolytes in energy storage devices (e.g. electrochemical double-layer capacitors (EDLCs)), as their high electrochemical stability, charge density, low volatility and other tunable properties can lead to safer

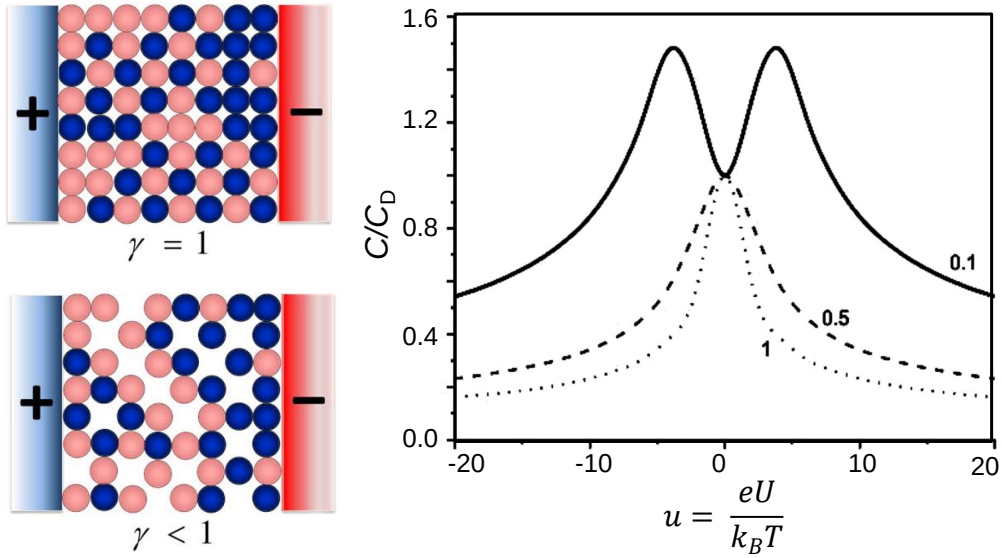

Figure 1.2: (left column) Cartoon showing an ionic liquid between two electrodes, representing the concept of the compacity parameter γ (red spheres standing for anions, blue spheres depict cations, and empty space in the lattice representing voids), (right column) Capacitance given by the mean-field theory, Equation 1.9, for indicated values of the compacity parameter, γ. The graph shows camel and bell shapes, for small and large values of γ, respectively[2].

devices with enhanced energy storage capability[14]. Nevertheless, their behavior at the EDL significantly deviates from these classical theories. In this section, we will provide a brief overview of the studies that describe charge and potential distribution in concentrated electrolytes near electrified surfaces.

RTILs exhibit potential-capacitance curves that significantly deviate from the Gouy-Chapman-like U-shaped profiles observed in dilute electrolytes. Two important phenomena, namely, *lattice saturation* (crowding) and *overscreening* lead to this deviation from U-shaped capacitance profiles. In particular, in RTILs, the volumetric constraints on the density of ions that accumulate in the double play a significant role in determining the potential decay as a function of distance from the electrode surface. This effect is called lattice saturation (crowding). Furthermore, overscreening of

the electrode charge at small electrode polarizations by the first later of ions near the surface leads to an oscillatory charge distribution that decays in the bulk electrolyte.

These concepts have been previously considered in molten salts[15, 16], but the first direct consideration of steric effects, and discussion on ion correlations in the context of RTILs was proposed in 2007 by Kornyshev as a mean field theory (MFT)[17]. This theory uses the principles of the lattice-gas model, in which N_+ cations and N_- anions are distributed over N lattice sites. The cation and anion concentrations ($c_+ = N_+/N$ and $c_- = N_-/N$) that is controlled by the electrostatic potential $\Phi(z)$ is read as

$$c_\pm = c_0 \frac{exp(\frac{\pm e\Phi}{k_B T})}{1 - \gamma + \gamma cosh(\frac{e\Phi}{k_B T})} \tag{1.5}$$

controlled by a single parameter γ given by the ratio of average ion concentration divided by the maximum possible ion concentration

$$\gamma = \frac{N_+ + N_-}{N} \tag{1.6}$$

The relationship between electrostatic potential and ion distribution is given by

$$\epsilon_* \frac{d^2\Phi}{dz^2} = 4\pi e[c_- - c_+] \tag{1.7}$$

combining these, the distribution of potential (Φ) as a function of distance from the electrode surface is obtained as

$$\frac{d^2\Phi}{dz^2} = \frac{8\Phi e c_0}{\epsilon_*} \frac{sinh(\frac{e\Phi}{k_B T})}{1 + 2\gamma sinh^2 \frac{e\Phi}{2k_B T}} \tag{1.8}$$

The resulting expression for capacitance is

$$C = C_D \, cosh(\frac{u}{2}) \frac{1}{1 + 2\gamma sinh^2(\frac{u}{2})} \sqrt{\frac{2\gamma sinh^2(\frac{u}{2})}{ln[1 + 2\gamma sinh^2(\frac{u}{2})]}} \tag{1.9}$$

where $C_D = \epsilon/(4\pi\lambda_D)$, $u = e^{\Phi}/k_BT$ and λ_D is given by Equation 1.3. The first two factors in Equation 1.9 are associated with the Gouy-Chapman capacitance, while the latter two factors take into account the lattice saturation and overscreening effects. The physical meaning of γ in neat RTILs is compacity[17], the ratio of the average number of ions in the bulk to the maximum number of ions in the double layer, and $1-\gamma$ is the fraction of void volume (Figure 1.2). When γ is small, voltage dependence of capacitance has U-shape, while with increasing γ it takes a double-hump shape, and eventually becomes bell-shaped (Figure 1.2).

This MFT theory concentrates on crowding effects and demonstrates the principal difference of the structure of electrical double layer in ionic liquids from those in dilute electrolytes. In the same paper where this theory is introduced[17], the necessity of incorporating short range Coulomb correlations, i.e. going beyond the mean-field approximation, is also pointed out.

Kornyshev's paradigm changing MFT was followed by two simulation-based studies that investigate the effect of Coulomb correlations (overscreening) in ionic liquids[18, 19, 20]. In particular, Federov and Kornyshev performed molecular dynamics simulations for a simplified system where they have confirmed the bell-shaped double layer capacitance versus potential curves predicted by the mean field theory[18, 19]. Their simulations depicted the remarkable overscreening effects due to ionic correlations in neat RTILs which results in oscillations of the electrostatic potential and surface charge density in the EDL. They also considered the effects of ion size asymmetry on the EDL in ionic liquids[20].

Later, Bazant et. al studied the structure of the electrical double layer using a Landau-Ginzburg-type continuum theory for neat RTILs[21, 22]. This model describes the interplay between overscreening and crowding effects and depicts that overscreening from short-range correlations is dominant at small voltages, while steric constraints of finite ion sizes prevail at large voltages.

1.1.4 Electrical Double Layer for Concentrated RTIL Solutions

The theories discussed so far pertain to neat RTILs. Although RTILs are regarded as the next-generation electrolytes for electrical double-layer capacitors (EDLCs), as their low volatility and wide electrochemical windows can lead to safer devices with greater energy density[23], their low conductivity limits the rate performance of EDLCs and yields devices with suboptimal power density[24].

To overcome this limitation, in top-performing EDLCs, the common practice is to add a polar organic solvent (e.g. acetonitrile) to a neat RTIL ($\approx$1 M), and improve the conductivity of the mixture while decreasing its viscosity[25, 26, 27]. Such RTIL/solvent mixtures are electrochemically stable up to 4 V and have also shown promise in devices operating at high temperatures[28, 29]. Additionally, RTILs offer processing advantages over traditional solid salt-based electrolytes, namely, they can be evaporatively consolidated with the active electrode material from a volatile phase (e.g., organic solvent) to form dense electrodes[25, 30]. Though improvements in rate performance have been achieved using these mixtures, the effect of diluting RTILs with organic solvents on the double layer capacitance of the electrode-electrolyte interface remains unclear[31, 32, 33, 34]. Understanding the effect of RTIL dilution with organic solvents on the double-layer capacitance is critical in the design of RTIL/solvent combinations that maximize capacitance and, correspondingly, improve the energy density of EDLCs. Also, this knowledge could be useful in understanding how impurities that are present in commercially available RTILs affect their capacitive properties. Chapter 2 of this dissertation addresses these questions to elucidate the mechanisms through which dilution of a concentrated ionic solution affects the double layer structure and its capacitive properties. We demonstrate that differential capacitance increases when a RTIL is diluted with an organic solvent in the concentrated regime, and provide a fundamental basis for these observations using simulations.

1.2 Protein Stability under Environmental Perturbations

Proteins fold into their compact, functional forms, and remain marginally stable under a narrow range of physiological conditions. This stability is determined by the interplay between many competing forces and can be perturbed by changes in the protein environment, such as temperature, pressure, and solvent properties[35, 36, 37, 38, 39, 40, 41]. Below we present a brief overview of molecular forces that affect protein stability. Next, we introduce the protein free energy landscape concept. These will provide the basis for Chapter 3 and Chapter 4 where we investigate the effect of environmental perturbations on protein stability.

1.2.1 Conformational Space of Proteins

The primary structure of a protein, that is the amino acid sequence, determines how a protein folds into its native fold[42, 43, 44]. Helices, beta sheets and beta turns constitute the *secondary structure*, and are formed mainly through hydrogen-bonding interactions. For a polypeptide to function, the secondary structure elements, loops and links of the protein usually fold into a *tertiary structure*. Association of the folded chains of polypeptides forms the *quaternary structure*. This native fold of the protein is not a static rigid structure, but it is an ensemble of conformations[42, 43, 44]. Secondary structure elements of the protein, as well as its tertiary structure, continually undergo small temperature-dependent fluctuations in the protein's conformational space. Even under physiological conditions, these fluctuations can sometimes be collective, resulting in the subunits of the protein to flip from one conformation to another. In particular, when the solvent environment deviates from physiological conditions and the protein is destabilized, these collective motions of the atoms become significant. Molecular dynamics studies can provide a detailed microscopic

description of these conformational fluctuations, both under thermodynamic equilibrium and as a response to enrionmental perturbations, through monitoring the protein as a function of order parameters that best represent the conformational space of the protein[45]. Figure 1.3 shows the conformational space, or free energy surface, of the miniprotein Trp-cage at two different temperatures under ambient pressure as a function of the following order parameters[45]: the root mean square deviation of the Cα atoms from the reference NMR structure[46] (Cα rmsd) and radius of gyration (R_g). The system samples two basins, one describing the folded state (small R_g and rmsd) and another corresponding to the unfolded state. In Chapter 3 and Chapter 4, we monitor the changes in the conformational space of proteins as a response to perturbations in solvent composition and in (T, P) phase space, respectively. We note that the order parameters used to construct these surfaces can be chosen in an ad-hoc manner, or they can be determined systematically (e.g. using dimensionality reduction methods[47, 48]).

1.2.2 Globular Proteins are Marginally Stable

Slight temperature, pressure or solvent composition changes in the protein environment can convert functional, folded proteins into denatured ones[49, 50, 40, 51]. For instance, the free energy surfaces of Trp-cage in Figure 1.3 depict that the unfolded state basin is not highly populated at low temperature but as the temperature increases above 315 K, it quickly dominates the weight of the distribution. The energy barrier this model protein needs to overcome to transition from the folded basin to unfolded basin is small (e.g., $\approx$2.5 kcal/mol at physiological conditions), the same order of magnitude as the energy contribution of a single hydrogen bond ($\approx$2-5 kcal/mol), indicating the marginal stability of the protein.

Two major contributors determine the free energy difference between the folded and unfolded states: *Enthalpy* and *Entropy*[42, 43, 52]. Enthalpy derives from the

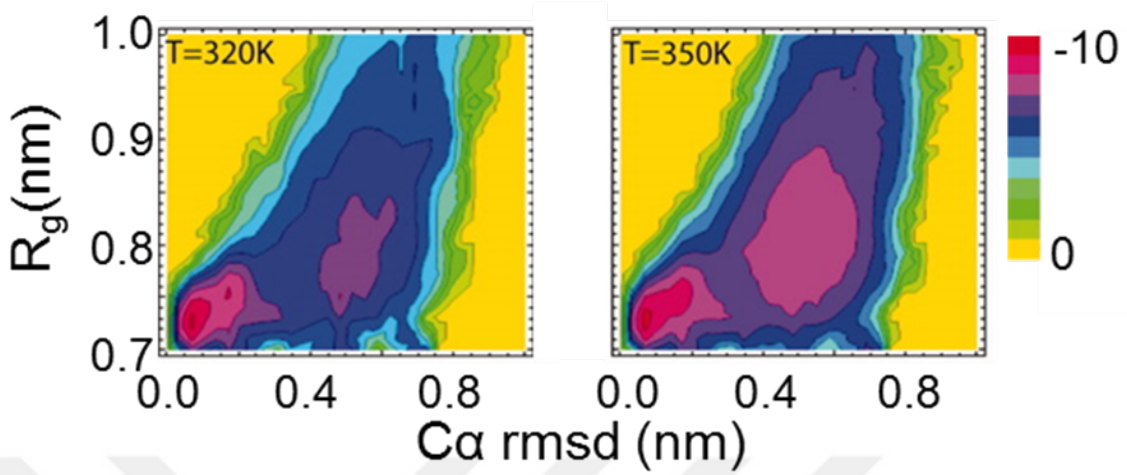

Figure 1.3: Free energy surface of Trp-cage as a function of the Cα rmsd and R_g at 320 K and 350 K. The surfaces show that the system occupies two main basins: one corresponding to the folded state (small Cα rmsd and compact states) and another to the unfolded state (large rmsd and less compact). The distribution of the states within a basin is due to thermal-fluctuations within the state. The legends use a logarithmic scale in units of RT. Figure adapted from Day et. al[45].

intramolecular and intermolecular energetic interactions, and the enthalpy difference between folded and unfolded states can reach several hundred kcal/mol[43]. In most cases the major contribution comes from noncovalent interactions. The covalent bonds within the protein stay the same in folded and unfolded states, with the exception of disulfide bonds. On the other hand, while noncovalent interactions are weaker than covalent bonds, since there are many of them in a protein, they sum up to a substantial energetic contribution in protein folding/unfolding events[43]. In particular, *electrostatic interactions* take place between positively and negatively charged regions. A particular type of electrostatic interaction is the salt bridge that forms between oppositely charged side chains when they are sufficiently close to each other. *Van der Waals interactions* are between temporary dipoles on non-bonded neighbors of the protein. *Hydrophobic side chains* are nonpolar and uncharged, thus they mainly engage in van der Waals interactions. In particular, the most polarizable groups induce the greatest van der Waals interactions (e.g. methyl and methylene groups of

hydrophobic side chains). The hydrophobic side chains tend to avoid contact with water by associating with each other, forming the basis for the *hydrophobic effect*[53] - a major driving force for the folding of globular proteins. The hydrophobic effect results in the burial of the hydrophobic residues in the core of the protein. *Hydrogen bonds* are formed between a hydrogen atom with significant partial positive charge due to being covalently bonded to a more electronegative atom (such as oxygen) and is attracted to an atom with a large negative partial charge. *Hydrophilic side-chains* are polar or charged, and can make hydrogen bonds. In the native fold of the protein, these interactions are maximized to produce a compact structure with a packed hydrophobic core, whereas they tend to be weakened in the more open and loosely packed denatured state.

Entropy derives from the second law of thermodynamics which states that the entropy of an isolated system never decreases, and systems spontaneously evolve towards maximum entropy. In physiological conditions, the native fold of a protein is highly ordered, whereas unfolded state tends to be disordered with the protein molecules taking many different conformations. Therefore, under physiological conditions, it is entropically favorable for the protein to be in a more disordered state. The energy difference between the folded and unfolded configurations due to entropy can also reach several hundred kcal/mol, but in the opposite direction to enthalpy difference. Thus, the total energy difference between the folded and unfolded states, which is called the *free energy difference*, results from the difference between the entropic and enthalpic contributions, and is much smaller than these individual contributions.

We can elucidate the molecular mechanisms that influence the free energy difference between the folded and unfolded states of a protein using molecular dynamics simulations. In particular, Chapter 3 and Chapter 4 of this dissertation investigate how pressure, temperature and solvent composition perturbations affect the interplay

between these mechanisms.

1.2.3 Protein Folding

Since Anfinsen and his colleagues, in 1973, postulated that a protein's primary structure and solution conditions dictate the unique three dimensional configuration that the protein spontaneously folds into[54], many models have been established to explain how a protein reaches this configuration.

The folded state of a protein has a free energy that is lower than other kinetically accessible conformational structures[55]. Thus, intuitively, one could imagine that protein molecules do a random search of all possible configurations until the lowest energy state is reached. Nevertheless, a simple calculation that Cyrus Levinthal made shows that this is impossible as folding by a random search of the conformational space would take an enormously long amount of time, yet, paradoxically, proteins fold in a time scale of seconds or less[56]. The earliest theories of protein folding (e.g. the framework model, the nucleation-condensation mechanism, the diffusion-collision mechanism, the hydrophobic collapse model) propose that proteins fold quickly because they follow predetermined pathways defined by discrete intermediates[50]. In particular, the diffusion-collision model proposes that small parts of the protein fold first, and then diffuse and collide to form larger parts[57, 58]. The nucleation-condensation theory postulates nucleation of transition state structures with some secondary structure form the native fold[59]. The hydrophobic collapse theory states that proteins may fold via the collapse of the hydrophobic core followed by the formation of secondary structure elements[60].

The more recent views of protein folding suggest that predefined pathways with discrete intermediates do not exist[50, 62, 63, 64]. In particular, the energy landscape theory states that folding follows a downhill path on the free energy landscape,

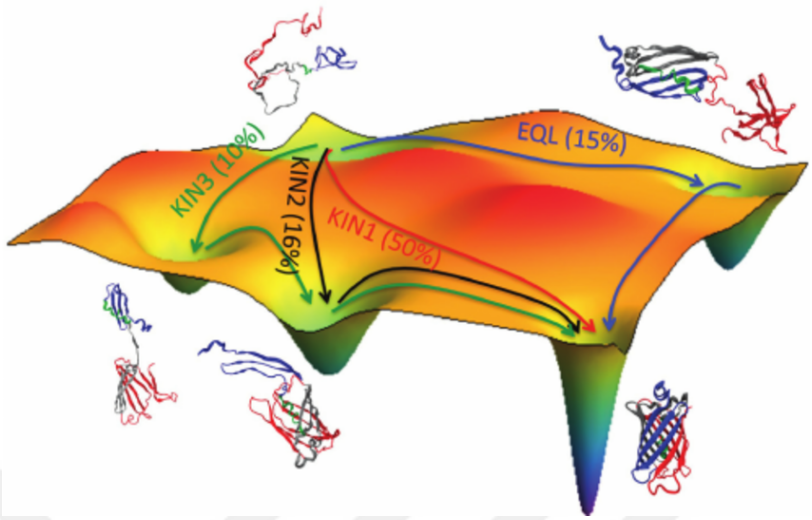

Figure 1.4: Example of a folding free energy landscape of the green fluorescent protein. During folding, the protein can be captured in many different topological traps, i.e. metastable states along its folding pathway. The different routes observed in folding simulations are indicated by arrows. Representative structures of the different metastable states are shown. The kinetic traps and metastable minima necessitate using advanced sampling techniques to efficiently sample the energy landscape. Figure is adapted from Bertz et. al[61].

through routes down a folding tunnel (Figure 1.4). This folding landscape has a rugged surface with 'traps', i.e. local minima in which the protein can transiently reside. Thus, there is no unique pathway but many folding routes that reach the native structure, and the folding process involves a stochastic search of the many conformations accessible to the protein[62].

Experimental and theoretical methods have been used to search for folding pathways. Some of these experimental techniques include optical spectroscopy methods[65], laser-induced temperature jump[66], laser photolysis, laser-initiated electron transfer[67], mutational methods to identify the residues that determine folding speed[68, 69], hydrogen exchange methods[70], extensive exploration of the free energy landscape of model proteins[71], and single molecule methods[72]. Nevertheless, it is often very difficult to examine the folding mechanisms experimentally since obtaining a molecular level understanding requires picosecond timescales at

atomistic resolution, and most experimental techniques are outside of this spatiotemporal resolution[73]. Consequently, atomistic computer simulations to study protein folding have been pursued to overcome these difficulties.

Atomistic classical MD simulations of proteins evolved from simulating very small proteins in vacuum to simulating large protein complexes in explicit solvents[74]. However, despite this success, there are still two major challenges associated with these simulations - the accuracy of force fields and computational cost. Although more remains to be done for force field development, force fields capable of folding proteins in good agreement with experiment already exist[74, 75, 76]. Exploring the free energy landscapes efficiently is still a major challenge in producing reliable simulations as computational limitations can lead to inadequate sampling of conformational states. However, advances in hardware, software, and sampling techniques provide solutions to the sampling challange. In particular, specialized hardware, efficient parallelization of MD codes, and development of advanced sampling methods such as replica exchange molecular dynamics, metadynamics and simulated annealing already have been contributing to this advancement[73]. In Chapter 3 and Chapter 4, we conduct extensive, highly parallelized fully-atomistic MD simulations combined with advanced sampling to investigate the mechanisms and thermodynamics of protein folding under environmental perturbations.

1.3 Liquid Water's Anomalies

Water is a tetrahedral liquid with a hydrogen bond structure that tend to form a three-dimensional, tetrahedral network in the liquid state [112]. Other examples of tetrahedral liquids include silicon, germanium, carbon, tin, silicon oxide and germanium oxide. These fluids are distinct from simple fluids in several ways. First, due to the tetrahedrally coordinated configurations, they generally have a lower density

than simple liquids with isotropic, close-packed molecules. Tetrahedral fluids also often exhibit several liquid-state anomalies including an increase in density on isobaric heating (negative thermal expansion coefficient (α)), and an increase in isothermal compressiblity (κ_T) and isobaric heat capacity (C_P) upon cooling. A schematic illustration of these response function profiles is given for the case of water in Figure 1.5.

One possible explanation for water's anomalous thermodynamics is the existence of a metastable first-order phase transition involving two distinct liquid phases that terminates at a liquid-liquid critical point (LLCP) in deeply supercooled water[77, 78]. According to the LLCP hypothesis, the thermodynamic response functions which can be represented as fluctuations in entropy and volume (Equations 1.10-12) diverge upon approaching the LLCP, as the entropy and volume fluctuations themselves also diverge at this location.

$$\alpha = \frac{1}{k_B T} \frac{\langle (S - \langle S \rangle)(V - \langle V \rangle) \rangle}{V} \tag{1.10}$$

$$\kappa_T = \frac{1}{k_B T} \frac{\langle (V - \langle V \rangle)^2 \rangle}{V} \tag{1.11}$$

$$C_P = \frac{1}{N k_B} \langle (S - \langle S \rangle)^2 \rangle \tag{1.12}$$

where $\langle\rangle$ denotes a statistical average, N is the number of molecules, and k_B is the Boltzmann's constant.

ThE LLCP hypothesis is consistent with the two-structure equation of state (TSEOS) concept that considers water as a mixture of two interconvertible states: a high-density, high-entropy state (structure A) and a low-density, low-entropy state (structure B)[80, 81, 82, 83]. In fact, a TSEOS has been developed and successfully used for the description of the thermodynamic anomalies in supercooled water[83, 84], as well as in different water models: mW[85], ST2[86], and TIP4P/2005[80]. In Chap-

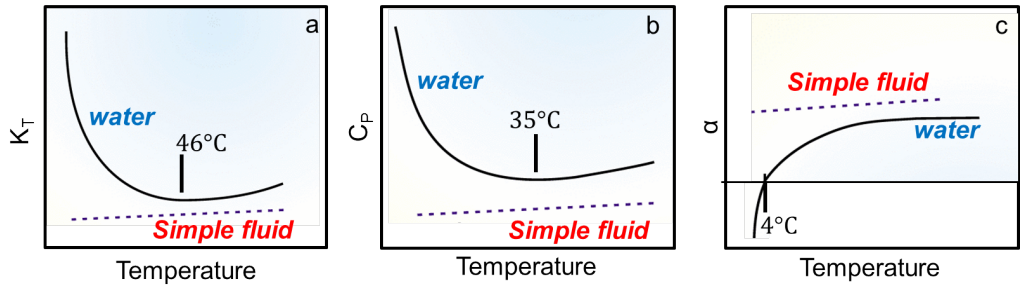

Figure 1.5: Schematic representation of waters anomalies at atmospheric pressure. (a) isothermal compressibility (κ_T) , (b) isobaric heat capacity (C_P) , and (c) thermal expansion coefficient (α). The behavior of water is indicated by the solid line; that of a typical liquid by the dashed lines. These three thermodynamic response functions are proportional to corresponding fluctuations in entropy or volume Adapted from Debenedetti et al.[79].

ter 5, we also use the TSEOS concept to study water's thermodynamic anomalies. The TSEOS exhibits a liquid-liquid phase transition (LLPT) when there is sufficient non-ideality in the mixing of these two alternative structures[83, 84, 86, 80].

In tetrahedral systems, regardless of the existence or non-existence of the LLPT (e.g., mW[87, 88, 89], mTIP4P[88], ST2[90], TIP4P/2005[91], TIP5P[92], silicon[93, 94, 95], silica[96, 97], germanium[98]), there is an underlying characteristic pattern of extrema lines for thermodynamic properties. The most well-known is the locus of density extrema, whose existence suggests a competition between low-density and high-density structures in the same liquid. For tetrahedral models with the LLPT, the location of the critical points and the thermodynamic property extrema are clearly system-dependent, but the various extrema loci exhibit many common features imposed by thermodynamics[88, 89, 99, 100, 101]. In particular, the loci of response function maxima merge asymptotically at the LLCP. The density shows maxima at positive pressures (temperature of maximum density, TMD). The TMD first shifts to higher temperatures as pressure is lowered, however, upon further decrease in pressure, it eventually retraces after reaching a maximum temperature ("nose") and terminates when it meets the locus of minimum densities (TmD). As required by

thermodynamic constraints for the case of a monotonically increasing liquid-vapor spinodal[100, 101], the locus of isothermal compressibility extrema intersects the TMD line's "nose". Also, the point at which the locus of density maxima joins the locus of density minima is a point along the locus of extrema of C_P, measured along isotherms[99, 100, 101]. Consequently, the question arises as to whether rescaling of the thermodynamic property extrema could provide a unified description of the patterns of property extrema loci for the tetrahedral systems that exhibit LLCP. To investigate this question, in Chapter 5, we analyze the patterns of extrema lines for three commonly used molecular water models (ST2, TIP4P/2005, and TIP5P), and a TSEOS fit for real water that exhibit a metastable liquid-liquid transition, and show that a corresponding-states-like rescaling of pressure and temperature results in a significant degree of universality in the pattern of extrema loci of the density, isothermal compressibility, and isobaric heat capacity.

Chapter 2

Concentration Fluctuations and Capacitive Response in Dense Ionic Solutions

This chapter is adapted from two papers published in The Journal of Physical Chemistry Letters (Betul Uralcan, Ilhan A. Aksay, Pablo G. Debenedetti, and David T. Limmer, J. Phys. Chem. Lett., ***7(13)****, 2333-2338, 2016 and David J. Bozym, Betul Uralcan, David T. Limmer, Michael A. Pope, Nicholas JSzamreta, Pablo G. Debenedetti, and Ilhan A Aksay, J. Phys. Chem. Lett.,* ***6(13)****, 2644-2648, 2015.*)

2.1 Introduction

Due to the increasing interest in ionic liquid based capacitors that provide high energy density devices [24, 102], ionic liquid-metal interfaces have become a recent focus of research [103, 104, 105, 106, 107, 2, 17, 108, 109]. Concentrated ionic solutions of RTIL/organic solvent mixtures are practically relevant as they have the potential to exhibit both high energy and high power densities [110]. Nevertheless, while the limiting behaviors of neat ionic liquids or their dilute solutions have been widely

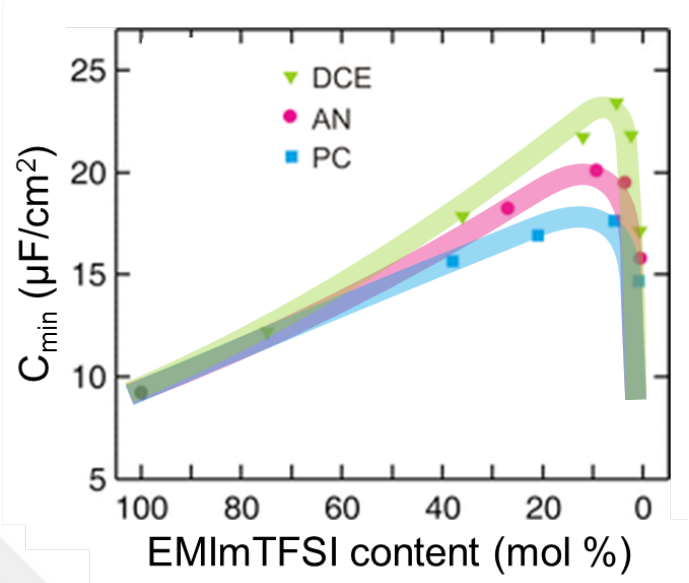

Figure 2.1: Differential capacitancepotential curves of the GCelectrolyte interface using neat [EMIM][TFSI] and [EMIM][TFSI] diluted with dichloro ethane (DCE), acetonitrile (ACN), and propylene carbonate (PC).

studied, relatively little is known about the properties of concentrated electrolytes at charged solid interfaces.

The findings of a few experimental[111, 112] and simulation[31, 32, 34] studies implied a possible capacitance enhancement with dilution in concentrated ionic solutions, but such an enhancement has not been unambiguously and systematically demonstrated. Furthermore, the existing EDL theories did not predict a capacitance enhancement with dilution. Consecutively, we have performed a rigorous analysis of the effect of RTIL dilution with organic solvents on the differential capacitance of a glassy carbon(GC)-electrolyte interface and have also provided a fundamental basis for the cause of this effect by using an Ising model[113].

In particular, we showed that the effect of solvent concentration on the differential capacitance of 1-Ethyl-3-methylimidazolium bis(trifluoromethylsulfonyl)imide ([EMIm$^+$][TFSI$^-$]) on glassy carbon electrodes that possess a large space charge capacitance[114] is significant, with the capacitance increasing with the addition of a

small amount of solvent (Figure 2.1)[113]. We measured the minimum differential capacitance (C_{min}) of the GC-electrolyte interface for mixtures of [EMIM][TFSI] diluted with acetonitrile (ACN), dichloro ethane (DCE), and propylene carbonate (PC) as a function of [EMIM][TFSI] content (Figure 2.1). C_{min} increased and reached a maximum at 5 and 10 mol% upon diluting the RTIL with all three solvents, demonstrating that the capacitance enhancement was not specific to a particular solvent.

While concentration effects in dilute solutions were well understood, i.e., the GCS theory predicts that capacitance increases proportionally to the square root of bulk ion concentration[4], a similar understanding for RTILs has been lacking in view of the experimental results presented above. To gain insight into the role of dilution on the capacitance in [EMIM][TFSI], we also simulated a coarse-grained model, defined by the Hamiltonian

$$H[s] = -J \sum_{\langle i,j \rangle} s_i s_j + \frac{q^2}{2} \sum_{i \neq j} s_i s_j v(r_{ij}) \tag{2.1}$$

where q is the charge density of a lattice site, J sets the strength of local repulsive interactions, s denotes the vector of Ising-like variables, $s_i = [0, \pm 1]$, $\langle i, j \rangle$ denotes a restriction over distinct nearest neighbor pairs, r_{ij} is the distance between sites i and j on a three-dimensional cubic lattice, and $v(r)$ is a Coulomb interaction evaluated on those lattice sites, which approaches $1/|\mathbf{r}|$ as $r \rightarrow \infty$. This so-called charge-frustrated Ising model[115] has been studied theoretically in the context of ionic liquids, reproducing interfacial experimentally observed phase diagrams, as well as molecular models[109]. In this model, solvent molecules are idealized as noninteracting cells, $s_i = 0$, with unit dielectric constant, and ions are constrained to a fixed density, ρ. Capacitance calculations for J = 1.5 and q = 2 are shown in Figure 2.2.

Consistent with experiment, for certain parameter regimes, we found a nonmonotonic dependence of the capacitance at zero charge, C, as a function of ion concen-

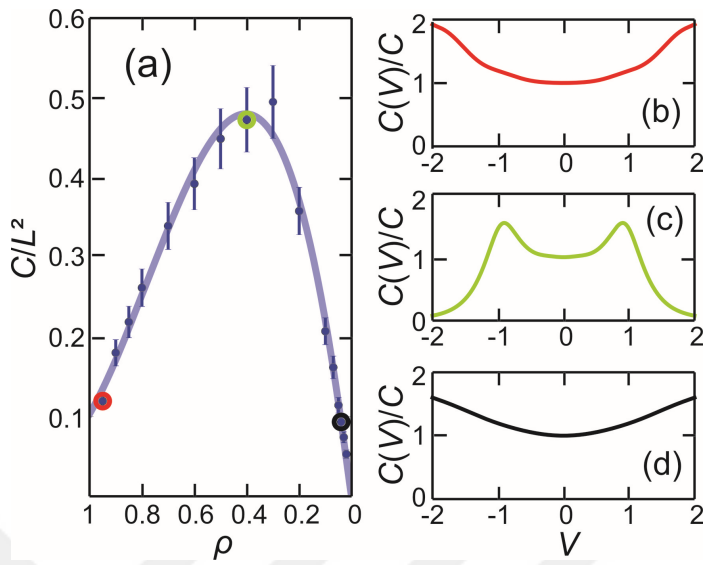

Figure 2.2: Capacitance as a function of ion concentration and potential for the charge-frustrated Ising model. (a) Capacitance as a function of ion concentration, for q = 2 and J = 1.5, normalized by the area of the electrode, L2. Error bars denote 1 standard deviation, and the line is a guide to the eye that asymptotes to $\sqrt{\rho}$ for small ρ. (bd) Capacitance curves for three concentrations, (b) $\rho = 0.95$, (c) 0.4, and (d) 0.05, as labeled by additional markers in panel a.

tration. While for low ion concentrations we recovered the square root dependence predicted by GCS theory, deviations from this scaling were found for ρ >0.1. Figure 2.2 shows that the capacitance as a function of applied voltage, $C(V)$, was consistent with the experimental measurements[113], with a curvature around V = 0 that increased with increasing ion concentration. For all ρ >0.1, we observed a double peak in the CV curves, as has been observed previously[2], with an increasing voltage range between the two peaks observed with increasing concentration.

Understanding the molecular mechanisms that lead to this nonmonotonic capacitance profile as a function of electrolyte composition requires molecular level models and is worth further exploration. Consecutively, to study the effects of solution composition on the electrochemical response of a double layer capacitor, we next use molecular dynamics simulations in a constant potential ensemble. Our molecular simulations also show that capacitance first increases with ion concentration follow-

ing its expected ideal solution behavior but decreases upon approaching a pure ionic liquid in agreement with our experimental and lattice-model results. The nonmonotonic behavior of the capacitance as a function of ion concentration results from the competition between the independent motion of solvated ions in the dilute regime and solvation fluctuations in the concentrated regime. Mirroring the capacitance, we find that the characteristic decay length of charge density correlations away from the electrode is also nonmonotonic. The correlation length first decreases with ion concentration as a result of better electrostatic screening but increases with ion concentration as a result of enhanced steric interactions. When charge fluctuations induced by correlated ionsolvent fluctuations are large relative to those induced by the pure ionic liquid, such capacitive behavior is expected to be generic.

2.2 Results and Discussions

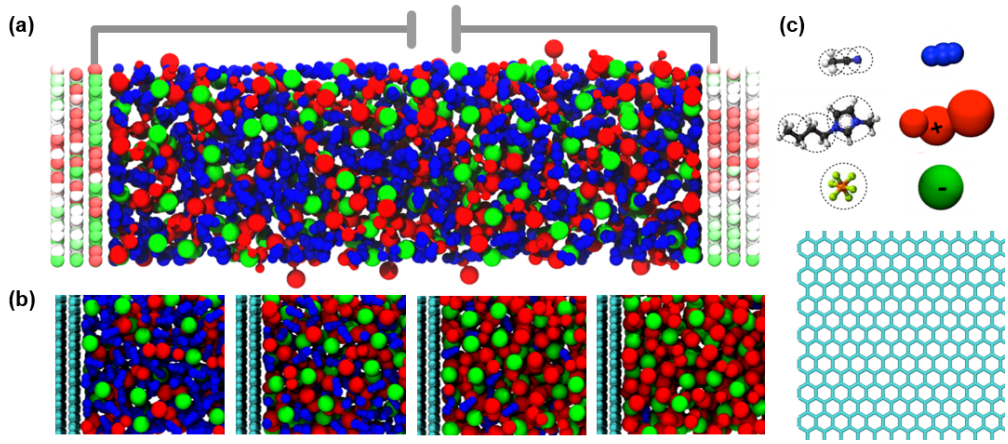

Figure 2.3: Simulated capacitor. (a) Each capacitor consists of an electrolyte between two electrodes maintained at constant potential difference. The color code on the electrode atoms indicates the instantaneous charge on each carbon atom. (b) Close-ups of the graphene/electrolyte interface for $\rho = 0.12$, 0.31, 0.68, and 0.89 electrolyte systems are shown. (c) Illustration of the coarse-grained models used in the simulations for ACN (blue), [BMIM] (red), and [PF6] (green). The electrode is composed of three layers of carbon atoms with its basal plane exposed.

Using MD simulations in the constant potential ensemble, we can investigate the relationship between the molecular structure of the electrolyte and the thermal electrode charge fluctuations. This approach offers a physically transparent way to decompose the effects of microscopic correlations on electrochemical response[116]. The subtle effects resulting from the interplay between these solvent-solvent, ion-ion and solvent-ion correlations are not easily understood from continuum treatments. The specific system considered here utilizes coarse-grained molecular models with non-specific surface-fluid interactions and is aimed at capturing the behavior of a typical low molecular weight ionic liquid-solvent mixture in contact with idealized electrodes. Specifically, we employ molecular simulation models of butlymethylimidazolium hexafluorophosphate ([BMIM][PF6]) [117] - acetonitrile (ACN) [118] mixtures bounded by electrodes modelled as three parallel ideal conductor honeycomb lattices of carbon atoms on both sides [119] as depicted in Figure 2.3(a). Despite its relative simplicity, this model has been shown to yield good agreement between simulation and experiment for a variety of bulk and interfacial properties [108, 120, 121, 122]. Figure 2.3(b) shows characteristic snapshots of the electrode-electrolyte interface for different ion-solvent compositions. Details on the molecular models are given in Appendix 2.A.

The algorithm we use to maintain a constant potential across the capacitor follows from Reed et al. [123] based on the work of Siepmann and Sprik [124]. During the simulation, the charge on each electrode atom fluctuates in response to the thermal motion of the electrolyte with fixed potential difference $\Delta\Psi$, temperature T and system volume V. The number of electrolyte molecules $N = N_{\mathrm{i}} + N_{\mathrm{s}}$, where N_{i} is the number of ions and N_{s} is the number of solvent molecules, is also kept fixed during the simulation. The electrode charges are determined at each time step by minimizing the potential energy subject to a constraint of constant voltage, which can be solved efficiently by matrix inversion[125]. Within this ensemble, the differential capacitance, $C(\Delta\Psi)$, is calculated from the variance of electrode charge fluctuations

using the fluctuation-dissipation theorem [126, 127],

$$C(\Delta\Psi) = \frac{\partial Q}{\partial \Delta\Psi} = \beta\langle \delta Q^2 \rangle \,, \tag{2.2}$$

where Q is the total charge of one electrode, $\beta = 1/k_{\mathrm{B}}T$, with k_{B} Boltzmann's constant, $\langle \ldots \rangle$ indicates the ensemble average with constant N, $\Delta\Psi$ and $T = 400$ K, and $\delta Q = Q - \langle Q \rangle$.

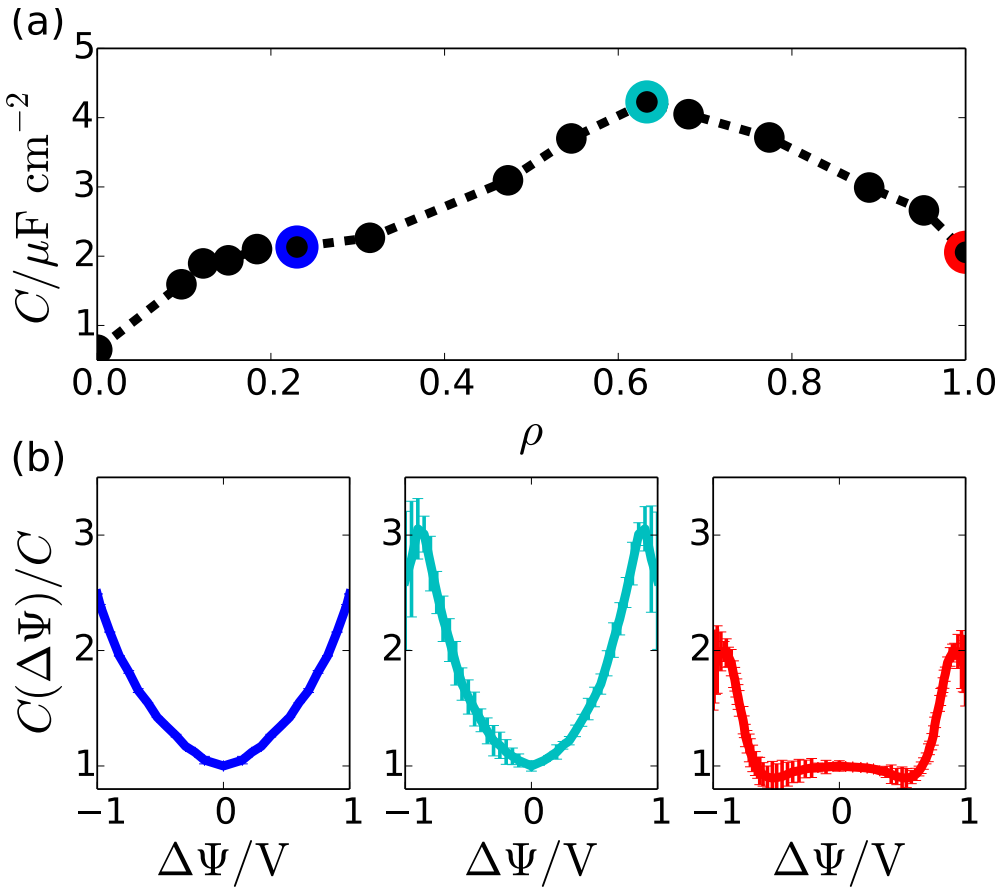

Figure 2.4: Capacitance as a function of ion fraction and potential. (a) Capacitance at zero applied potential as a function of ion concentration, normalized by the area of the electrode. The line is a guide to the eye. Error estimates are smaller than the circle size. (b) Capacitance as a function of applied potential for three ionic liquid mole fractions, 0.23, 0.63, and 1 (left to right).

Figure 2.4(a) shows C, the capacitance at zero applied potential, as a function of ion fraction $\rho = N_{\mathrm{i}}/N$. While C increases with increasing ion concentration near $\rho = 0$, in the concentrated regime it decreases with ion concentration and exhibits a peak near $\rho = 0.63$. The increase in capacitance with increasing ion concentration in the dilute regime is expected from Gouy-Chapman-Stern theory, where near the potential of zero charge, the capacitance is proportional to the square root of ion concentration[128]. The peak in capacitance is consistent with experimental results of a different ionic liquid in contact with a molecularly rough electrode[113], suggesting an origin for this behavior within the electrolyte.

Figure 2.4(b) shows the capacitance as a function of potential calculated using histogram reweighting techniques[116]. Details on the methods are in the Appendix 2.A. Capacitance profiles as a function of electrode potential for the three systems in Fig. Figure 2.4(b) exhibit a broadening near the potential of zero charge with increasing concentration, consistent with experiment[113]. The nonmonotonic concentration dependence of capacitance at $\Delta\Psi = 0$ V is observed throughout the 2 V potential window. For pure ionic liquids, previous studies foreshadowed an unbounded capacitance at $\Delta\Psi = \pm 0.9$ V due to a surface phase transition[108]. In that regime, finite size effects not studied here are likely important. The capacitance calculated from electrode charge fluctuations should be symmetric around $\Delta\Psi = 0$ V, and any deviation is due to statistical uncertainty.

The capacitance-voltage relationship of pure [BMIM][PF6] features symmetric double-peaks [2]. When the ionic solution is diluted to $\rho = 0.63$, the peaks are retained and curvature around $\Delta\Psi = 0$ V also increases. The peaks at moderate to high voltages result from the small bias to expel counterions and solvent from the interface[21, 2, 17] with increasing potential difference. At larger potentials when the ionic adlayer condenses, charge fluctuations are sterically suppressed and capacitance decreases[21, 2, 17]. As ρ is decreased further, the curve becomes U-shaped. This U-

shape at low ion concentrations results from charge fluctuations that are proportional to the number of ions near the interface, whose number can grow by expelling solvent molecules away from the electrode without the steric constraints that occur at high concentrations[21, 2, 17]. Hereafter, we focus on electronic and structural properties at $\Delta\Psi = 0$ V.

The concentration dependence of the capacitance can be understood by decomposing the charge fluctuations into different components,

$$\langle(\delta Q)^2\rangle = \langle(\delta Q_{\mathrm{s}}^2)\rangle + \langle(\delta Q_{\mathrm{i}})^2\rangle + 2\langle\delta Q_{\mathrm{s}}\delta Q_{\mathrm{i}}\rangle\,, \tag{2.3}$$

where $\langle(\delta Q_{\mathrm{s}})^2\rangle$ and $\langle(\delta Q_{\mathrm{i}})^2\rangle$ are due the the solvent and ions respectively, and $\langle\delta Q_{\mathrm{s}}\delta Q_{\mathrm{i}}\rangle$ are fluctuations induced by ion-solvent correlations. This decomposition is possible for a conductor where the electrode charges are linear functions of the partial charges of the electrolyte[116]. Microscopically, they can be explicitly computed using the Stillinger-Lovett sum rules for the charge-charge structure factor[129]. Simulations of a pure ACN-electrode system gives $\beta\langle(\delta Q)^2\rangle = \beta\langle(\delta Q_{\mathrm{s}})^2\rangle = 0.65 \pm 0.06$ μF/cm^2, which is significantly smaller than that of the ionic solutions. Therefore, $\langle(\delta Q_{\mathrm{s}})^2\rangle$ are expected to be negligible over the entire concentration regime, consistent with the expectation that since solvent molecules do not carry a net charge they cannot efficiently polarize the electrode surface.

The second term in Equation 2.3, $\langle(\delta Q_{\mathrm{i}})^2$, is expected to govern the behavior of electrode charge fluctuations both in the dilute ion regime and as $\rho \to 1$. For an ideal solution, the differential capacitance can only increase with an increase in the fraction of independent ions, a number set by the screening length. Deviations from this monotonic increase are expected in the limit of a pure ionic solution, as ions cease behaving ideally. However as Figure 2.4(a) shows, rather than a plateau in the capacitance as $\rho \to 1$, there is a maximum at intermediate concentrations. This

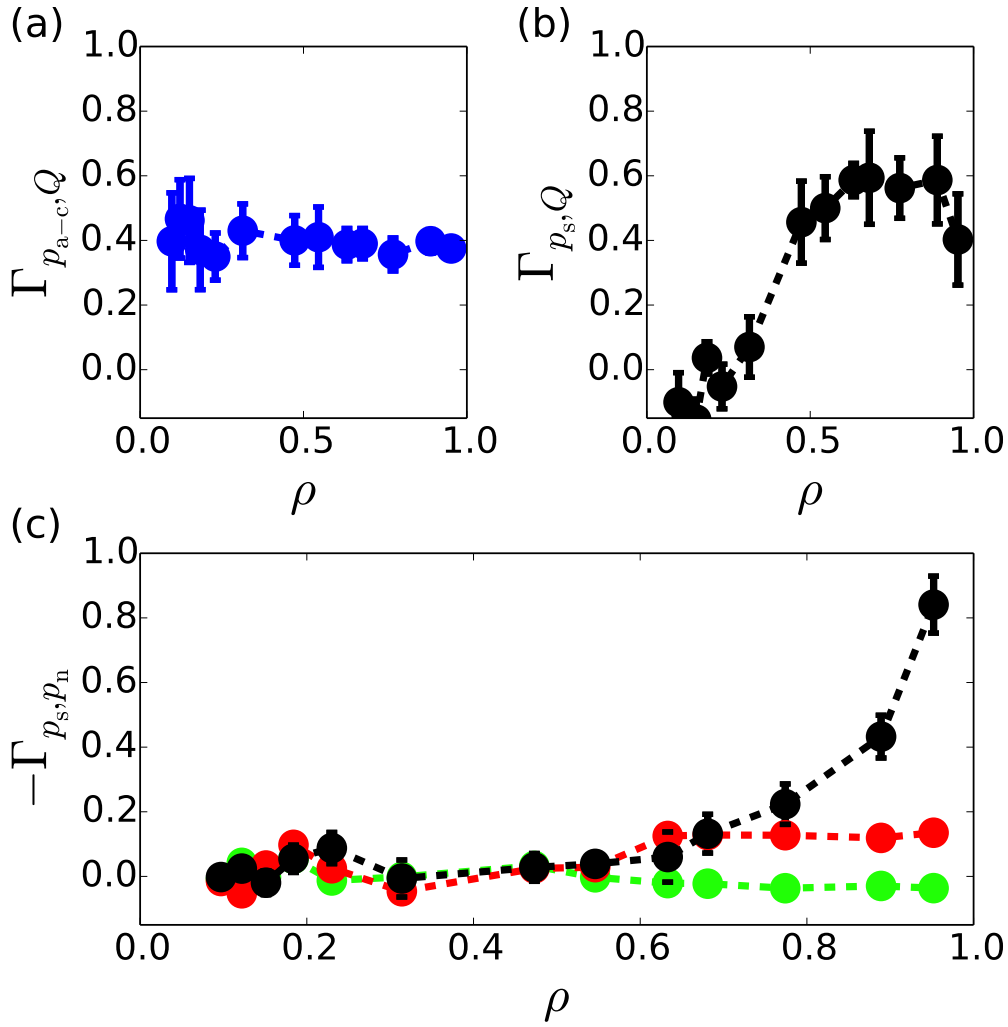

Figure 2.5: Composition dependence of electrolyte-electrode charge correlations at $\Delta\Psi = 0$ V. Normalized static cross-correlation coefficients between (a) electrode charge fluctuations and ion polarization; (b) electrode charge fluctuations and interfacial solvent concentration weighted by its displacement from the electrode; (c) interfacial solvent concentration weighted by its displacement from the electrode and ion polarization p_{a-c} (black), cation p_c (red) or anion p_a (green) concentration, weighted by its displacement from the electrode at the interface. The lines are guides to the eye. Error bars represent one standard deviation and are smaller than the markers when not shown.

suggests that the third term, $\langle \delta Q_{\mathrm{s}} \delta Q_{\mathrm{i}} \rangle$, plays a significant role in determining the magnitude of charge fluctuations. In fact, as discussed below, for concentrated electrolytes the motion of solvent molecules is highly correlated with the charge density fluctuations near the electrode interface, due to the incompressibility of the solution. These ion-solvent correlations enhance the electrode charge fluctuations by affecting the magnitude of the induced image charge on the electrodes.

In particular, Figure 2.5(a) illustrates the concentration dependence of the cross correlation coefficient between electrode charge fluctuations and ion polarization,

$$\Gamma_{p_x,Q} = \frac{\langle \delta p_x \delta Q \rangle}{\sqrt{\langle (\delta p_x)^2 \rangle \langle (\delta Q)^2 \rangle}}\,, \tag{2.4}$$

where $p_x = \{p_{\mathrm{a-c}}, p_{\mathrm{s}}\}$, and $p_{\mathrm{a-c}}$ is the charge polarization near the electrode and p_{s} is the interfacial solvent concentration, weighted by its displacement from the electrode. The interfacial polarization is computed by summing over the N_{i} ions with instantaneous displacement from the electrode less than $z_{\mathrm{c}} = 0.9$ nm, as

$$p_{\mathrm{a-c}} = \frac{1}{v} \sum_{i=1}^{N_{\mathrm{i}}} \hat{z}_i q_i \Theta(z_{\mathrm{c}} - \hat{z}_i)\,, \tag{2.5}$$

and similarly,

$$p_{\mathrm{s}} = \frac{1}{v} \sum_{i=1}^{N_{\mathrm{s}}} \hat{z}_i \Theta(z_{\mathrm{c}} - \hat{z}_i)\,, \tag{2.6}$$

where q_i is the charge of ion i, $\Theta[x]$ is the Heaviside step function, $\hat{z}_i$ is the instantaneous displacement of the ion from the electrode and v is the volume of the $L \times L \times z_{\mathrm{c}}$ slab. The thickness z_{c} is chosen to accommodate the first two solvation layers near the electrode and the results are qualitatively insensitive to its precise value. The constant profile in Figure 2.5(a) reveals that ion polarization at the interface has a similar effect on electrode polarization regardless of the electrolyte composition. Correlations between interfacial solvent displacement and electrode charge become more

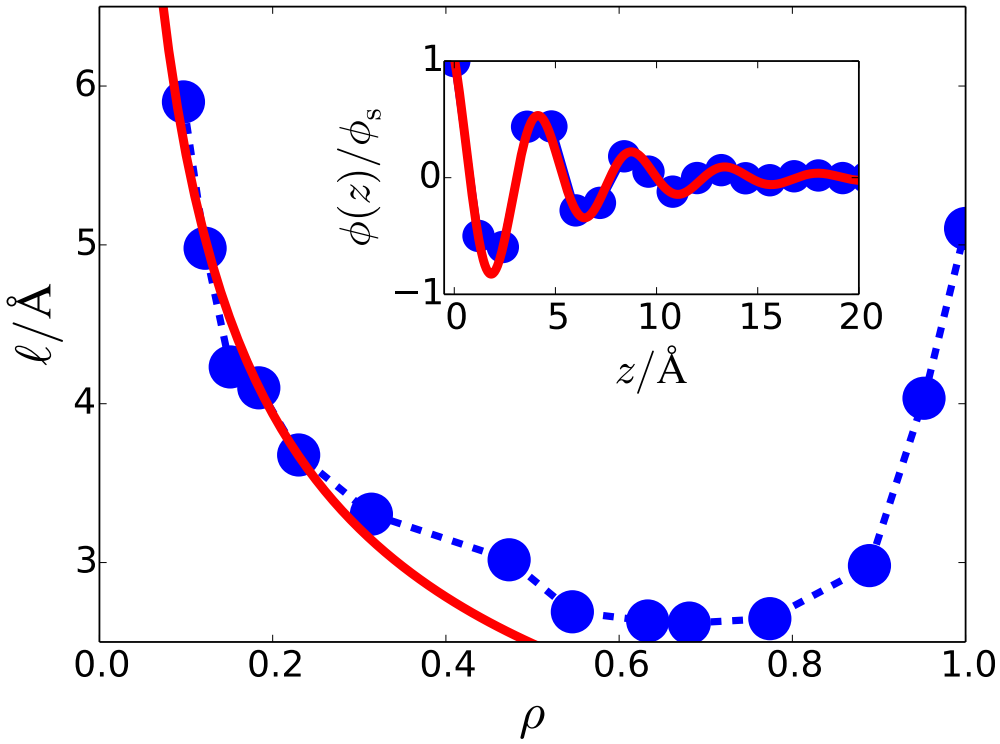

Figure 2.6: Charge density correlation length as a function of ion concentration. See Equation 2.8 for definition. The solid line is a fit to $\ell \propto 1/\sqrt{\rho}$, as predicted from Gouy-Chapman theory. The dashed line is a guide to the eye. Coarse-grained charge density as a function of distance from the electrode surface is given in the inset. The solid line is a fit to Equation 2.8.

pronounced with increasing ion concentration. This is indicated in Figure 2.5(b) by the cross correlation coefficient between Q and p_s.

Since solvent fluctuations themselves cannot significantly polarize the electrode, increasing $\Gamma_{p_s,Q}$ with concentration implies that solvent motion is correlated with ion polarization that in turn gives rise to the increase in Figure 2.5(b). In fact, Figure 2.5(c) shows solvent fluctuations correlated with cation and anion center of mass and ion polarization fluctuations,

$$\Gamma_{p_s,p_n} = \frac{\langle \delta p_s \delta p_n \rangle}{\sqrt{\langle (\delta p_s)^2 \rangle \langle (\delta p_n)^2 \rangle}} \tag{2.7}$$

where $p_{\mathrm{n}} = \{p_{\mathrm{a}}, p_{\mathrm{c}}, p_{\mathrm{a-c}}\}$ and p_{a} (p_{c}) is the interfacial anion (cation) concentration, weighted by its displacement from the electrode, and calculated analogously to p_{s}. While cation-solvent and anion-solvent correlations do not exhibit strong compositional dependence, solvent-polarization correlations are enhanced with increasing ion concentration. The negative value of this covariance arises molecularly from swapping motions that simultaneously moves the center of mass of the solvent molecules away from the electrode while polarizing the electrode by increasing the charge separation in the direction of the electrode.

The source of these increasing ion-solvent correlations can be understood as arising from the solvent's ability to facilitate fluctuations in an otherwise dense, incompressible and strongly associated fluid. Namely, for an ion pair to be separated and polarize the electrode, a fluctuation in the surrounding solvent must occur to stabilize that polarization. The increase in magnitude of this correlation with ion concentration, results from the increasing steric constraints of the ions. This picture is consistent with the results from lattice model calculations[113], where the capacitance maximum can be recovered by treating the solvent molecule as a defect that enables ionic reorganization, but does not directly contribute to the charge fluctuations.

In order to provide a structural interpretation of the composition dependence of the correlations described above, we construct a coarse-grained charge density distribution away from the electrode. Specifically, we take the out-of-plane charge density distribution computed from the simulations and average over 1 Å bins, so as to integrate out small length scale features associated with the internal structure of the ions. A representative coarse-grained profile is plotted in the inset of Figure 2.6. For all concentrations studied, the coarse-grained charge density can be fit with a damped harmonic function with decay constant ℓ and periodicity q_{s},

$$\phi(z) = \phi_{\mathrm{s}} e^{-z/\ell} \cos(2\pi z/q_{\mathrm{s}} + \theta) \tag{2.8}$$

where z is distance from the first maximum of $\phi(z)$, ϕ_s is the magnitude of that first maximum and θ is an angular offset. This functional form has been derived theoretically for pure ionic liquids [109] and is routinely used in experimental studies to fit the charge density profile of dense electrolytes[103]. The periodicity of charge oscillations, q_s originates from the interplay of excluded volume of the ions and screening[109] and we find that it can be fixed to 4.2 Å, or a little smaller than the average size of the ions, for all concentrations. This indicates that ions can maintain their preferred distance from each other regardless of electrolyte composition.

The decay length, ℓ, reflects the scale of ionic correlations away from the electrode surface. As shown in Figure 2.6, in the dilute regime $1/\ell$ scales as the square root of ion concentration, qualitatively in agreement with Debye-Hückel theory, though quantitatively inconsistent with the known dielectric constant for this solvent model [118]. In the pure ionic liquid, ℓ is determined by steric interactions [109] and thus, its decrease with decreasing ion concentration signifies a solvent mediated reduction in packing constraints. This behavior is consistent with an $\ell \propto \sqrt{1-\rho}$ dependence extracted from lattice model calculations[113] where the capacitance enhancement in the concentrated regime is facilitated by the solvent's ability to enable ionic reorganization in an otherwise incompressible fluid. This reduction in charge density oscillations with solvent has been noted in previous simulations of different solutions [34]. The steeper charge density decay as a function of distance from the electrode surface with the dilution of the ionic solution in the concentrated regime is analogous to that found in experiment [103]. Both ℓ and q_s obtained from the interfacial profiles show similar trends with the correlation length and periodicity extracted from bulk radial charge density distributions as given in Appendix 2.A, consistent with the expectation that the electrode interacts with the solutions weakly.

The maximum charge density near the electrode, ϕ_s, is determined by the relative surface propensities of cations, anions and solvent and depends intimately on the

details of the intermolecular interactions [130, 131, 132, 133]. To quantify this, the inset of Figure 2.7 depicts the free energy difference, $\Delta F(z)$, for moving an ion from the bulk to a distance z from the electrode, computed from

$$\beta \Delta F(z) = -\ln\left[\rho(z)/\rho_{\mathrm{b}}\right] \tag{2.9}$$

where $\rho(z)$ is the local ion density and ρ_{b} is the bulk ion density. Figure 2.7 shows the depths of the first minimum, ΔF^{w}, for both cation and anion, which is indicative of the strength of selective ion adsorption at the interface.

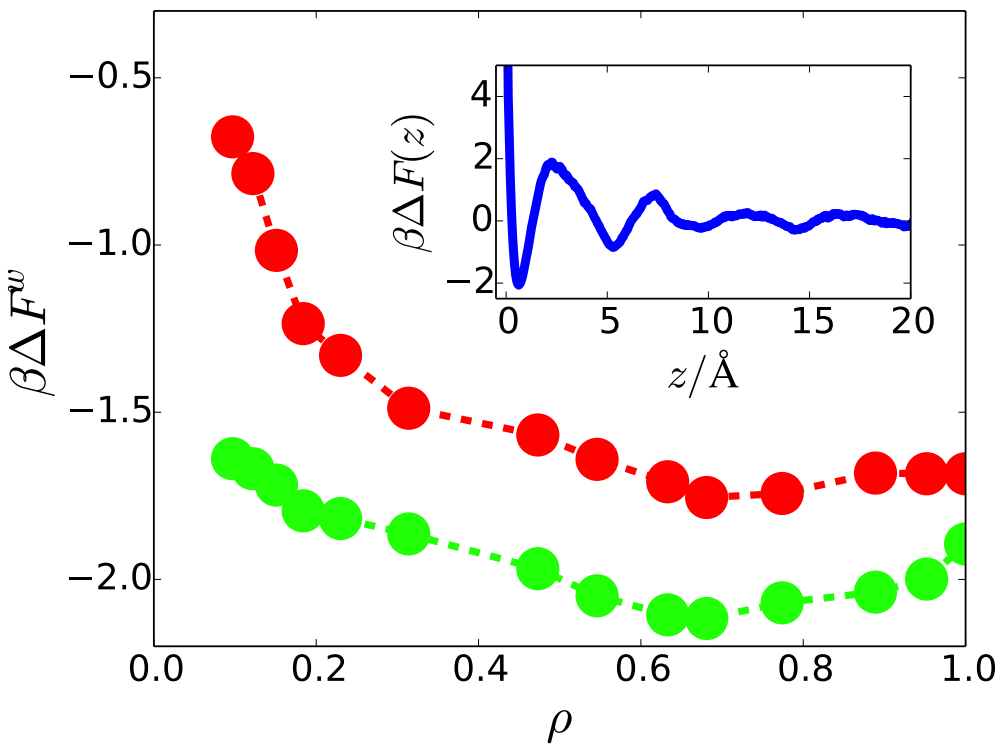

Figure 2.7: Ion surface adsorption free energies at $\Delta\Psi = 0$ V. The adsorption free energy obtained for the cation (red), and anion (green), as a function of composition. Error estimates are smaller than the circle size. The lines are guides to the eye. The inset shows the free energy profile for moving an anion at $\rho = 0.09$ as a function of distance from the electrode surface.

Adsorption of both cations and anions depends strongly on the bulk electrolyte concentration. In the dilute regime, the affinity of both ion types for the interface increases with ion fraction. The effect is larger for the cation, consistent with previous work suggesting that it is weakly solvated [34]. In the concentrated regime, the adsorption affinities of both ions do not change appreciably, though the anion is slightly depleted from the interface in the pure ionic liquid. These observations mirror those derived from the charge density distribution. In the dilute regime, changing ion concentration changes the average density of ions near the interface, which acts to increase fluctuations proportionally. In the concentrated regime, average densities are not strongly affected by solvent concentration, but fluctuations around the mean are influenced. In the charge density, this is manifested in the extent of charge density layering, while here it is manifested in the changing barrier height to move between layers. These observations are in accord with the results of Feng et al.[134] where the introduction of a small amount of water into an ionic liquid system was found to have very little impact on ion adsorption affinities but leads to an increase in the capacitance at 2V. The authors show that the capacitance enhancement is associated with the larger potential drop at the electrical double layer in the absence of water molecules, which disrupts the ion ordering at the interface, and stems mainly from energetic effects. Our studies in progress reveal that in the acetonitrile-ionic liquid system entropic effects also play an important role due to the fact that the solvent molecules are comparable in size to the ions.

2.3 Conclusions

Recent experimental observations have shown that the differential capacitance of a room temperature ionic liquid based electrical double layer capacitor can change markedly with solvent concentration [113, 111, 112]. Using molecular dynamics (MD)

simulations we show that the concentration dependence of the capacitance results from the interplay between two different limiting behaviors. In the dilute ion concentration regime, charge fluctuations are simply proportional to the number of ions near the electrode, because their mean distances are larger than the electrostatic screening length and so those fluctuations are uncorrelated [2]. In the pure ionic liquid, ions are densely packed and charge fluctuations are determined by steric constraints and interionic Coulomb correlations [17, 20, 18, 19, 21, 22, 135]. The addition of a small amount of solvent mediates these constraints, increasing the magnitude of charge fluctuations. At a specific concentration these effects are balanced, leading to an intermediate concentration where the capacitance is maximized. The analysis presented here offers a general way to understand the molecular contributions to the electrochemical response of complex electrolyte solutions, opening new directions for the optimization and rational design of energy storage devices.

2.A Appendix

2.A.1 Simulation Details

In this system, electrolyte species are represented by coarse-grained models where the interactions beyond chemically bonded atoms are represented by Lennard-Jones and Coulombic forces. The force field for [BMIM][PF6] is developed by Roy and Maroncelli[117] while the model for ACN is taken from Edwards et al.[118]. ACN and [BMIM] are represented by three site molecules and [PF6] is treated as a sphere. The electrodes are modeled as three layers of fixed pristine metallic graphene sheets subject to two-dimensional periodic boundary conditions[119]. The distance between carbon atoms within each layer is 1.43 Å, and the distance between layers is 3.38 Å. The parameters are summarized in Table 2.1. We study fourteen systems, containing

ρ = 0.09, 0.12, 0.15, 0.18, 0.23, 0.32, 0.47, 0.54, 0.63, 0.68, 0.77, 0.89, 0.95 and 1 molar fraction of [BMIM][PF6].

The molecular dynamics simulations were conducted in the NVT ensemble using a time step of 1.5 fs and a langevin thermostat with a time constant of 6-9 ps. Average pressure for all systems is maintained at 10 atm. For each simulation at 0 V, 2-7 ns equilibration at T = 400 K is followed by a 20-80 ns production run from which configurations are sampled every 0.15 ps.

Table 2.1: Force-field parameters for the molecules of the electrolyte and electrode[117, 118, 119]. A is [PF6], while C1, C2 and C3 are the three sites of the [BMIM] cation. Me is the methyl group, and CA and N are the other two sites of acetonitrile. CE is the carbon atoms of the electrode. Crossed parameters are calculated by Lorentz-Berthelot mixing rules.

	A	**C1**	**C2**	**C3**	**Me**	**CA**	**N**	**CE**
σ (Å)	5.06	4.38	3.41	5.04	3.60	3.40	3.30	3.37
ϵ (kJ/mol)	4.71	2.56	0.36	1.83	1.59	0.42	0.42	0.23
q(e)	-0.78	0.4374	0.1578	0.1848	0.269	0.129	-0.398	
M(g/mol)	144.96	67.07	15.04	57.12	15.04	12.01	14.01	
x(Å)	0	0	0	0	0	0	0	
y(Å)	0	-0.527	1.641	0.187	0	0	0	
z(Å)	0	1.365	2.987	-2.389	0	1.46	2.63	

2.A.2 Capacitance as a Continuous Function of Electrode Potential

In order to determine the evolution of capacitance with applied voltage, we perform additional simulations at seven electrode potentials $(0.15, 0.30, 0.45, 0.60, 0.75, 0.90$ and 1.0 V). We estimate the probability distribution of the total electrode charge at any potential by combining the data from the simulations performed at various potential differences using the weighted histogram analysis method with the expression

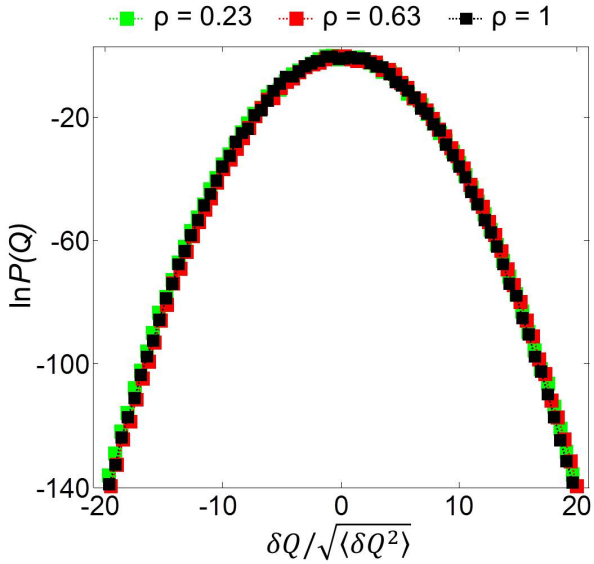

Figure 2.A.1: Probability distribution of the total charge Q on the electrodes at $\Delta\Psi = 0$ V for $\rho = 0.23$, 0.63 and 1.

$$-\ln P(Q|0) = -\ln P(Q|\Delta\Psi) + \beta Q \Delta\Psi + \beta \Delta F \tag{2.10}$$

where $\Delta F = F(\Delta\Psi) - F(0)$[116].

The probability distribution of the total charge Q on the electrodes at $\Delta\Psi = 0$ V is reported in Figure 2.A.1 as a function of $\delta Q/\sqrt{\langle(\delta Q)^2\rangle}$. In this way, each simulation under an applied potential provides an estimate of the charge distribution at any other potential. Capacitance is then calculated by computing the variance of electrode charge fluctuations from the probability distribution data.

2.A.3 Bulk Charge Density

Radial charge density distributions for bulk electrolyte is computed and fit with a damped harmonic function as in Equation 2.8. The decay constants ℓ obtained from the bulk charge density profiles are given in Appendix 2.A. The periodicity of oscillations, q_s, is 5.51 Å. The similar trends obtained from bulk and out-of-plane charge

density distributions is consistent with the expectation the electrode interacts with the solutions weakly.

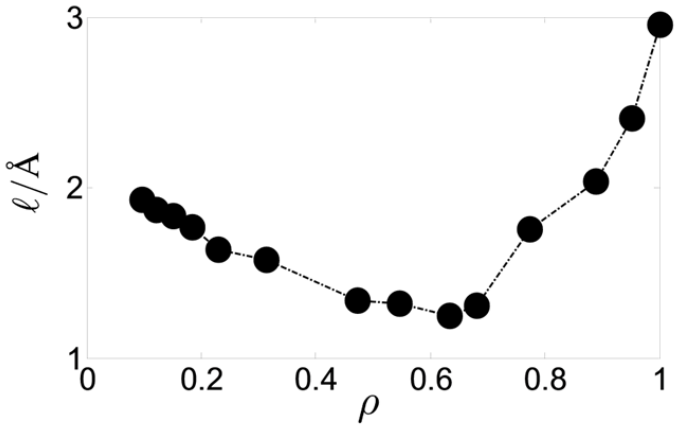

Figure 2.A.2: Charge density correlation length obtained from bulk charge density distribution as a function of ion concentration. See Equation 2.8 for the definition of correlation length. The black line is a guide to the eye.

Chapter 3

A Computational Study of the Ionic Liquid-Induced Destabilization of the Miniprotein Trp-Cage

This chapter is adapted from our work published in The Journal of Physical Chemistry B (Betul Uralcan, Sang Beom Kim, Chester E. Markwalter, Robert K.Prudhomme, and Pablo G. Debenedetti, J. Phys. Chem. B, ***122(21)****, 5707-5715, 2018). Betul Uralcan, Sang B. Kim and Pablo G. Debenedetti designed and performed the molecular simulations. We thank Chester E. Markwalter and Robert K. Prudhomme for conducting the circular dichroism measurements.*

3.1 Introduction

Proteins generally remain stable over a narrow range of physiological conditions. Perturbations away from these conditions, such as changes in temperature, pressure or

ion concentration, often destabilize proteins, leading to partial or complete unraveling of their structure[35, 36, 37, 38, 39, 40, 41]. Fundamental understanding of protein stability as a function of temperature, pressure, or solute concentration is not only essential for a theoretical description of the physicochemical principles underlying protein folding and stability, but is also critical due to its relevance to industrial processing of proteins and biological materials. During the past decades, a vast number of studies have been performed aimed at understanding folding/unfolding over broad ranges of environmental perturbations. Heat denaturation of proteins is a well understood phenomenon that entails loss of secondary and tertiary structure, with associated configurational entropy gain. High pressure denaturation near ambient temperature is thought to be associated with modifications in the structure of hydration and bulk water, and cavities in the protein[136, 137, 138, 139, 140, 141]. Cold denaturation is believed to result in a partial form of structural unraveling[37, 142, 40, 143, 144, 145, 146]. Despite numerous studies aimed at investigating protein-ion interactions through Hofmeister ion effects, fundamental understanding of the relationship between ion concentration and protein stability is still incomplete[147, 148, 149].

In this work, we focus on room temperature ionic liquids (RTILs), organic salts that melt at temperatures below 100 °C. They are promising solvents for the solvation and separation of biomolecules due to their properties (high thermal, chemical and electrochemical stability, low volatility, tunable polarity by adjusting composition) that make them attractive from both fundamental and application perspectives[150, 151, 152, 153, 154, 155]. Notably, several enzymes have been shown to remain functional in the presence of RTIL/water mixtures; others have been shown to retain high levels of catalytic activity in pure ILs[154, 156, 157, 158, 159]. The yield from lignocellulosic biomass processing can be enhanced by biomass pretreatment with 1-ethyl-3-methylimidazolium acetate which has the rare ability to solvate crystalline cellulose[160, 161]. RTIL-containing solvents can alter reaction equilibria when com-

bined with enzymes such as lipases[162, 163]. In addition, RTILs can also be used to enable long-term protein storage[164, 165], extending the shelf life of therapeutics or industrially relevant proteins. While there are some heuristic rules for choosing protein-stabilizing RTILs based on the Hofmeister series[166, 167, 168, 169, 170, 171], there remain important gaps in basic understanding, such as would be needed to allow rational selection of favorable RTIL-protein combinations.

As several previous studies have demonstrated, RTIL-induced changes in protein structure can be investigated by molecular dynamics (MD) simulations[172, 173, 174]. Particularly, MD has been used to study the interactions of RTILs with various enzymes, including cellulases, xylanase, lipase and chymotrypsin.[175, 176, 174, 177, 178, 179, 180]. The protein-cation-solvent interactions have been investigated to determine the mechanism of action of RTILs on proteins. Most of these studies have used classical MD exclusively, or docking protocols coupled with spectroscopy[181, 182]. However, ionic liquid-induced unfolding is challenging to simulate due to the rapidly increasing solvent viscosity with ion concentration, which results in sluggish dynamics that frustrate sampling[181, 183, 184]. In order to overcome such challenges, Pfaendtner and colleagues employed classical MD in conjunction with the metadynamics family of enhanced sampling methods to study protein stability in ionic liquids[183, 184, 185]. These studies investigated ionic liquid-induced stabilization/destabilization mechanisms, but did not address the folding routes and thermodynamics of proteins in the conformation-temperature phase space.

Recent studies on protein stability at extreme conditions have shown that sampling challenges can be overcome by using replica exchange molecular dynamics (REMD)[186, 187, 40]. Here, we apply this approach to investigate the stability of the miniprotein Trp-cage in the presence of RTILs. We choose Trp-cage as our model protein due to its fast folding dynamics, and the fact that it possesses secondary structural features similar to those found in larger globular proteins. This combination of

favorable kinetics and realistic structure makes Trp-cage ideal for use in fundamental computational studies[188, 189, 190, 191, 192, 193]. In particular, despite having only 20 residues, Trp-cage has a cooperatively folded tertiary structure including a hydrophobic core with a tryptophan amino acid residue (W6), an N-terminal α-helix, a 3_{10}-helix, a C-terminal polyproline II segment, and a salt bridge between oppositely charged residues aspartic acid (D9) and arginine (R16). We report results from fully atomistic extensive REMD simulations and obtain folding/unfolding equilibrium phase diagrams for Trp-cage in the 290-500 K temperature range in aqueous solutions of Guanidinium Acetate ([Gdm][Act]) and 1-Ethyl-3-methylimidazolium Acetate ([EMIM][Act]). We complement the simulations of Trp-cage-[Gdm][Act]/water systems with Circular Dichroism (CD) measurements. We discuss [Gdm][Act] systems in Section 3.3, and report [EMIM][Act] results in Appendix 3.A. Our simulations with both [Gdm][Act] and [EMIM][Act] show that Trp-cage swells due to enhanced interaction with ionic liquid species, increasing the exposure of both hydrophilic and hydrophobic residues. We observe that the intrusion of ions and water into Trp-cage's hydrophobic core is facilitated by the disruption of its salt bridge and 3_{10}-helix. The intramolecular H-bonds of Trp-cage are replaced by solvent-protein H-bonds. Despite the partial disruption of Trp-cage's structure, however, its α-helix remains stable in the presence of the ionic liquid, exhibiting similarities to cold-induced denaturation[40]. Our results also show signs of RTIL-induced enhancement in the thermal stability of Trp-cage at high temperatures. We show that this behavior is due to the ionic liquid's ability to stabilize the α-helix.

3.2 Methods

3.2.1 Computational Methods

Protein Initial Configurations and Equilibration

We describe the simulation setup for [Gdm][Act] systems here, and report the details for [EMIM][Act] simulations in the Appendix 3.A. The NMR structure of Trp-cage was taken from the Research Collaboratory for Structural Bioinformatics Protein Data Bank (PDB ID code 1L2Y)[46]. Trp-cage was modeled using a modified version[194, 195] of the Amberff03 force field (Amberff03w), compatible with the TIP4P/2005 model of water[91]. [Gdm][Act] was modeled using the generalized Amber force field (GAFF)[194]. Electroneutrality of the system was achieved by adding a chloride ion to the system to counter the +1 net charge on Trp-cage. The initial topology files for the GROMACS simulation package[196] were generated with the pdb2gmx[197] utility. Trp-cage was solvated in 0 M, 1 M, 3 M and 5 M [Gdm][Act]/water mixtures.

To ensure the convergence of REMD results, two independent sets of calculations, starting from folded and thermally unfolded structures, were performed. The preparation of initial structures is as follows. First, to ensure that the system does not have any atomic overlaps, the Trp-cage/solvent systems were relaxed through energy minimization using the steepest descent method[196]. The solvent was then equilibrated at 300 K using the Berendsen thermostat[198] for 5 ns while position-restraining the protein under constant volume and temperature. The SETTLE algorithm is used to treat the water molecules as rigid[199]. Holonomic bond length constraints were applied to Trp-cage using the linear constraint solver algorithm (LINCS)[196]. A 1 nm cut-off is used for short-range interactions. The Particle Mesh Ewald (PME) technique[200] with a 0.1 nm grid spacing is used to treat the long-range electrostatics. The starting configurations with folded Trp-cage were obtained by equilibrating

the solvent using the Berendsen thermostat and barostat for 1 ns in the isothermal-isobaric ensemble. For the REMD simulations starting from the unfolded structure, the intial configurations were prepared by thermally unfolding Trp-cage for 15 ns at 530 K.

REMD Simulations

The REMD simulations which enhance the folding/unfolding transitions were performed using the GROMACS[196] simulation package to sample Trp-cage's folded and unfolded states at 56 temperatures ranging from 290 to 530 K, at 1 bar. Replica temperatures were determined by running several iterations of 150 ps-long REMD simulations. The distribution of replica temperatures was chosen to achieve a 20-25% acceptance rate for exchanges between adjacent states with exchange trials every 2 ps.

The REMD simulations were carried out in the isothermal-isobaric ensemble using the leapfrog algorithm with a 2 fs time step. The temperature and pressure were maintained using a Nosé-Hoover thermostat [201, 202] (0.2 ps time constant) and a Parrinello−Rahman barostat[203, 204] (2 ps time constant), respectively. A cut-off of 1 nm was used to truncate short-range interactions, and standard long-range dispersion corrections were applied to the energy and pressure. During the REMD simulations, the rigid structure of the TIP4P/2005 water molecules was maintained using SETTLE[199]. Holonomic bond length constraints were applied to Trp-cage using LINCS[196].

Simulations initiated from the folded structure were run for 2.5, 2.6 and 3.1 μs per replica for the 1 M, 3 M and 5 M systems, respectively. After their convergence is ensured, as described in the following section, the last 1.5, 1.6 and 2.1 μs of the trajectories were used for analysis. In concentrated ionic solutions, longer production times are used as slower dynamics frustrate sampling in these systems. Particularly,

the length of a production run was determined as fifteen times the correlation time of the fraction of folded proteins in all replicas, where the correlation time was defined as the value at which the time correlation function of the fraction of folded proteins in all replicas crosses zero for the first time.

REMD Simulations Convergence

In the thermodynamic limit, the fraction of time spent in folded configurations is equivalent to the ensemble average of the fraction of folded proteins. In order to accurately compute this quantity, we ensured the folding/unfolding equilibrium convergence of the simulations. For [Gdm][Act] calculations, convergence of the REMD simulations for the 0 M, 1 M and 5 M systems was demonstrated by performing independent sets of calculations initialized from folded and thermally unfolded Trp-cage structures (Figure 3.A.1).

Simulations initiated from the unfolded structure were run for 2.3 and 3.1 μs per replica for the 1 M and 5 M systems. The last 1.5 and 2.3 μs of each trajectory initiated from the unfolded structure was used for the analysis of 1 M and 5 M systems, respectively (Figure 3.A.1). The REMD simulation trajectories in pure water (0 M) were obtained from previous work[40]. Analysis of the trajectories showed that the two sets of REMD simulations converged after about 500 ns for the 0 M[40], and 800 ns for the 1 M and 5 M systems.

Standard errors were estimated from standard deviations of the mean obtained by dividing each trajectory into 3 blocks[205]. Particularly, the length of a block for a given system is five times the correlation time of the fraction of folded proteins in all replicas.

Thermodynamic Analysis

Thermodynamic analysis of the REMD simulations using a two-state population model requires defining an appropriate order parameter to distinguish between Trp-cage's folded and unfolded states. We identified two order parameters, namely the α-Carbon root-mean-squared deviation from the fully folded NMR reference structure (Cα rmsd) and the distance between the tryptophan residue (W6) and serine residue (S14) of Trp-cage (W6S14 distance). The Cα rmsd is defined as

$$C\alpha\ rmsd = [M^{-1} \sum_i m_i \left|\vec{r_i} - \vec{r}_{i,0}\right|^2]^{1/2} \tag{3.1}$$

where the sum is over all Cα atoms, M is the total mass of backbone Cα atoms, m_i is the mass of the atom i, r_i is the instantaneous position of the atom i, and $r_{i,0}$ is the position of the corresponding Cα atom in the least-squares fitted reference structure. W6 and S14 are two residues residing in Trp-cage's hydrophobic core and on its C-terminus, respectively, and the distance between them gives a measure of the widening of the U-shape of the protein.

The Cα rmsd and W6S14 distance distributions at 300 K (Figure 3.A.2) exhibit gaps at $\approx$ 0.3 nm and $\approx$ 0.42 nm that separate the peaks associated with Trp-cage's native and denatured states. Consequently, for the purpose of our analysis, structures with Cα rmsd$\leq$0.3 nm and W6S14 distance$\leq$0.42 nm were considered to belong to the ensemble of folded configurations.

The Gibbs free-energy change of unfolding (ΔG) was then calculated at each state point using,

$$\Delta G = G_u - G_f = -RTln\Big(\frac{1-x}{x}\Big) \tag{3.2}$$

where x is the fraction of folded proteins or, equivalently, the probability of observing a single Trp-cage unit in its folded state. The associated enthalpy and entropy change of unfolding were computed by fitting a cubic polynomial to ΔG and using

the thermodynamic relationships

$$\Delta S = -\Big(\frac{\partial \Delta G}{\partial T}\Big)_P \quad \text{and} \quad \Delta H = \Big(\frac{\partial \Delta G/T}{\partial 1/T}\Big)_P \tag{3.3}$$

Structural Analysis

Changes in Trp-cage's overall structure were characterized by constructing the free energy surfaces associated with the order parameters Cα rmsd and W6S14 distance. Free energy surfaces were constructed via

$$G = -RTln(p) + c \tag{3.4}$$

where R is the gas constant, T is the temperature, c is an additive constant whose value can be set to 0, and p is the normalized probability assigned for the chosen order parameters obtained by collecting histograms of the average occupation of the Cα rmsd - W6S14 distance space.

Geometric criteria were employed to define hydrogen bonds, in which a bond was considered to be formed if the donor-acceptor distance was less than 0.35 nm and the donor-hydrogen-acceptor angle was less than 30°[206]. We considered OH and NH groups as donors, and nitrogen and oxygen atoms as acceptors.

The electrostatic interaction between oppositely charged residues arginine (D9) and aspartic acid (R16) of Trp-cage stabilizes its folded structure. We investigated the formation of a salt bridge between these residues by monitoring the shortest distance between the charged oxygen and nitrogen atoms of D9 and R16, respectively. The salt bridge was considered to be formed, as will be discussed in the text, when the D9-R16 distance was less than 0.5 nm.

3.2.2 Experimental Methods

Materials

The trifluoroacetic acid (TFA) salt of the Trp-cage variant TC5b with a purity of 95.4% was obtained from Genscript, Inc. (Piscataway, NJ). The molecular weight of Trp-cage matched the theoretical value (2169.4) as determined by ESI-mass spectrometry. Mass purity was determined to be 90.5% by thermogravimetric analysis which measured residual solids content after evaporation of water and TFA. [Gdm][Act] and anhydrous sodium phosphate monobasic buffer were obtained from Sigma-Aldrich. Anyhydrous sodium phosphate dibasic was obtained from Fisher Scientific. All reagents were used as received.

Unfolding Curve by Circular Dichroism

[Gdm][Act] was dissolved in 50 mM phosphate buffer (pH 6.95) at the target concentration (0 M, 1 M, 3 M). Each solution was degassed and filtered. 60 mM TC5b solutions were gravimetrically prepared using each stock, correcting for the mass purity of TC5b. Circular dichroism spectra at 222 nm and 230 nm were collected at 1 K increments using a Chirascan CD Spectrometer (Applied Photophysics, Leatherhead, UK). Temperature ramping at 0.5 K/min was carried out by a TC125 temperature controller (Quantum Northwest, Liberty Lake, WA) and a Julabo AWC100 recirculating cooler. Each wavelength was sampled for 25 seconds. Molar ellipticity values were determined from the raw CD data and the known TC5b molarity. Helix fraction was calculated from ellipticity as in Heyda et al. [192] The method assumes a linear relationship between the ellipticity at 222 nm and helical fraction, based on a Lifson-Roig model of the helix-coil transition. Additionally, the unfolded content was determined using the method and reported baselines of Neidigh et al.[46]. To address

the high absorbance of [Gdm][Act] at 222 nm, a linear fit of the unfolding curve for the 0 M case was applied to the data at 230 nm for all cases.

3.3 Results and discussion

Stability and Thermodynamics of Trp-cage

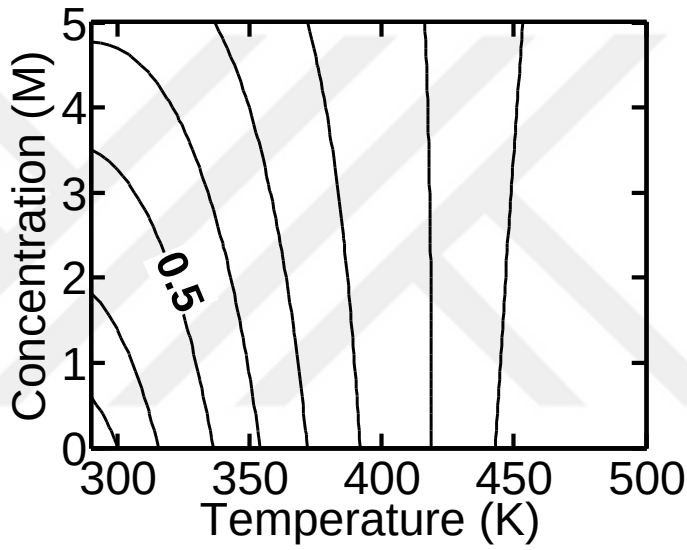

Figure 3.1: Stability diagram of Trp-cage from simulation data at 0 M, 1 M, 3 M and 5 M. Curves are contours of constant folded fraction at 0.05, 0.1, 0.2, 0.3, 0.4, 0.5, 0.6 and 0.65, right to left.

Based on the Cα rmsd and W6S14 distance profiles depicted in Figure 3.A.2 and the two-state model of Anson[207], the folded state of Trp-cage is defined as the ensemble of configurations where the Cα rmsd is less than 0.3 nm and W6S14 distance is less than 0.42 nm. Using this definition, we construct the temperature(T)-concentration(C) stability diagram for Trp-cage in aqueous [Gdm][Act] mixtures by creating a set of 2-D grid points in the T-C plane and linearly interpolating the simulation data to compute the corresponding fraction folded values at grid points.

The fraction folded profiles exhibit elliptical shapes in the 290-420 K range (Figure 3.1), suggesting that the protein can be denatured at constant ion concentration by increasing the temperature or by increasing the ion concentration at constant temperature. Trp-cage's stability in [Gdm][Act]/water mixtures obtained from our simulations (Figure 3.2(a)) is in qualitative agreement with fraction folded Trp-cage profiles from Circular Dichroism (CD) measurements Figure 3.2(b).

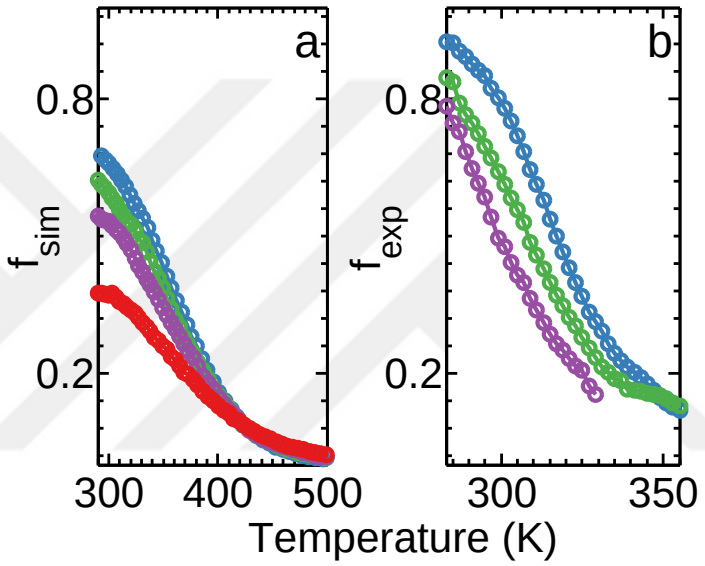

Figure 3.2: Temperature dependence of (a) fraction of folded Trp-cage (REMD), (b) fraction of folded Trp-cage (CD measurements) at various [Gdm][Act] concentrations. Blue denotes pure water; green 1M; purple 3M; red 5M.

At temperatures above 420 K, an apparent stabilization of Trp-cage with increasing ion content is observed (Figure 3.2). Figure 3.3(a) suggests that, as will be discussed below in more detail, this apparent stabilization is due to an overall increase in Trp-cage's α-helical content upon increasing [Gdm][Act] content at high temperatures. The fraction of α-helical content measured by CD (Figure 3.3(b)) also qualitatively captures this trend. In particular, Figure 3.3(b) shows that α-helical stability decreases monotonically with ionic liquid content in the 283-350 K range, but an apparent crossover of the curves corresponding to 0 M and 1 M is observed at

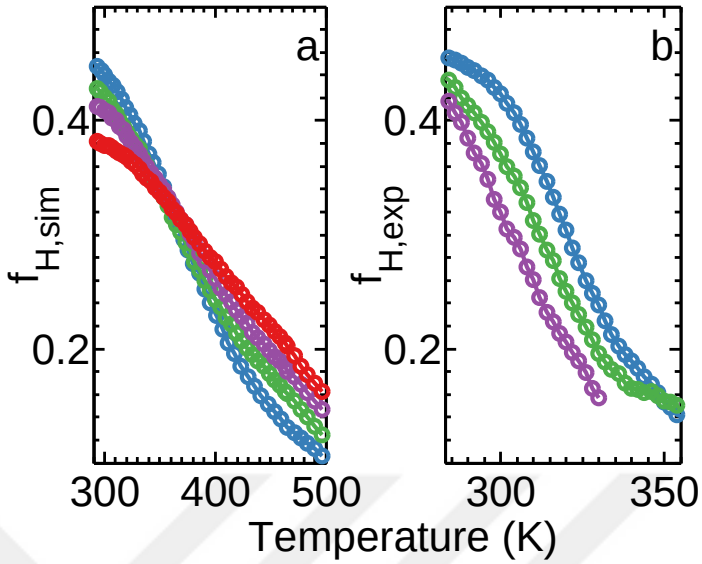

Figure 3.3: Temperature dependence of (a) helix fraction of Trp-cage (REMD), and (b) helix fraction of Trp-cage (CD measurements) as a function of [Gdm][Act] concentration. Blue denotes pure water; green 1 M; purple 3 M; red 5 M.

≈350 K. This is in agreement with experimental work which indicates stabilization of secondary structure elements in the presence of RTILs [208, 209].

The parabolic temperature dependence of ΔG (Figure 3.4) is characteristic of globular proteins that undergo heat denaturation[210]. The largest value of ΔG (1.8 kJ/mol) is observed in pure water at 290 K, where the folded fraction reaches its maximum. This free energy estimate is in agreement with experimental studies of Trp-cage that report values of $\Delta G \approx 3$ kJ/mol near ambient conditions in pure water[191]. Unfolding becomes favorable as the folded fraction drops below 0.5 and ΔG becomes negative. This threshold, referred as the melting temperature, is crossed at 342 K in pure water (Figure 3.4). We observe that the melting temperature of Trp-cage decreases with ionic liquid concentration (330 K at 1 M, and 320 K at 3 M), and at 5 M, ΔG becomes negative across the entire temperature range sampled in this work. This is in line with experimental studies of proteins, which predict denaturation and enzyme deactivation in the presence of guanidine-based ionic liquids[192]. We note that our simulations predict higher nominal melting temperatures (fraction folded

= 0.5) than the experimental values obtained from CD measurements, as shown in Figure 3.2(b) (317 K, 308 K and 299 K at 0 M, 1 M and 3 M, respectively), but they capture well the qualitative concentration dependence of Trp-cage's stability and the relative change in the melting temperature.

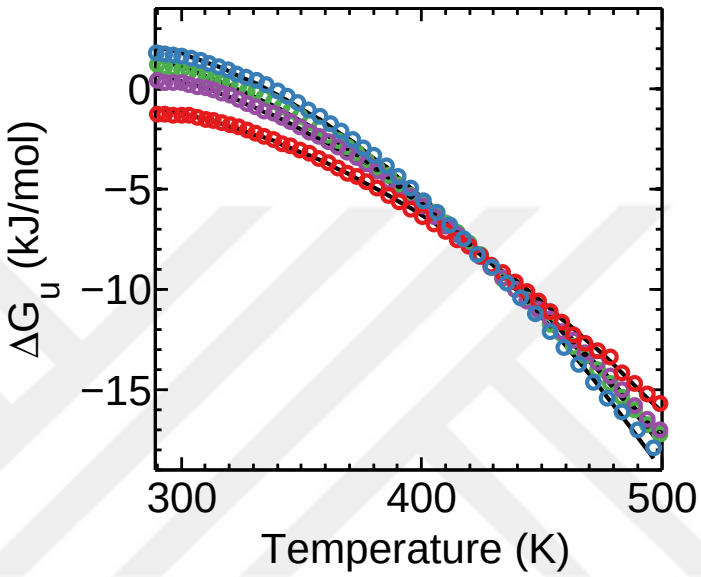

Figure 3.4: Free energy change of unfolding for Trp-cage as a function of temperature and [Gdm][Act] concentration. Blue denotes pure water; green 1 M; purple 3 M; red 5 M. Error bars are smaller than the symbols.

Figure 3.5 indicates that within the entire region studied, unfolding is endothermic ($\Delta H\ (T,C)>0$) with positive entropy change, ($\Delta S\ (T,C)>0$). Figure 3.5(a) shows that increasing [Gdm][Act] content reduces ΔH, eventually making RTIL-induced unfolding athermal at 5 M near room temperature. In this regard, the effect of the RTIL on the unfolding thermodynamics of Trp-cage is similar to the effect of decreasing the temperature in pure water in the subzero temperature range[40]. We note that this mechanism differs significantly from thermal denaturation, where increasing temperature decreases ΔH and increases ΔS.

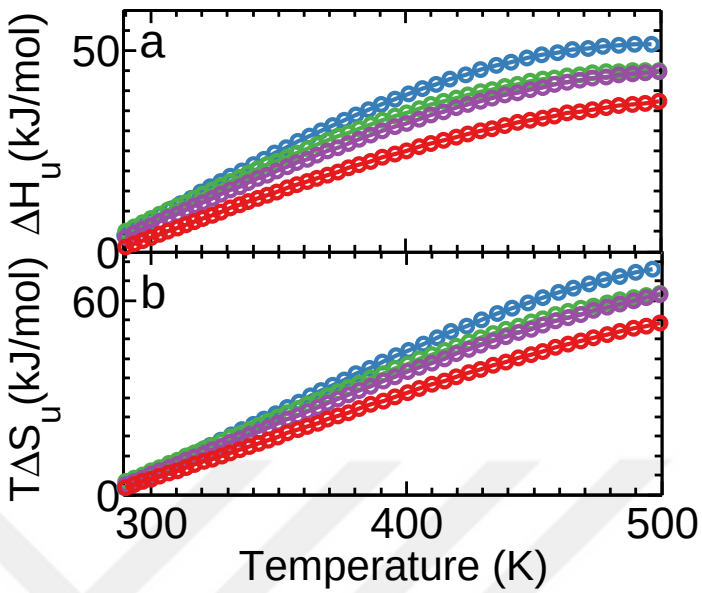

Figure 3.5: (a) Enthalpic, and (b) entropic contributions to the free energy change of unfolding for Trp-cage as a function of temperature and [Gdm][Act] concentration. Blue denotes pure water; green 1M; purple 3M; red 5M. Quantities computed from the thermodynamic relationships (Eq.3) applied to cubic polynomial fits to the calculated ΔG curves (Figure 3.4).

RTIL-induced Effects on the Structure of Trp-cage

Experiments can capture the principal thermodynamic signatures of RTIL-induced denaturation. Fully atomistic simulations give additional insight by providing a detailed microscopic description. To this end, changes in Trp-cage's overall structure have been characterized by constructing the free energy surfaces associated with the order parameters Cα rmsd and W6S14 distance. Figure 3.6 shows these free energy surfaces at 300 K for 0 M, 1 M, 3 M and 5 M, as well as the most frequently observed structures for the labeled basins that are obtained by clustering analysis (Appendix 3.A). We also construct the free energy surfaces at 210 K and 496.5 K (Figure 3.7) to compare RTIL-induced denaturation to cold unfolding and thermal unfolding mechanisms.

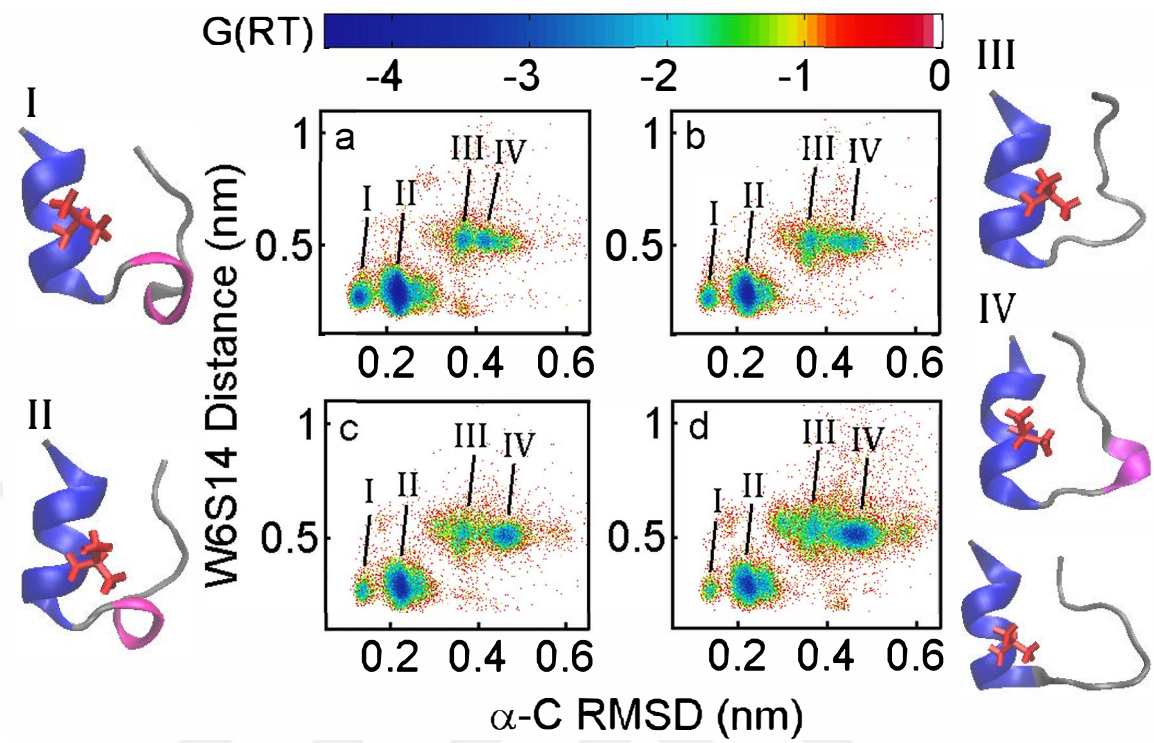

Figure 3.6: The free energy surfaces associated with the order parameters Cα rmsd and W6-S14 distance for (a) 0 M, (b) 1 M, (c) 3 M, and (d) 5 M at 300.0 K. The protein structures show representative configurations for labeled basins.

The two local minima (I and II) in Figure 3.6 correspond to folded Trp-cage states. The representative conformations of these minima differ by the formation of the N-terminal backbone hydrogen bond between asparagine (N1O) and glutamine (Q5H) residues, in line with NMR results identifying ensembles of native structures of Trp-cage where the N-terminal backbone hydrogen bond (N1O−Q5H) is either formed (I) or broken (II) [211]. States III and IV are partially unfolded structures that remain relatively compact with stable α-helices. The representative structure of state III differs from the native fold only in the absence of its 3_{10}-helix (residues 11-13). There are two frequently observed configurations in basin IV. One exhibits a shift in the position of its 3_{10} turn helix (residues 12-14). Despite shifting position, however, the α-helix and 3_{10} turn helix of this fold remain stable. A second one is a configuration with a destabilized 3_{10} turn helix, bend (residues 14-16) and turn structure,

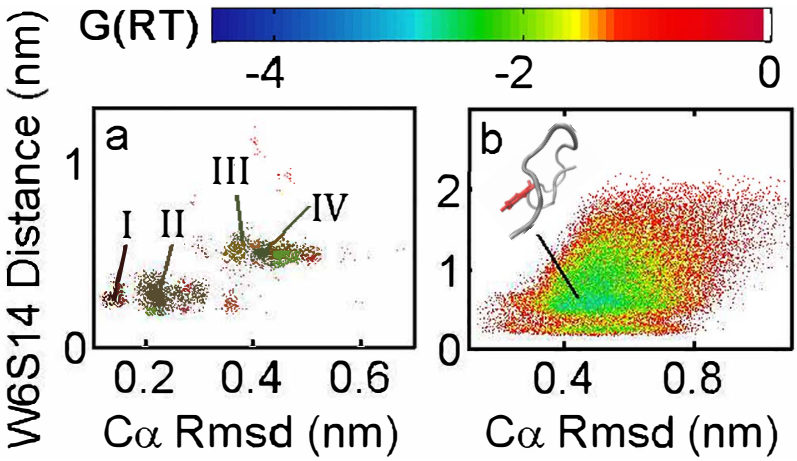

Figure 3.7: The free energy surfaces associated with the order parameters Cα rmsd and W6-S14 distance for (a) 230 K, and (b) 465 K at 0 M.

and a disrupted hydrogen bond between residues 8 and 10. We observe that increasing [Gdm][Act] concentration favors the equilibrium of conformational states to shift towards partially unfolded states (III and IV). This denaturation mechanism shows considerable resemblance to cold-induced unfolding (Figure 3.7(a)) and the reader is referred to recent work by Kim et al.[40] for more details on Trp-cage's cold unfolding mechanism. On the other hand, RTIL-induced denaturation is significantly different from heat denaturation (Figure 3.7(b)), where the unfolded states are distinguished from the native fold by nearly complete unraveling of elements of the secondary and tertiary structure.

Next, we analyze global conformational properties obtained from simulations to characterize Trp-cage at different ion concentrations. As depicted in Figure 3.8(a), the W6S14 distance increases with [Gdm][Act] concentration. Residues W6 and S14 are located in the hydrophobic core and on the C-terminus of Trp-cage, respectively. They are in close proximity in the folded structure, because of Trp-cage's U-shape. This increased separation at high [Gdm][Act] content therefore suggests a widening of Trp-cage's U-shape and resembles the shift in the W6S14 distance during cold unfolding (Figure 3.8(a)). We also note that the increase in Trp-cage's solvent-accessible-

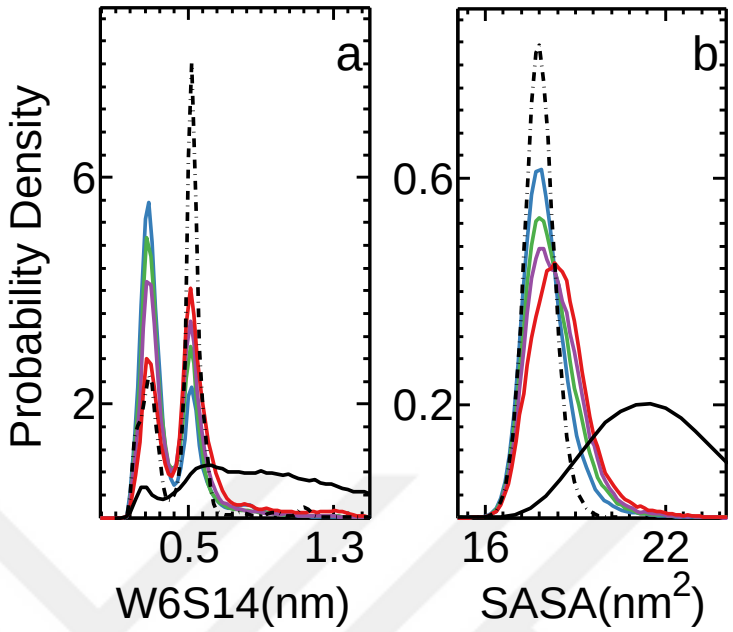

Figure 3.8: Probability distribution of (a) distance between residues W6 and S14 (1/nm), and (b) solvent accessible surface area (1/nm^2) at 300 K (blue denotes pure water; green 1 M; purple 3 M; red 5 M) and at 0 M (black dashed line denotes 230 K and black solid line 465 K).

surface-area (SASA), as will be discussed below, is due to the exposure of the protein residues, particularly the residues in the hydrophobic core, to the surrounding solvent (Figure 3.8(b)). These structural changes are much more local and subtle than those observed at high temperatures (Figure 3.8).

Hydration and Ion-Protein Interactions

To investigate the increased exposure of the hydrophobic core to the solvent in the presence of [Gdm][Act], we compute the number of solvent molecules surrounding each residue. A solvent molecule is considered to be near a residue if any of its non-hydrogen atoms is found to be within 0.4 nm of any atoms on the residue. Figure 3.9 shows that the exposure of Trp-cage's residues to both ions is enhanced with increasing ionic liquid concentration. This results in less favorable intramolecular protein-protein interactions. Particularly, we investigate the behavior of Trp-cage's salt bridge by

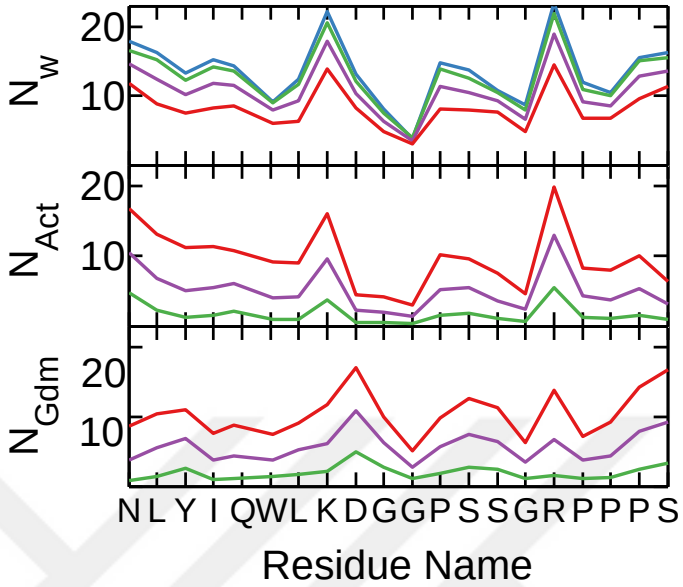

Figure 3.9: Average number of water molecules (N_w), acetate ions (N_{Act}), and guanidinium ions (N_{Gdm}) within 0.4 nm of each residue at 300 K. Blue denotes pure water; green 1 M; purple 3 M; red 5 M.

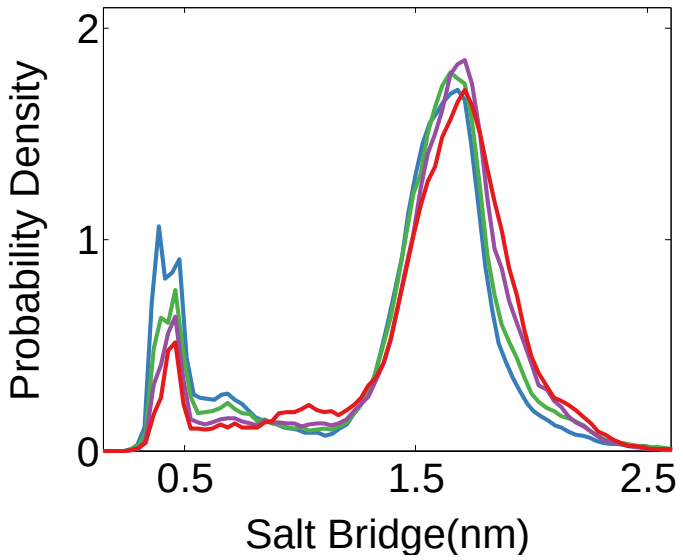

Figure 3.10: Probability distribution of the distance between salt bridge forming residues D9 and R16 at 300 K. Blue denotes pure water; green 1 M; purple 3 M; red 5 M.

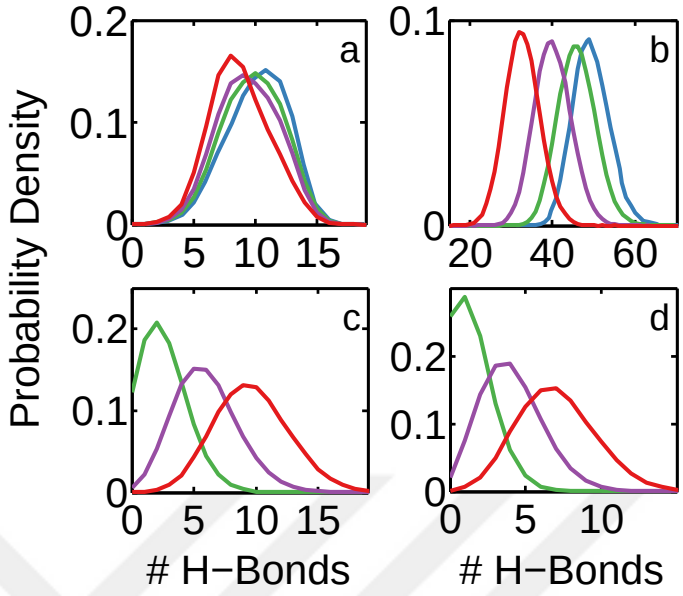

Figure 3.11: Probability distribution of the number of (a) protein-protein, (b) protein-water, (c) protein-acetate, and (d) protein-guanidinium H-bonds at 300 K. Blue denotes pure water; green 1 M; purple 3 M; red 5 M.

monitoring the distance between the oxygen and nitrogen atoms on the side chains of residues aspartic acid (D9) and arginine (R16), respectively (Figure 3.10). The distribution of D9-R16 distances show that the salt bridge between these residues forms when the two residues are separated by less than 0.5 nm. At all conditions examined, we observe that the salt bridge loses stability upon increasing [Gdm][Act] concentration, as evidenced by the fact that states in which the salt bridge is intact become less populated at high ion concentrations.

The weakening of intramolecular interactions with increasing ionic liquid content is revealed also by the decrease in the number of intramolecular H-bonds formed within Trp-cage's structure (Figure 3.11). These are offset by the increase in the number of acetate-protein and guanidinium-protein H-bonds (Figure 3.11). Guanidinium, which can make H-bonds via the NH_2 groups along its edges despite having hydrophobic faces, is capable of hydrogen bonding even with nonpolar residues that are part of Trp-cage's hydrophobic core, such as tryptophan (W6), glycine (G11) and proline

(P18). This promotes the exposure of the residues in the hydrophobic core to the solvent and the disruption of Trp-cage's tertiary structure. Computing the average number of protein-ion H-Bonds formed upon increasing the ion content from 1 M to 5 M at 300 K, we also find that on average 12 of the 14 protein-ion H-bonds are between ions and hydrophilic residues, indicating that hydration of hydrophilic residues enthalpically favors unfolding.

3.4 Conclusions

We have investigated the RTIL-induced folding/unfolding of an α-helical miniprotein with a hydrophobic core, using fully atomistic REMD simulations, and compared our results to CD measurements. The stability diagram in the C-T plane exhibits an elliptical shape in the 290-420 K range, suggesting destabilization of Trp-cage at constant ion concentration with increasing temperature, or at constant temperature with increasing ion concentration. At temperatures above 420 K, an apparent stabilization of Trp-cage with increasing ion content is observed.

The mechanism of RTIL-induced denaturation resembles cold unfolding, where the equilibrium of conformational states shifts towards partially unfolded configurations. The partially unfolded states observed in RTIL systems are populated by configurations that conserve secondary structure elements, as opposed to completely unraveled states. In particular, we observe widening of Trp-cage's hydrophobic core due to the disruption of its salt bridge and intramolecular H-bonds. Despite this deformation, however, Trp-cage's α-helix remains stable, giving rise to the apparent stabilization at high temperatures.

Denaturation, which is entropically driven at ambient and higher temperatures in pure water despite unfavorable enthalpy, becomes less endothermic in the presence

of RTILs. This is due the formation of additional solvent-protein H-bonds in RTILs, that offset the positive ΔH from the disruption of intramolecular protein H-bonds.

Finally, we demonstrate that sampling challenges associated with studying protein stability using all-atom models when dynamics are slow, can be overcome using REMD. We predict that increasing processing power combined with improved advanced sampling techniques will facilitate the study of larger globular proteins and enable the calculation of complete (C, P, T) stability diagrams for such systems.

3.A Appendix

3.A.1 Convergence of REMD Simulations

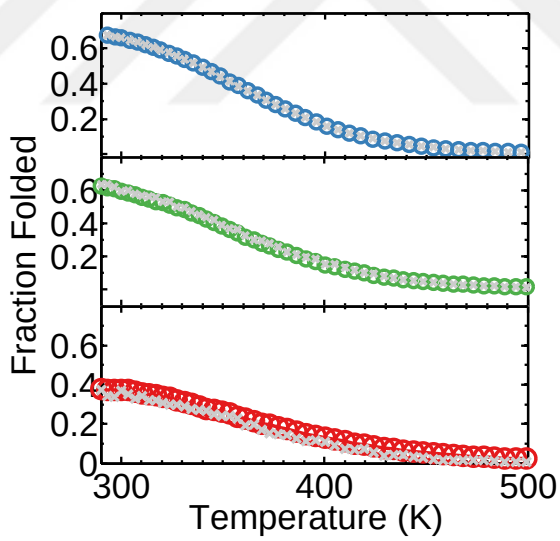

Figure 3.A.1: Fraction of folded proteins computed from two independent sets of REMD simulations. The first set is initialized from a configuration in the folded state (circles), whereas the second set is initialized from a thermally unfolded structure (stars). Blue denotes pure water; green 1M; red 5M.

The fraction of folded proteins is equal to 1 at all temperatures in the initial configurations of the first set, while it is 0 in the second set. The fraction of folded

Trp-cage distributions obtained from the two sets after equilibration are very similar, indicating that equilibrium has been reached.

3.A.2 Order Parameter for the Selection of Folded/Unfolded States

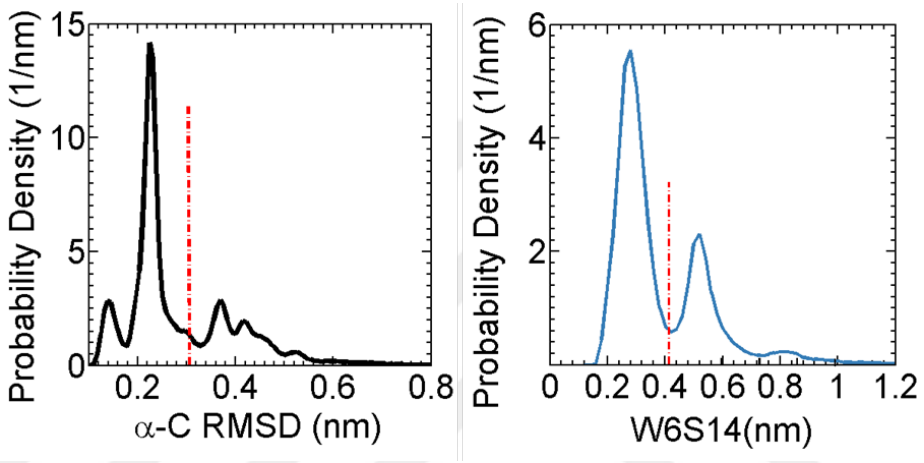

Figure 3.A.2: Probability distribution of (a) Cα rmsd (b) W6S14 distance at 300K. A cut-off of 0.3 nm and 0.42 nm are chosen to distinguish between folded and unfolded configurations, respectively.

3.A.3 Determination of the Representative Configurations

In order to identify the representative configurations in Figure 3.6, clustering analysis based on Cα rmsd was performed. Particularly, the structures within $k_{\mathrm{B}}T$ of a free energy basin are extracted and the structural diversity of the free energy basins was assessed by using the *gcluster* utility of GROMACS using the *gromos* algorithm[212]. Cluster analysis of basins I, II and III yielded a single dominant structure throughout a given basin. On the other hand, there are two high-frequency clusters identified in basin IV. The proportion of structures that belong to the dominant clusters in each state is given in Table 3.1.

Table 3.1: Fraction of the structures that belong to the main cluster of a free energy basin

	I	II	III	IV
0 M	1	0.991	0.933	0.357 and 0.543
1 M	1	0.989	0.931	0.237 and 0.663
3 M	1	0.981	0.927	0.211 and 0.670
5 M	1	0.981	0.887	0.175 and 0.637

3.A.4 Analysis for [EMIM][Act] Systems

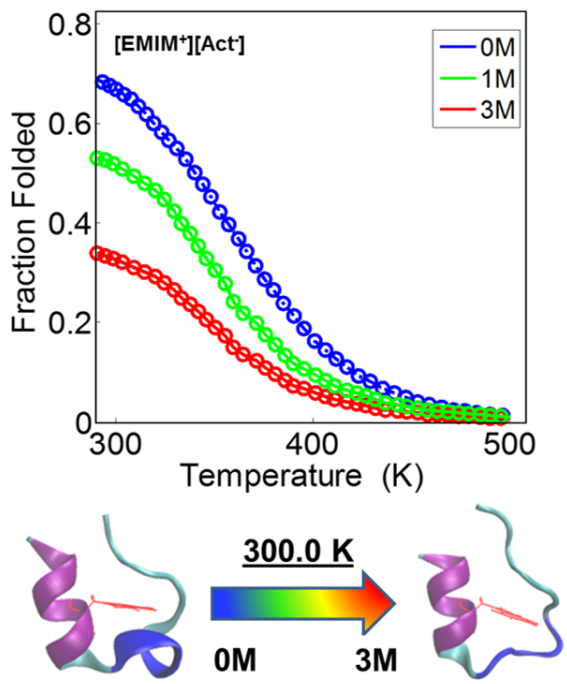

Figure 3.A.3: Fraction of folded Trp-cage as a function of temperature and [EMIM][Act] concentration.

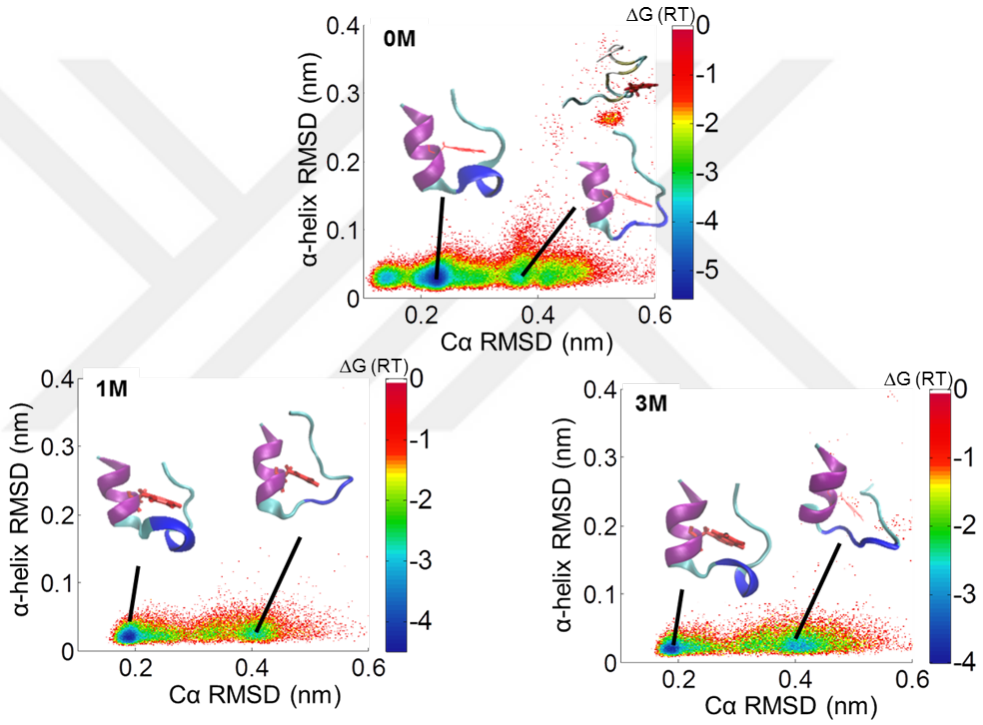

Figure 3.A.4: The free energy surfaces associated with the order parameters Cα rmsd and α-helix rmsd at 300 K (0 M, 1 M and 3 M) for [EMIM][Act]. The protein structures show representative configurations for the indicated basins.

Chapter 4

Computational Investigation of the Effect of High Pressure on Protein Stability

4.1 Introduction

From the frigid waters of the Antarctic Ocean to deep-sea hydrothermal vents, and from the high altitudes of the Andes to high-pressure depths of the oceans, life can exist in environments usually referred to as "extreme", by comparison to the comparatively mild conditions characteristic of human life. The existence of organisms that thrive under such conditions (extremophiles) prompts questions, both fundamental and applied. The former have to do with understanding the molecular mechanisms underlying life at extremes of temperature, pressure, or solvent composition. The latter address the possible use of biomolecules in technological processes over broad ranges of thermodynamic conditions.

Proteins carry within their functional, native structures the key to many essential life processes[38]. Hence, understanding how changes in temperature[213, 214, 137,

215], pressure[216, 217, 218, 214, 137, 215, 136, 219, 41, 220, 221, 222], pH[216, 217] or solvent composition[223, 224, 51], affect protein stability is of interest in both of the above contexts. Thermal denaturation has significant implications for understanding thermophiles and nearly all high-temperature technical applications[225]. High pressure effects have implications in food processing[140], the study of aquatic organisms[226] and disease-causing misfolding/aggregation events[227]. Cold unfolding is relevant to lyophilization[228] as well as to the study of freeze-tolerant species[229]. Accordingly, gaining a fundamental understanding of protein stability across broad ranges of environmental perturbations has attracted interest for more than a century[213, 230, 231, 232, 233].

Contours of constant folded fraction in the (P,T) plane are a convenient way of displaying protein stability[234, 235, 236, 237, 233, 238, 219]. Experimental studies using calorimetric[239, 240, 241], spectroscopic[214, 137, 217, 236, 215, 141] and imaging[141] methods, as well as molecular simulations[221, 41, 222, 219] are commonly used to construct such diagrams, thereby shedding light on the underlying transitions commonly referred to as thermal, cold, and pressure denaturation. Thermal denaturation is commonly explained as an entropy-driven phenomenon in which proteins unfold as a result of exposure of the hydrophobic side chains that are buried in the interior of the folded protein to the surrounding solvent[242]. Cold unfolding is linked to the energetically-favored hydration of hydrophobic residues[242, 243, 244, 245, 142], although recent studies suggest that hydration of hydrophilic groups may also play a significant role[246, 40]. High pressure denaturation near ambient temperature is associated with structural perturbations resulting from water penetration into buried protein cavities[217, 236, 215, 233]. The construction of stability diagrams spanning broad ranges of temperature and pressure is challenging on account of the constraints imposed by extreme conditions on both experiments and simulations[236, 237, 236].

In particular, the direct observation of protein behavior at conditions involving both low temperatures and high pressures is hindered by freezing of the solvent in experiments (since cold unfolding conditions usually lie below waters freezing point)[247, 248, 249], or sluggish dynamics in simulations because of the solvent's large viscosity[40]. Thus, experiments often involve the small subset of proteins that cold-denature above the freezing point of water[248, 249], or systems whose thermophysical properties are altered by additives that prevent crystallization[250, 241]. Alternatively, cold-induced unfolding has been studied by protein confinement in reverse micelles[144, 251], and in emulsified water microdroplets[241].

Computational or theoretical studies using coarse-grained models[213, 242, 252] can be performed, but these lack atomistic-level information and consequently, have a limited ability to describe proteinwater interactions realistically. So far, complete protein stability diagrams have been obtained by thermodynamic integration, parametrized using data from a limited pressure and temperature range[236, 237, 215, 222]. Atomistic molecular dynamics simulations have been also performed to understand the effect of temperature and pressure perturbations on protein stability, but these studies did not aim to construct full stability diagrams[186, 219, 45, 41, 187].

In this work, we examine the stability of the Trp-cage miniprotein at temperatures between 210 and 420K in the pressure range 1 bar to 5 kbar using replica-exchange molecular dynamics (REMD) simulations, and we construct the resulting stability diagram from fully atomistic simulation data. We observe that Trp-cages stability decreases with increasing pressure at room temperature and above, but it exhibits a nonmonotonic dependence on pressure at lower temperatures. Cold unfolding and thermal denaturation mechanisms differ significantly at ambient pressure and become progressively similar with increasing pressure. At ambient pressure, Trp-cage cold-unfolds into a relatively compact state with elements of its secondary structure significantly conserved, while the tertiary and secondary structure of Trp-cage is more

significantly disrupted at its melting temperature. On the other hand, cold unfolding at high pressure shares progressively more structural features with thermal denaturation. The pressure stabilization of Trp-cage at lower temperatures may carry broader implications for species that live at extreme pressures, including the single-cell protist *Foraminifera* found in the deepest parts of oceans, such as the Marianas Trench[253]. It may also be of relevance to the development of processes such as the manufacture and preservation of biotherapeutics, food sterilization and storage, and the production of biofuels.

4.2 Results and Discussions

4.2.1 Thermodynamics of Trp-cage

Recent computational studies on protein stability under extreme conditions have shown that sampling challenges can be overcome by using REMD[186, 187, 40]. In this work, we apply this approach to construct the phase diagram of the miniprotein Trp-cage over the temperature and pressure ranges 210-420K and 1 bar-5 kbar from fully atomistic simulation data without the need to invoke free energy expansions. We chose Trp-cage as our model protein due to its fast folding kinetics and the fact that in spite of its short chain length (20 amino acids) it possesses secondary structural features characteristic of larger globular proteins[188, 189, 222, 45, 190].

In order to compute changes in thermodynamic and structural properties upon unfolding, we analyze trajectories from 4-5 microsecond-long REMD simulations, using the two-state folding model of Anson[207]. This approach requires defining appropriate order parameters to distinguish between Trp-cages folded and unfolded states. Here, we use a combination of two order parameters, namely, the root-mean-squared deviation of Trp-cages alpha carbon (Cα) atoms from the fully folded reference NMR structure[46] (Cα rmsd), and the minimum distance between any atoms of the tryp-

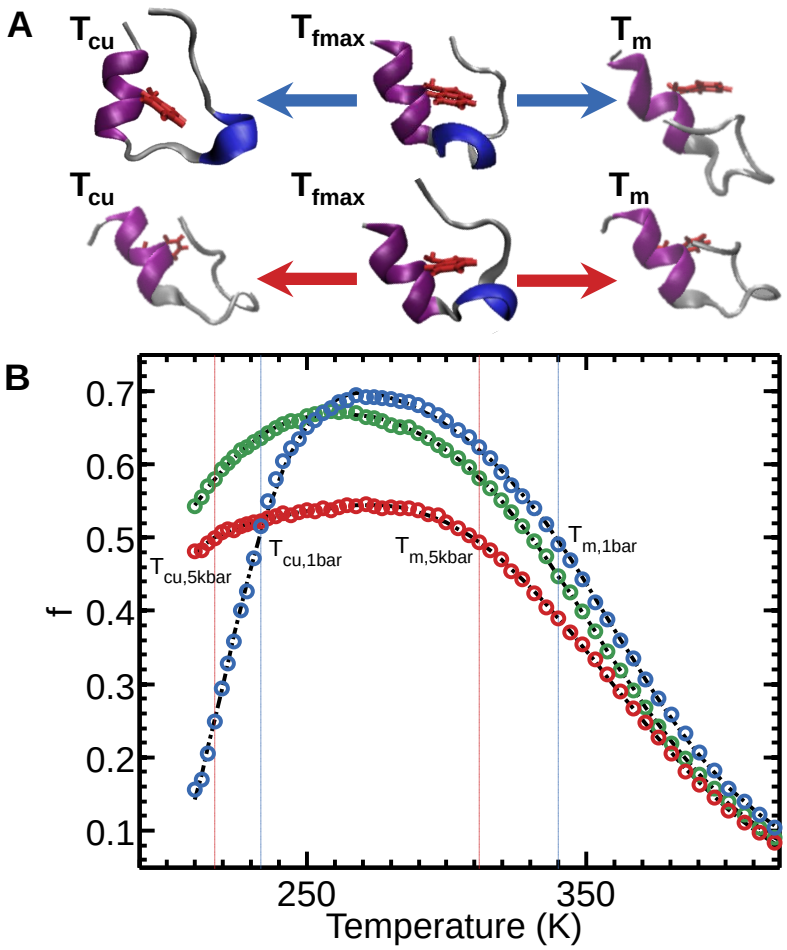

Figure 4.1: (A) Representative protein configurations from the most populated states at the cold unfolding temperature (T_{cu}), melting temperature (T_{m}) and the temperature at which the folded fraction is a maximum (T_{fmax}) at 1 bar and 5 kbar. Trp-cage's α-helix, 3_{10}-helix, and aromatic side chain of residue W6 are colored in purple, blue, and red, respectively. (B) Equilibrium folded fraction as a function of temperature, at three pressures. Blue: 1 bar; green: 2 kbar; red: 5 kbar.

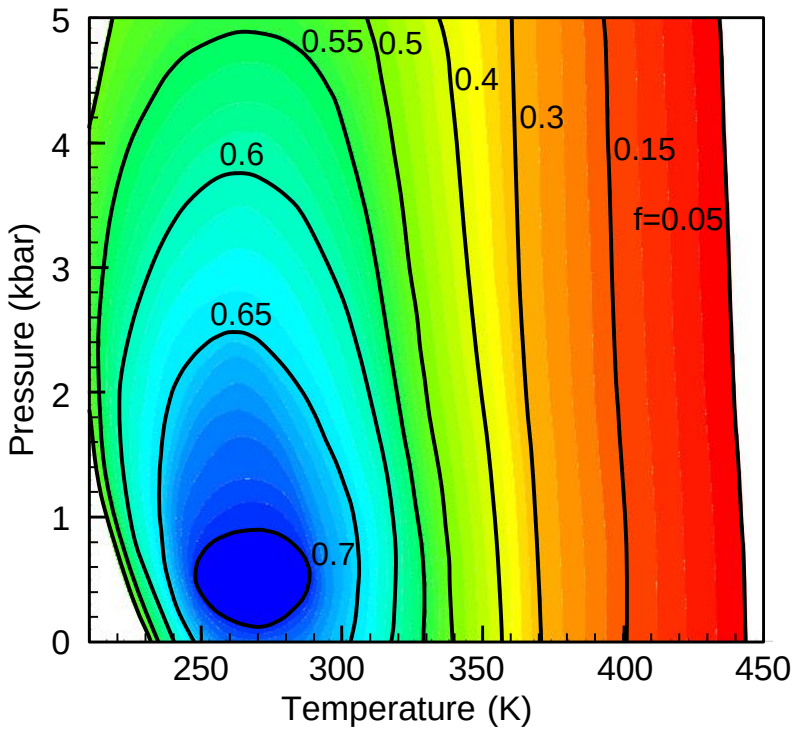

Figure 4.2: Stability diagram of Trp-cage in the (P,T) plane, obtained from simulation data. The equilibrium folded fraction (f) is constant along a contour line.

tophan (W6) and serine (S14) residues (W6S14 distance). W6 and S14 reside in Trp-cage's hydrophobic core and at its C-terminus, respectively, and the minimum distance between them is a measure of Trp-cage's U-shape. Based on the Cα rmsd and W6S14 distance profiles depicted in Figure 4.A.2, we define the folded state as the ensemble of configurations with a Cα rmsd less than 0.3 nm and a W6S14 distance less than 0.42 nm.

Figure 4.1(a) depicts representative configurations for the unfolded populations at the cold unfolding (T_{cu}), and melting (T_{m}) temperatures, at which the populations of folded and unfolded configurations are equal, and for the folded populations at the temperature at which the folded fraction is maximum (T_{fmax}), at ambient pressure and at 5 kbar. The temperature dependence of the fraction of folded states exhibits parabolic shapes (4.1(b)) that are characteristic of proteins which undergo both low- and high-temperature unfolding. Increasing the pressure destabilizes Trp-

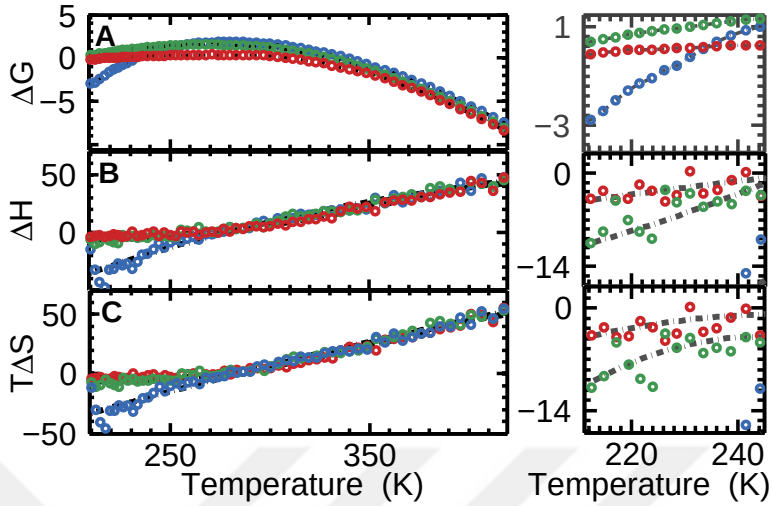

Figure 4.3: (A) The free-energy change upon unfolding (ΔG) (kJ/mol), and the corresponding (B) enthalpic ΔH (kJ/mol) and (C) entropic $T\Delta S$ (kJ/mol) contributions, as a function of temperature. Blue: 1 bar; green: 2 kbar; red: 5 kbar. Inset shows the limiting behavior of ΔG, ΔH and $T\Delta S$ at low temperatures.

cage's folded state at temperatures above ≈250K. On the other hand, below ≈250K, Trp-cage's stability exhibits a nonmonotonic dependence on pressure.

We next translate this information into a phase diagram in the (P,T) plane (Figure 4.2). In particular, we construct the stability diagram by creating a set of grid points showing folded fraction in the (P,T) plane and interpolating the simulation data from isobaric REMD simulations (see Figure 4.A.3 for fraction of folded protein profiles at 1 bar, 500 bar, 1 kbar, 2 kbar and 5 kbar) using cubic splines. We then compute the corresponding ΔG according to

$$\Delta G = G_{\mathrm{u}} - G_{\mathrm{f}} = -RT\ln(\frac{1-f}{f}) \tag{4.1}$$

where f is the probability of observing Trp-cage in its folded state (or, equivalently, folded protein fraction at the given temperature and pressure where the protein concentration is low enough so that protein units do not interact), R is the gas constant and T is the temperature. We find that the contours along which f, or equivalently

ΔG, is constant exhibiting elliptical shapes (Figure 4.2) as previously suggested by two-state thermodynamic models[215, 236, 237, 222]. In order to gain insight into the interplay between different thermodynamic quantities that drive the stabilization/destabilization of Trp-cage as a function of temperature and pressure, we next investigate the enthalpic and entropic contributions to ΔG (Figure 4.3).

We compute ΔH by averaging the instantaneous values of H for the folded and unfolded states and taking the difference between them. We use the relationship $\Delta S = (\Delta H - \Delta G)/T$ to calculate ΔG. Figure 4.3(a) shows that within the pressure range explored in this work, $\Delta G(T_{\text{fmax}})$ is in the 1-2.5 kJ/mol range. This estimate is in agreement with experimental studies of Trp-cage that report values around $\Delta G \approx$ 3 kJ/mol near ambient conditions [254]. The fact that ΔG is very similar to RT (2.4 kJ/mol) at ambient conditions indicates that the folded and unfolded states of Trp-cage are in dynamic equilibrium. Both T_{fmax} and $\Delta G(T_{\text{fmax}})$ decrease with pressure, accompanied by a decrease in the melting and cold unfolding temperatures. When the pressure is increased from 1 bar to 5 kbar, the thresholds of stability shift from 232K to 218K (T_{cu}), and from 340K to 311K (T_{m}). Figure 4.3(b-c) indicate a remarkable enthalpy-entropy compensation, whereby the change in enthalpy upon unfolding is largely compensated by a corresponding change in entropy, resulting in small ΔG. The $T \geq T_{\text{fmax}}$ behavior of ΔH and ΔS is largely insensitive to pressure (Figure 4.3(b-c)). In particular, thermal denaturation of Trp-cage at temperatures above T_{fmax} is entropically driven, with positive entropy and enthalpy changes upon unfolding.

On the other hand, cold unfolding of Trp-cage depends significantly on pressure. Cold unfolding at 1 bar is enthalpically driven ($\Delta H < 0$) and entropically disfavored ($\Delta S < 0$) (Figure 4.3(b-c)). As seen in Figure 4.A.5, this favorable enthalpic effect comes from protein-water interactions which overcome the enthalpic penalty associated with the disruption of protein-protein and water-water interactions. On

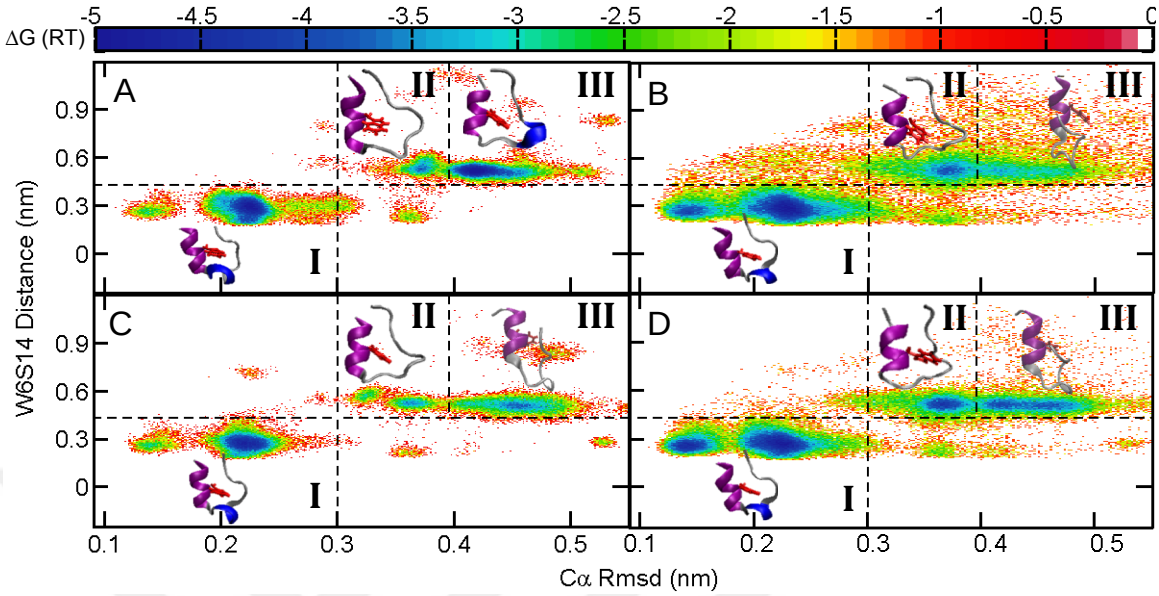

Figure 4.4: The free energy surfaces associated with the order parameters Cα rmsd and W6-S14 distance for (A) 1 bar, T_{cu}= 232 K, (B) 1 bar, T_{m} = 340 K, (C) 5 kbar, T_{cu} = 218 K, and (D) 5 kbar, T_{m} = 311 K. The protein structures show the representative configurations corresponding to the given regions. Dotted lines represent the boundaries for regions I: $C\alpha$ rmsd $\leq$ 0.3 nm and W6S14 distance $\leq$ 0.42 nm; II: 0.3 nm $\leq$ $C\alpha$ rmsd $\leq$ 0.4 nm and W6S14 distance $\geq$ 0.42 nm; III: $C\alpha$ rmsd $\geq$ 0.4 nm and W6S14 distance $\geq$ 0.42 nm.

the other hand, at elevated pressures, cold unfolding entails ΔH and $T\Delta S$ becoming very small and largely balancing each other (Figure 4.3(b-c)). This very small net enthalpic effect at high pressures results from favorable protein-water interactions, and unfavorable protein-protein and water-water interactions offsetting each other largely, as shown in Figure 4.A.5.

4.2.2 Pressure- and Temperature-Induced Effects on the Folding Landscape of Trp-cage

We monitor the changes in Trp-cage's overall structure by constructing the free energy surfaces associated with the order parameters $C\alpha$ rmsd and $W6S14$ distance, and analyze the representative protein configurations of the populated states at T_{cu} and

T_{m}, at atmospheric pressure and at 5 kbar (Figure 4.4). The free-energy surfaces are constructed using

$$G = -RT\ln(p) + C \tag{4.2}$$

where R is the gas constant, p is a histogram approximation to the configuration density, and C is a normalization constant. We characterize the populations present in the free energy surfaces by focusing on three regions of the order parameter plane (I: $C\alpha$ rmsd ≤ 0.3 nm and $W6S14$ distance ≤ 0.42 nm; II: 0.3 nm $< C\alpha$ rmsd ≤ 0.4 nm and $W6S14$ distance > 0.42 nm; III: $C\alpha$ rmsd > 0.4 nm and $W6S14$ distance > 0.42 nm).

Region I contains the basins corresponding to folded configurations; regions II and III contain the basins corresponding to unfolded configurations. We note that we define regions II and III as the ensemble of unfolded populations based on the Cα rmsd and W6S14 distance metrics introduced in the previous section. Consequently, rather than structures that are completely structurally unraveled, as would occur, e.g. at temperatures considerably higher than T_m (Figure 4.A.9), regions II and III are comprised of partially unfolded configurations with a Cα rmsd greater than 0.3 nm, and W6S14 distance greater than 0.42 nm. The ensemble of folded conformations, located in region I exhibit similar features regardless of the system temperature and pressure (Figure 4.4(a-d). In particular, they exhibit two local minima, both of which are defined by a hydrophobic core with an enclosed tryptophan amino acid residue, an N-terminal α-helix between residues 2-8, a 3_{10}-helix between residues 11-13, a C-terminal polyproline II segment, and a metastable salt bridge between oppositely charged residues D9 and R16 (Figure 4.A.6). These two minima differ trivially, and only by the existence of a N-terminal backbone hydrogen bond (N1O-Q5H), in line with NMR results that identify ensembles of native structures of Trp-cage where the N1O-Q5H bond is either formed or broken[46].

Representative configurations for the populations in regions II and III are depicted in Figure 4.4. Configurations in region II are relatively insensitive to temperature and pressure. They differ from the folded state only in the absence of Trp-cage's 3_{10}-helix (residues 11-13), and a slight decrease in the alpha-helical propensity of residue L2 (Figure 4.A.7). On the other hand, configurations in region III are highly sensitive to temperature and pressure. We observe that cold unfolded and thermally unfolded structures in region III differ significantly at ambient pressure (Figure 4.4(a-b)), while they become progressively similar at high pressures (Figure 4.4(c-d)). Specifically, the representative configuration in region III at 1 bar and $T_{\mathrm{cu}} = 232$K is relatively compact with a stable α-helix and a 3_{10}-helix that exhibits a shift with respect to its position with respect to the folded structure (from residues 11-13 to 12-14) (Figure 4.4(a)). By contrast, at 5kbar and $T_{\mathrm{cu}} = 218$K (Figure 4.4(c)), the representative configuration in region III is replaced by a structure with a destabilized 3_{10}-helix, bend (residues 14-16) and turn structures and loss of the hydrogen bond between residues 8 and 10. The disruption of the bend and the hydrogen bond between residues 8 and 10 results in the significant exposure of the hydrophobic core to the surrounding solvent, in contrast to the cold-unfolded conformation with a partially conserved hydrophobic core at ambient pressure. This significant exposure is also apparent from the protein-water H-bond profiles in Figure 4.A.8 that show enhanced hydration of the nonpolar residues at high pressures. The representative structure of Region III at 5 kbar (Figure 4.4(c)) is significantly similar to the unfolded structures at T_{m} (Region III in Figure 4.4(b,d)), confirming that cold- and heat-unfolded states become progressively similar at high pressures.

To gain further structural insight into the differences between cold-unfolding and heat denaturation mechanisms at ambient and high pressures, we investigated the exposure of Trp-cage to the solvent upon unfolding. To this end, we computed the change in the solvent accessible surface area upon unfolding ($\Delta SASA_{\mathrm{u}}$) (Fig-

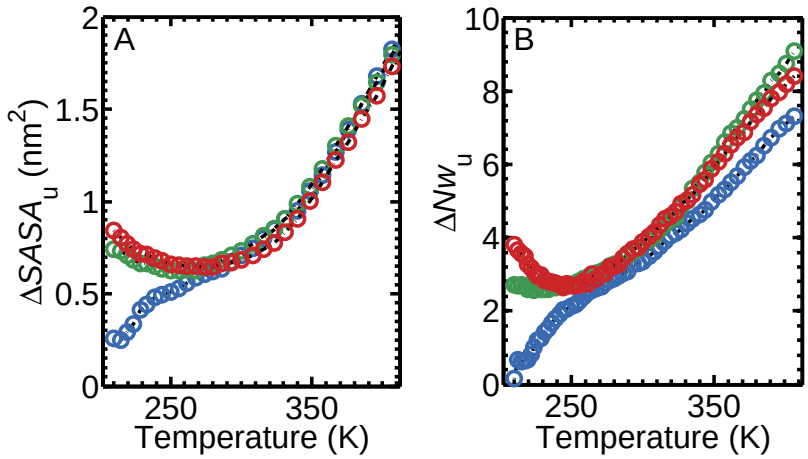

Figure 4.5: (A) The change in solvent accessible surface area upon unfolding ($\Delta SASA_{\mathrm{u}}$), (B) the change in the number of water molecules around residue W6 upon unfolding (ΔNw_{u}). Blue denotes 1 bar; green: 2 kbar; red: 5 kbar.

ure 4.5(a)) and the change in the number of water molecules around residue W6 upon unfolding (ΔNw_{u}) (Figure 4.5(b)). We computed $\Delta SASA_{\mathrm{u}}$ by averaging over the instantaneous values of $SASA$ over configurations belonging to the folded and unfolded states. We computed ΔNw_{u} from averaging over the number of oxygen atoms that belong to water molecules, which are found to be within 0.4 nm of any aromatic side chain atoms of residue W6 which is enclosed in folded Trp-cage's hydrophobic core. Figure 4.5 shows that, independent of pressure, heat denaturation results in an increase in $\Delta SASA_{\mathrm{u}}$ and ΔNw_{u}. In fact, at sufficiently high temperatures, Trp-cage completely unravels, losing both the secondary and tertiary structure elements of the native fold and exposing all residues to water (see Figure 4.A.9 for representative configurations at ≈417 K). In contrast, cold unfolding exhibits quite different trends at ambient and high pressures. At elevated pressures, $\Delta SASA_{\mathrm{u}}$ and ΔNw_{u} increase with decreasing temperature. Thus, at elevated pressures, reducing or increasing temperature away from T_{fmax} leads to increases in $\Delta SASA_{\mathrm{u}}$ and ΔNw_{u}, similar to thermal unfolding. In contrast, at ambient pressure, cooling (heating) away from T_{fmax} leads to progressively smaller (larger) increases in $\Delta SASA_{\mathrm{u}}$ and ΔNw_{u}.

4.2.3 Conclusions

In this work, we examine the stability of the Trp-cage miniprotein at temperatures between 210 and 420K in the pressure range 1 bar to 5 kbar, employing REMD simulations. We construct the stability diagram in the (P,T) plane, and show that contours along which the folded fraction is constant display elliptical shapes. Trp-cage's stability decreases with increasing pressure at room temperature and above, but it exhibits a nonmonotonic dependence to pressure at low temperatures. The fully atomistic, water-explicit simulations show that while cold unfolding and thermal denaturation mechanisms differ significantly at ambient pressure, they become progressively similar at high pressures, consistent with a dome-shaped stability region. At 1 bar, the dominant structure observed at Trp-cage's melting temperature has its tertiary and secondary structure disrupted but Trp-cage cold-unfolds into a relatively compact state with elements of its secondary structure significantly conserved. On the other hand, at high pressures, the cold- and thermally-unfolded states share similar degrees of secondary and tertiary structural perturbation.

Employing fully atomistic simulations to construct stability diagrams for larger globular proteins remains prohibitively expensive. We anticipate that progress in hardware, software and sampling algorithms will facilitate the construction of full (P,T) stability diagrams and enable the investigation of the effect of environmental perturbations on folding/unfolding mechanisms of larger proteins in broad ranges of thermodynamic conditions, which can not be easily obtained by experiments.

4.A Appendix

4.A.1 Simulation Details

Protein Initial Configurations and Equilibration

The NMR structure of Trp-cage was taken from the Research Collaboratory for Structural Bioinformatics Protein Data Bank (PDB ID: 1L2Y)[46]. Trp-cage was modeled using a modified version of the Amberff03 force field (Amberff03w[194]), compatible with the TIP4P/2005 model of water[91]. The topology files for the GROMACS simulation package[196, 255] were generated with the pdb2gmx utility[256, 255]. The initial structures for the replica-exchange molecular dynamics (REMD) simulations are then prepared as follows. Trp-cage is solvated in 2,910 water molecules in a cubic box of 89 nm^3 in volume. Electroneutrality of the system was achieved by adding a chloride ion to the system to counter the +1 net charge on Trp-cage. The system is relaxed by energy minimization using the steepest descent method in order to remove atomic overlaps. Water is then equilibrated using the Berendsen thermostat[198] for 5 ns while position-restraining the protein under constant volume at 298 K. The SETTLE algorithm is used to treat the water molecules as rigid[199]. Holonomic bond length constraints are applied to Trp-cage using the linear constraint solver algorithm (LINCS)[196]. A 1 nm cutoff is used for short-range interactions. The particle mesh Ewald (PME) technique[200] with a 0.1 nm grid spacing is used to treat the long-range electrostatics.

To ensure the convergence of REMD results, two independent sets of simulations (starting from folded and thermally unfolded structures) are performed at 2 kbar and 5 kbar. The starting configurations with folded Trp-cage are obtained by equilibrating the solvent using the Berendsen thermostat and barostat[198] for 1 ns in the isothermal-isobaric ensemble. For the REMD simulations starting from the unfolded structure, the initial configurations are prepared by thermally unfolding Trp-cage for 15 ns at 530 K and 1 bar. Only one set of simulations starting from unfolded structures is performed at 500 bar and 1 kbar. Simulations at 500 bar and 1 kbar are used to aid in improving the precision of the contour lines in the stability diagram of

Trp-cage (Figure 4.2).

REMD Simulations

The REMD simulations were carried out in the isothermal-isobaric ensemble using the leapfrog algorithm with a 2 fs time step at 84 temperatures ranging from 210 to 580 K at 1 bar, 500 bar, 1 kbar, 2 kbar and 5kbar. The temperature and pressure were maintained using a Nos-Hoover thermostat[201, 202] (0.2 ps time constant) and a Parrinello-Rahman barostat[203, 204] (2 ps time constant), respectively. A cut-off of 1 nm was used to truncate short-range interactions, and standard long-range dispersion corrections were applied to the energy and pressure. Long-range contributions to the electrostatic interactions were treated using the smooth-particle mesh Ewald method with a 0.1 nm grid spacing. During the REMD simulations, the rigid structure of the TIP4P/2005 water molecules was maintained using the SETTLE algorithm[199]. Holonomic bond length constraints were applied to Trp-cage using the linear constraint solver algorithm LINCS[196]. Replica temperatures for nearly constant acceptance ratios were determined from a few iterations of short, 150 ps-long REMD simulations. The distribution of replica temperatures was chosen to achieve a 20-25% acceptance rate for exchanges between adjacent states with exchange trials every 2 ps.

REMD Simulation Convergence

In the thermodynamic limit, the fraction of time a single protein spends in folded configurations is equivalent to the fraction of folded proteins. In order to accurately compute this quantity, we ensured the folding/unfolding equilibrium convergence of the simulations. At 2 kbar and 5 kbar, convergence of the REMD simulations was demonstrated by performing independent sets of calculations initialized from folded and thermally unfolded Trp-cage structures (Figure 4.A.1). The simulations initiated from folded structures were run for 3, 3.1, 3.8 and 6 μs for the 500 bar, 1 kbar, 2 kbar and 5 kbar systems, respectively. The REMD simulation trajectories in pure

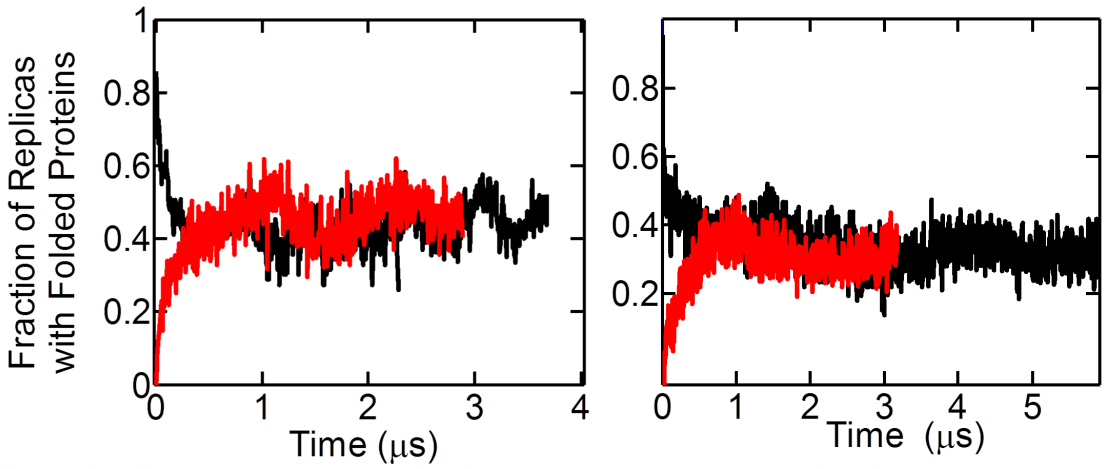

Figure 4.A.1: Fraction of folded proteins computed from two independent sets of REMD simulations for (a) 2 kbar, (b) 5 kbar. The first set of REMD simulations was initialized from a thermally unfolded Trp-cage structure (red), folded configurations was used to initiate the second set (black).

water were obtained from previous work[40]. Simulations initiated from the unfolded structures were run for 2.9 and 3.3 μs per replica for the 2 kbar and 5 kbar systems. Analysis of the trajectories showed that the two sets of REMD simulations converged after about 500 ns for the 2 kbar and 900 ns for the 5 kbar system. Standard errors for fraction folded were estimated from standard deviations of the mean obtained by dividing each trajectory into three blocks[205]. Images of Trp-cage's structure were rendered using the Visual Molecular Dynamics package[257].

4.A.2 Structural Analysis

Thermodynamic analysis of the REMD simulations using a two-state population model requires defining an appropriate order parameter to distinguish between Trp-cage's folded and unfolded states. We identified two order parameters, namely, the Cα root-mean-squared deviation from the fully folded NMR reference structure1 (Cα rmsd) and the minimum distance between any atoms of the tryptophan (W6) and

serine (S14) of Trp-cage (W6S14 distance). The Cα rmsd is defined as

$$C\alpha\ rmsd = [M^{-1} \sum_i m_i \left|\vec{r_i} - \vec{r}_{i,0}\right|^2]^{1/2} \tag{4.3}$$

where the sum is over all Cα atoms, M is the total mass of backbone Cα atoms, m_i is the mass of the atom i, r_i is the instantaneous position of the atom i, and $r_{i,0}$ is the position of the corresponding Cα atom in the least-squares fitted reference structure. W6 and S14 are two residues residing in Trp-cage's hydrophobic core and on its C-terminus, respectively, and the distance between them gives a measure of the widening of the U-shape of the protein.

The Cα rmsd (Figure 4.A.2(a)) and W6S14 distance (Figure 4.A.2(b)) distributions at 300 K exhibit gaps at ≈0.3 nm and ≈0.42 nm, respectively, that separate the peaks associated with Trp-cage's native and denatured states. The free energy surface in Figure 4.A.2(c) also clearly identify these gaps. Consequently, for the purpose of our analysis, structures with Cα rmsd $\leq$ 0.42 nm and W6S14 distance $\leq$ 0.42 nm were considered to belong to the ensemble of folded configurations. Fraction folded profiles computed using this criteria are given in Figure 4.2.

4.A.3 Thermodynamic Analysis

The free energy of unfolding in the isobaric-isothermal ensemble can be expressed as

$$\Delta G = \Delta H - T\Delta S \tag{4.4}$$

As discussed in Section 4.3, while cold unfolding at 1 bar is enthalpically driven ($\Delta H \leq 0$) and entropically disfavored ($\Delta S \leq 0$), at elevated pressures ΔH and TΔS become very small and largely balance each other. In order to explore the structural origins of these thermodynamic trends, we decomposed the total interaction energy of unfolding (ΔE) into three contributions $\Delta E = \Delta E_{\mathrm{pp}} + \Delta E_{\mathrm{ww}} + \Delta E_{\mathrm{pw}}$, namely

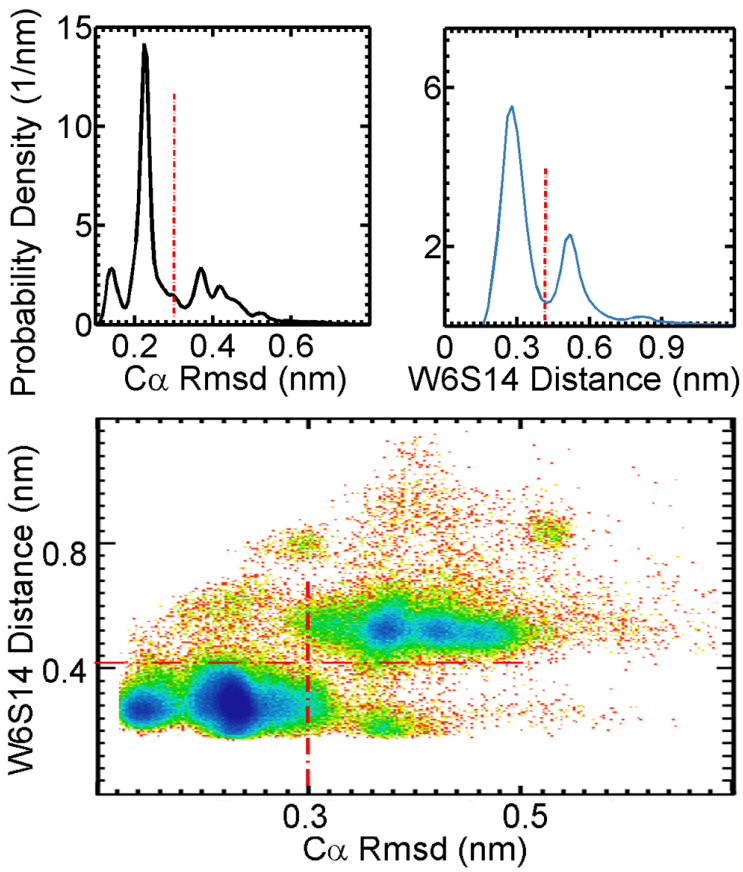

Figure 4.A.2: Order parameters for the selection of folded/unfolded states. Probability distribution of (a) Cα rmsd (b) W6S14 distance at 300K and 1 bar. (c) The free energy surface associated with the order parameters Cα rmsd and W6S14 distance at 300K and 1 bar.

intramolecular protein-protein (ΔE_{pp}), and intermolecular solvent-solvent (ΔE_{ww}) and protein-solvent (ΔE_{pw}) interactions (Figure 4.A.5). This is achieved by averaging and integrating the van der Waals and electrostatic contributions (i.e., Lennard-Jones and Coulombic potentials) for protein-protein (E_{pp}), water-water (E_{ww}), and protein-water (E_{pw}) interactions for the folded and unfolded configurations, and computing the difference between them. We note that considering the interaction energy suffices since, due to Trp-cage's small size, the contribution to ΔH arising from the volume change of unfolding (PΔV) is negligible (Figure 4.A.4).

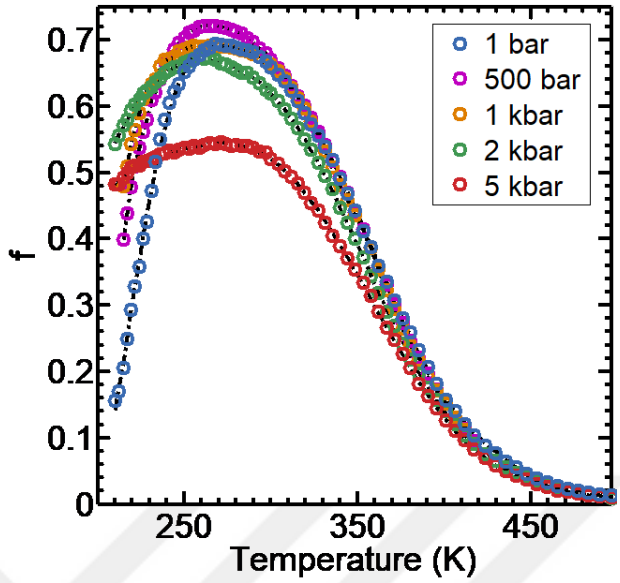

Figure 4.A.3: Equilibrium folded fractions as a function of temperature at 1 bar, 500 bar, 1 kbar, 2 kbar and 5 kbar.

4.A.4 Salt Bridge Profiles

Strong electrostatic interactions between oppositely charged residues D9 and R16 indicates the formation of a salt bridge that stabilizes the native fold of Trp-cage. We note that this salt bridge is metastable in the folded state, i.e. configurations with a stable and a disrupted salt bridge coexist in the folded basin (region I in Figure 4.4). We investigated the behavior of the Trp-cage's salt bridge by monitoring the distance between oxygen and nitrogen atoms on the side chains of residues D9 and R16, respectively (Figure 4.A.6). The D9R16 distance distribution shows that the salt bridge forms when the two residues are separated by less than 0.5 nm. The salt bridge loses stability upon increasing the pressure of the system at the cold unfolding temperature (T_{cu}). This is evidenced by the fact that states in which the salt bridge is stable become less populated at 5 kbar (Figure S5a). The reduced stability of the salt bridge shows that the electrostatic interactions in Trp-cage become weaker at high pressures.

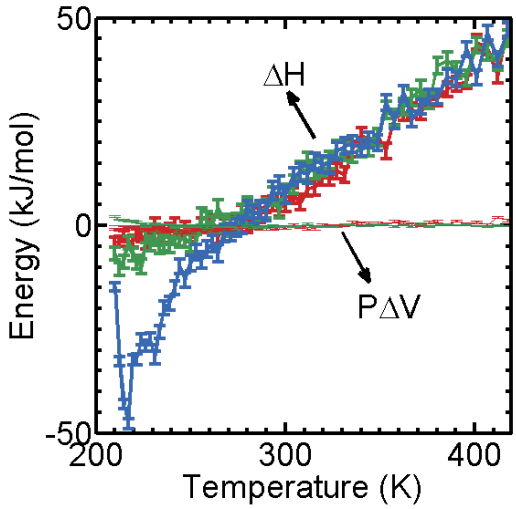

Figure 4.A.4: Enthalpy of unfolding (ΔH) and the contribution to ΔH from the volume change of unfolding ($P\Delta V$) as a function of temperature. Blue denotes 1 bar; green: 2 kbar; red: 5 kbar.

4.A.5 Trp-cage's α-helical propensity

Configurations in region II differ from the folded state only in the absence of the 3_{10} helix (residues 11-13), and a slight decrease in the alpha-helical propensity of residue L2. This slight decrease is depicted in Figure 4.A.7 as the probability of residue L2 to be in α-helical state in the three regions (Region I, II, III) of the parameter plane.

4.A.6 Hydrogen Bond Profiles

Geometric criteria were employed to define hydrogen bonds, in which a bond was considered to be formed if the donor-acceptor distance was less than 0.35 nm and the donor-hydrogen-acceptor angle was less than 30°[206]. We considered OH and NH groups as donors, and nitrogen and oxygen atoms as acceptors.

Figure 4.A.8 depicts the effect of cold unfolding on the probability distribution of the number of H-bonds formed between water and nonpolar amino acids (NonpolarAA), and between water and polar amino acids (PolarAA) in Trp-cage. We observe that both at ambient pressure and high pressures, the dominant contribution

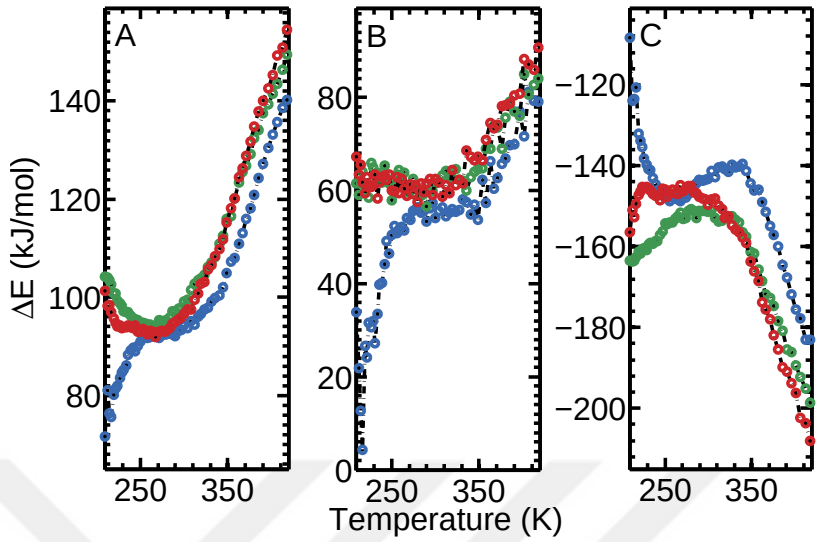

Figure 4.A.5: Decomposition of the energy change upon unfolding. (A) intramolecular protein-protein, (B) water-water, and (C) protein-water contributions. Blue denotes 1 bar; green, 2 kbar; red, 5 kbar.

to the hydration comes from hydrophilic residues (Figure 4.A.8(b)). Nevertheless, at high pressures, hydration of nonpolar residues is also significant (Figure 4.A.8(a)) in agreement with the observation that the exposure of Trp-cage's hydrophobic core to water upon cold unfolding is enhanced at high pressures (Figure 4.4).

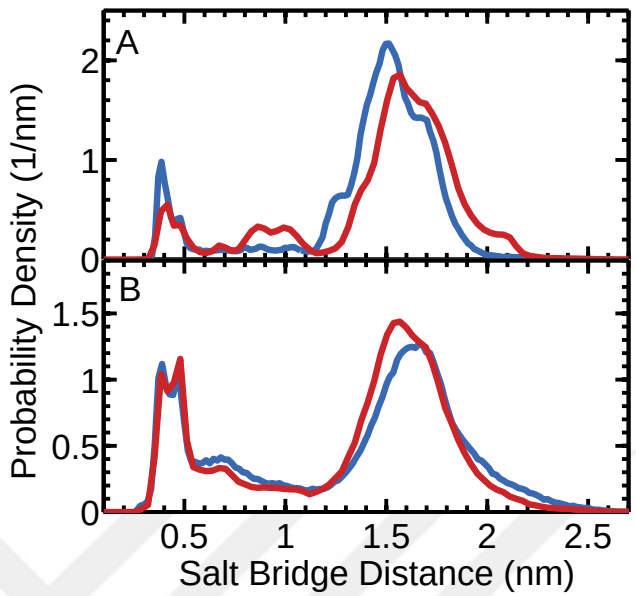

Figure 4.A.6: Probability distribution of the distance between salt bridge-forming residues D9 and R16 at (a) the cold unfolding temperature (T_{cu}), (b) the melting temperature (T_m). Blue denotes 1 bar; red: 5 kbar.

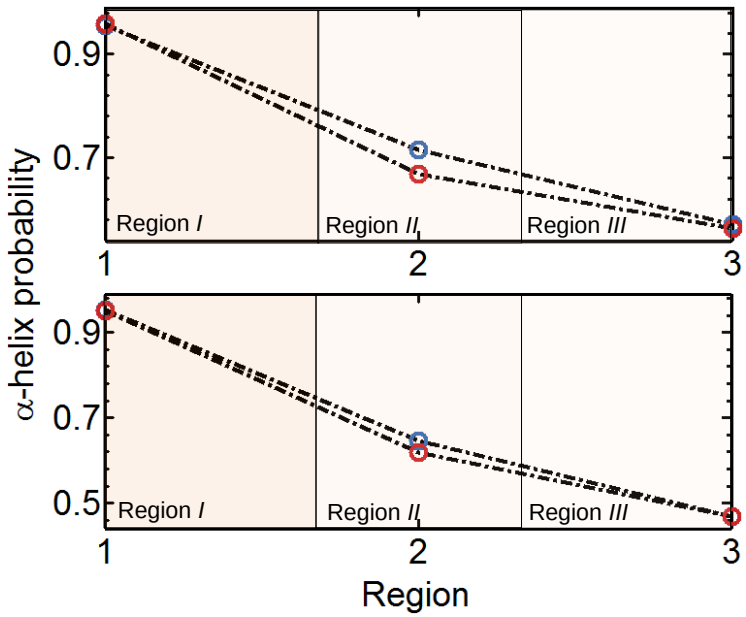

Figure 4.A.7: The α-helical propensity of residue L2 in regions I, II and III of the free energy surfaces of Figure 5 at the (a) cold unfolding temperature (T_{cu}), (b) melting temperature (T_m). Blue denotes 1 bar; red: 5 kbar.

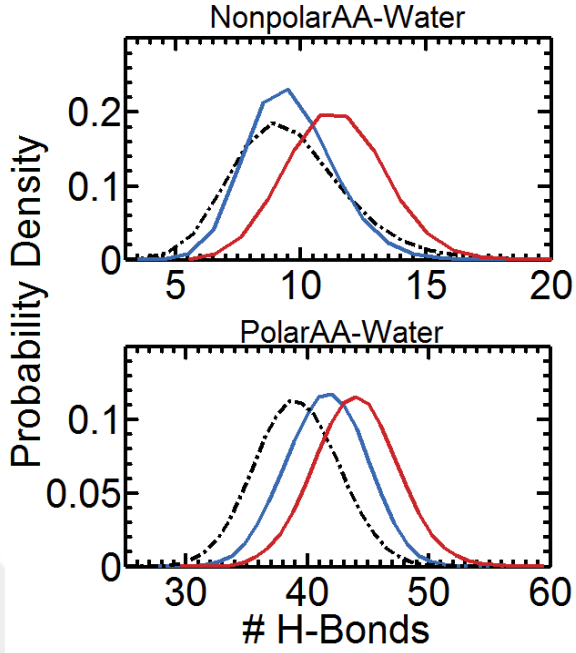

Figure 4.A.8: Probability distribution of the number of H-bonds formed between water and (a) nonpolar amino acids (NonpolarAA), (b) polar amino acids (PolarAA) in Trp-cage, at $T_{fmax,1bar}$ (black), $T_{cu,1bar}$ (blue), $T_{cu,5kbar}$ (red).

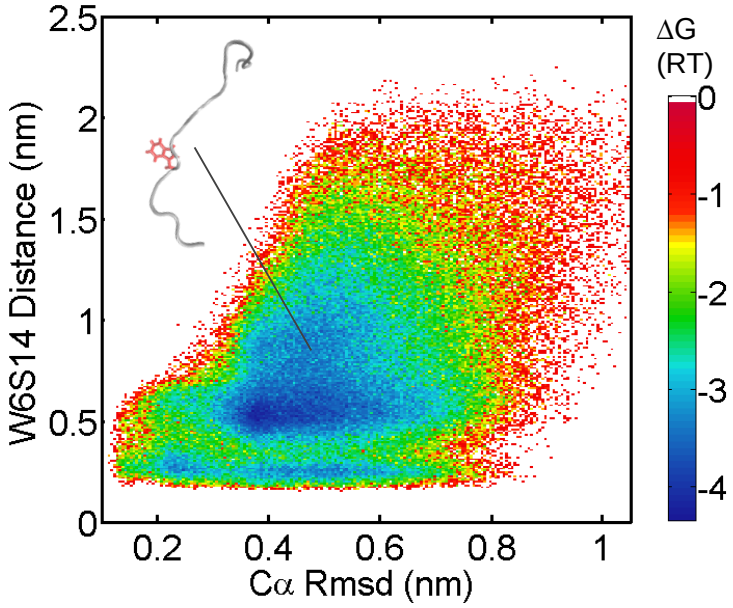

Figure 4.A.9: The free-energy surface associated with the order parameters Cα rmsd and W6S14 distance at 1 bar, 417.5K. The protein structure is a representative configuration for the given region.

Chapter 5

Pattern of Property Extrema in Supercooled and Stretched Water Models and a New Correlation for Predicting the Stability Limit of the Liquid State

This chapter is adapted from our work submitted to The Journal of Chemical Physics (B. Uralcan, Folarin Latinwo, P. G. Debenedetti, M. Anisimov, (preprint available 2018)).

5.1 Introduction

Despite being ubiquitous and essential for life, liquid water is still incompletely understood, especially in its supercooled and stretched metastable states[258, 259, 260, 261, 78, 262, 263, 264, 265, 266, 267, 268, 269, 270, 271, 83, 272, 77, 273]. A strik-

ing anomaly is the existence of a locus of density extrema, which continues into supercooled and deeply stretched (negative pressures) states[80, 101, 274, 81]. The observed extrema loci of response functions, such as isothermal compressibility (κ_T) and isobaric heat capacity (C_P), are strongly correlated with the shape of the density extrema locus [80, 101].

One possible explanation for water's anomalous behavior is the existence of a metastable first-order phase transition involving two distinct liquid phases that terminates at a liquid-liquid critical point (LLCP)[77, 78]. This liquid-liquid transition is considered to be a special case of fluid polyamorphism[81], a phenomenon that has been either found or hypothesized in a broad range of materials including metallic hydrogen[275, 276, 277], silicon[278, 94, 95], silica[96, 97], carbon[279], cerium[280] and phosporous[281]. Although experimental evidence consistent with polyamorphism exists for supercooled water[282, 262], a definitive proof is still lacking. Computer simulations, on the other hand, have shown that some molecular models of water exhibit liquid-liquid separation at deeply supercooled conditions[283, 284, 285, 286, 287, 288, 289, 290, 291, 80, 292, 293]. In tetrahedral systems, regardless of the existence or non-existence of the liquid-liquid separation (e.g., mW[87, 88, 89], mTIP4P[88], ST2[90], TIP4P/2005[91], TIP5P[92], silicon[93, 94, 95], silica[96, 97], germanium[98]), there is an underlying characteristic pattern of extrema lines for thermodynamic properties. The most well-known is the line of density extrema, whose existence suggests a competition between low-density and high-density structures in the same liquid.

The existence of the liquid-vapor and liquid-liquid transitions in a single-component fluid implies the possibility of a correlation between the pattern of extrema lines associated with the liquid-liquid transition and the stability limit of the liquid with respect to the vapor. A schematic phase diagram of a single-component fluid exhibiting both liquid-vapor and liquid-liquid phase transitions [81] is shown

in Figure 5.1. The possibility for such a fluid to crystallize is not shown in the phase diagram, however, if crystallization preempts polyamorphism, the liquid-liquid phase transition would simply be metastable with respect to crystallization. We also note that, in this particular example, the lower branch of the density extrema line, like the low-temperature part of the liquid-vapor spinodal, is located at negative pressures (stretched liquid state). The question thus arises as to whether there is any correlation between the extrema pattern and the stability limit of the liquid with respect to the vapor.

In this work, we analyze the pattern of extrema lines observed in three commonly used molecular water models (ST2, TIP4P/2005, and TIP5P) that exhibit a metastable liquid-liquid transition. We use earlier published data for ST2 (long-range electrostatic interactions are treated with the reaction field method[100]) and TIP4P/2005[289, 294], and present new simulation data for TIP5P (see Appendix 5.A). Rescaling the pressure and temperature coordinates for all these models results in a significant degree of universality in the pattern of extrema lines of the density, isothermal compressibility, and isobaric heat capacity. We also uncover a correlation between the location of the liquid-liquid critical points, the rescaled locus of thermodynamic property extrema, and the stability limit of liquid state with respect to the vapor. We discuss how this trend could be utilized for the prediction of the stability limit of the liquid state in real supercooled and stretched water, at conditions where experimental data are currently unavailable. We demonstrate a similar correlation for two generic fluid models that also exhibit a liquid-liquid critical point, namely, the "two-state" van der Waals model and the "two-state" lattice-gas model[81]. We also discuss the possibility of applying the rescaling procedure to other tetrahedral systems.

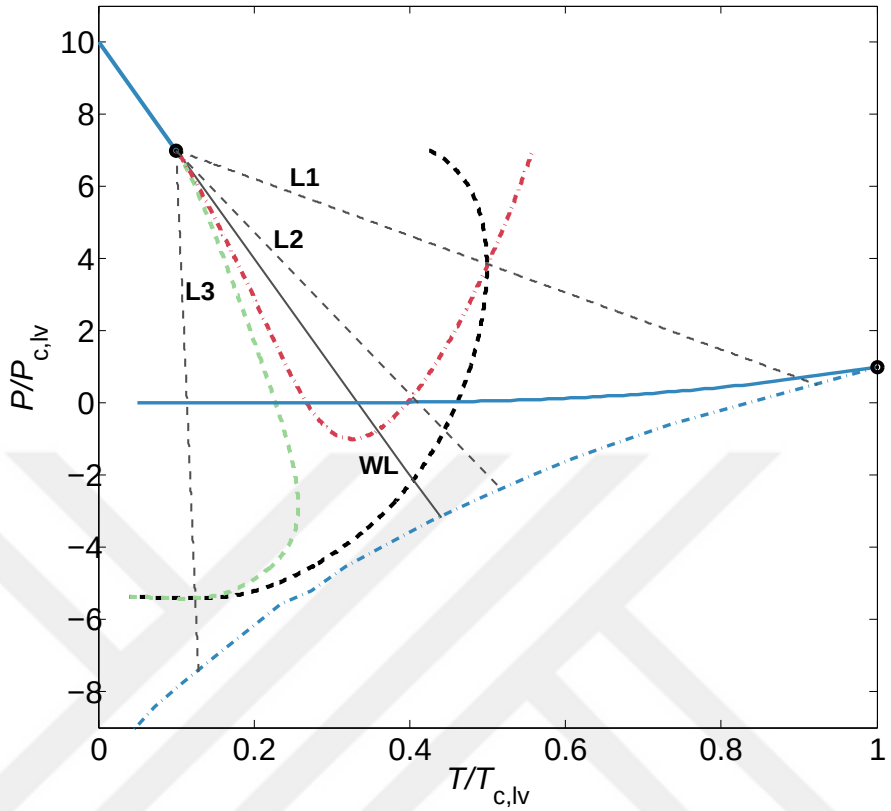

Figure 5.1: Generic phase diagram for a polyamorphic fluid (calculations for the two-state van der Waals model described by Anisimov et al.[81]). $P_{\mathrm{c,lv}}$ and $T_{\mathrm{c,lv}}$ are the pressure and temperature of the liquid-vapor critical point (LVCP). The blue curves are vapor-liquid and liquid-liquid first-order transitions ending at the LVCP and the LLCP (liquid-liquid critical point), respectively. The thin black line is the Widom line (WL), defined in the text. The blue dot-dashed curve is the liquid branch of the liquid-vapor spinodal (LVS). The black, red, and green dashed curves are loci of density, isothermal compressibility and isobaric heat capacity extrema, respectively. The three thin black dashed lines (L1, L2 and L3) are selected paths connecting the LLCP and the LVS (see Section 5.2.2).

5.2 Results and discussion

5.2.1 Searching for Universality in the Pattern of the Property Extrema

For the analysis of property extrema in molecular water models in the supercooled and stretched regions, we use molecular dynamics simulations of the ST2[100, 283, 295]

and TIP4P/2005 water models[289, 294], and report new data for the TIP5P model. The information on the property extrema in the ST2 and TIP4P/2005 models as well as for the previously unpublished TIP5P model is presented in the Appendix 5.A. In addition to the molecular water models, we also consider preliminary results for a two-structure equation of state (TSEOS) fit to experimental data for real metastable and stretched water [84].

Figure 5.2 depicts the extrema of density, isothermal compressibility (computed along isobars), and isobaric heat capacity (computed along isotherms) for three molecular water models that exhibit a liquid-liquid phase transition terminating at a critical point, namely ST2[100, 283, 295], TIP4P/2005[289, 294] and TIP5P (Appendix 5.A), and for real water obtained from the TSEOS fit to existing experimental data[84]. The stability limit of the liquid with respect to the vapor gives the lower limit of the phase diagram of liquid water. This limit is *thermodynamically* defined as a locus of divergent isothermal compressibility (blue dot-dashed curve in Figure 5.1), but is not directly attainable from experiment. The *kinetic* stability limit, on the other hand, can be directly observed in simulations, defined as the locus of spontaneous vapor cavity formation in the liquid [296] (thin solid lines in Figure 5.2). Thus, for the molecular water models, we show the kinetic stability limit of the liquid with respect to the vapor (thin solid lines in Figure 5.2), which will be used to predict the stability limit for real water in Section 5.2.2.

For the systems that we consider, the loci of density, isothermal compressibility and isobaric heat capacity extrema, and the liquid-vapor spinodal exhibit a strikingly similar pattern[88, 89, 99, 100, 101]. The location of the critical points and the thermodynamic property extrema are clearly system-dependent, but the various extrema loci exhibit many common features imposed by thermodynamics[99, 101]. In

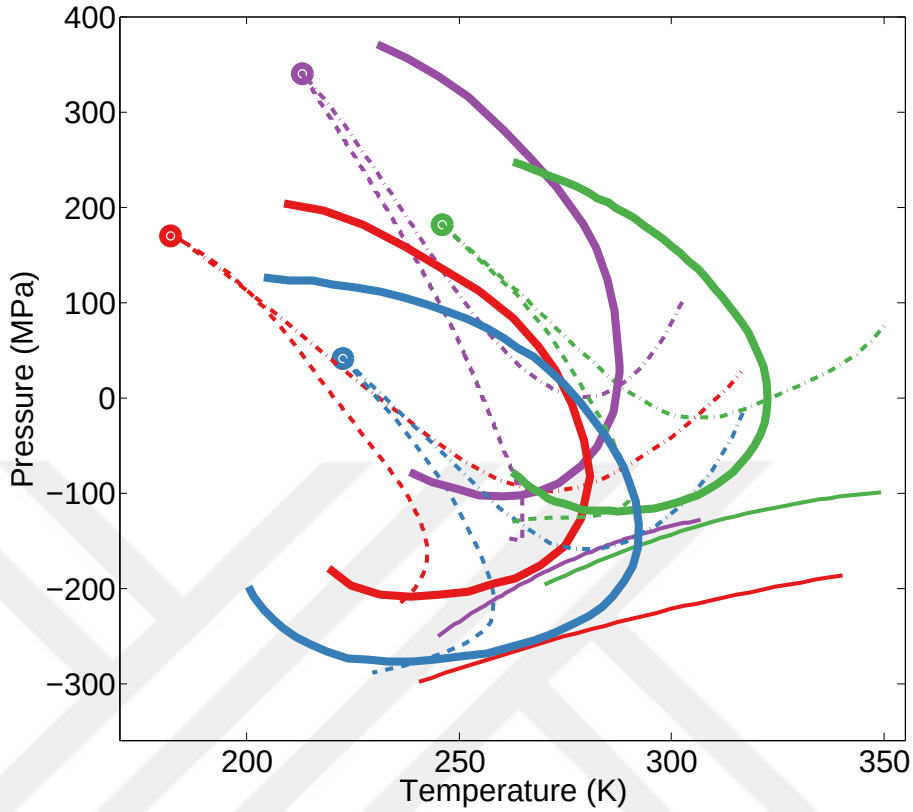

Figure 5.2: Extrema lines of various thermodynamic properties for different systems (green for ST2 [285], red for TIP4P/2005 [289, 294], purple for TIP5P (Appendix 5.A), and blue for real water, predicted by a fit to available experimental data [84]). The thick solid, dashed, and dot/dashed curves represent the loci of density, isobaric heat capacity (computed along isotherms) and isothermal compressibility (computed along isobars) extrema, respectively. The circles indicate the liquid-liquid critical points (LLCP). The thin solid lines are the cavitation lines which are observed in simulations for the water models.

particular, the loci of response function maxima merge asymptotically at the LLCP. The density shows maxima at positive pressures (temperature of maximum density, TMD). The TMD first shifts to higher temperatures as pressure is lowered, however, upon further decrease in pressure, it eventually retraces after reaching a maximum temperature ("nose") and terminates when it meets the locus of minimum densities (TmD). As required by thermodynamic constraints for the case of a monotonically increasing liquid-vapor spinodal[100, 101], the locus of isothermal compressibility

extrema intersects the TMD line's "nose". Also, the point at which the locus of density maxima joins the locus of density minima is a point along the locus of extrema of C_P, measured along isotherms[99, 100, 101].

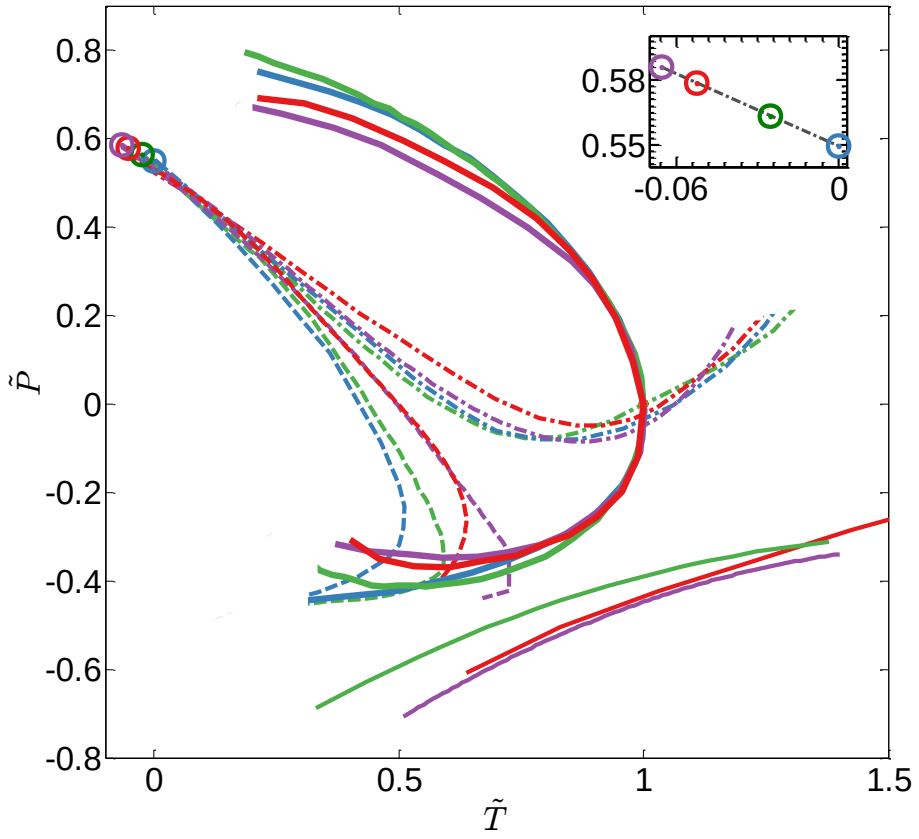

Figure 5.3: Extrema lines of various thermodynamic properties in the rescaled coordinates (green for ST2 [285], red for TIP4P/2005 [289, 294], purple for TIP5P (Appendix 5.A) and blue for real water predicted by a two-structure equation of state [84]). The thin solid lines are the cavitation lines which are observed in simulations for the water models. In the rescaled coordinates, the LLCPs lie along a straight line (see inset).

A corresponding-states-like[297, 298] rescaling of the patterns of property extrema with an eye towards a unified description could make the observed phenomena more informative and predictive. A preliminary attempt to collapse the extrema lines for two models, TIP4P/2005 and ST2, was made by Biddle [299]. In this work, we suggest

a different, though conceptually similar procedure for rescaling the temperature and pressure coordinates for the systems in Figure 5.2. Specifically, the rescaling analysis in this work is guided by the generic two-state formulation of polyamorphic fluids in Anisimov et al.[81], where the Gibbs energy difference between distinct but interconvertible states is affected by three parameters, namely, the change in energy, entropy, and volume. In the linear approximation, the Gibbs energy difference between the two interconvertible states, B and A, reads[81]

$$G_{\mathrm{BA}}(P,T) = \lambda + \alpha P + \beta T \tag{5.1}$$

where the coefficients λ, α and β represent the changes (in the linear approximation) of energy, volume and entropy, respectively. The phase transition line and the Widom line are defined as $\lambda + \alpha P + \beta T = 0$ with a constant slope $dP/dT = dS_{\mathrm{BA}}/dV_{\mathrm{BA}} = -\beta/\alpha$. This is why the rescaling requires at least three transformation steps: independently rescaling the temperature, the pressure, and accounting for a coupling between P and T along the Widom line or along any other characteristic line emanating from the LLCP.

The temperature and pressure coordinates are rescaled to account for the correlation between the liquid-liquid critical points and the density extrema loci, such that,

$$T' = \frac{T - T_{\mathrm{c}}}{T_{\mathrm{max}} - T_{\mathrm{c}}}, \tag{5.2}$$

and

$$P' = \frac{P - P(T_{\mathrm{max}})}{P_{\mathrm{c}} - P_{\mathrm{min}}}, \tag{5.3}$$

where T_{c} and P_{c} are the coordinates of the LLCP, T_{max} is the maximum temperature on the TMD line, and P_{min} is the minimum pressure on the TMD line. This rescaling fixes the coordinates of the "nose" of the TMD at (1, 0) in the scaled temperature/pressure plane, in analogy to the usual practice of fixing the scaled coordi-

nates of the critical point in corresponding states representations of the coexistence region[297]. Equations 5.2-3 also fix the vertical distance between the critical point and the point of minimum pressure along the TMD (P_{min}) to be equal to 1 in reduced pressure units. As depicted in Figure 5.A.8, this rescaling already provides an appreciable collapse for the systems considered in this work (compare with Figure 5.2). The final transformation (rotation of the coordinates) was made by rotating the extrema loci to superimpose the line connecting the LLCP and the "nose" of the TMD line (L1 in Figure 5.1), thus setting dP/dT constant along this line and accounting for the different $dS_{\mathrm{BA}}/dV_{\mathrm{BA}}$ scales. Specifically, we kept the extrema lines for the TSEOS fit for real water as in Figure 5.A.8, and rotated the molecular water models about the TMD "nose", so as to attain a common slope of the line joining the LLCP and the TMD nose. The resulting rotated coordinates are given by

$$\begin{bmatrix} \tilde{T} \\ \tilde{P} \\ 1 \end{bmatrix} = \begin{bmatrix} \cos\theta & -\sin\theta & 1-\cos\theta \\ \sin\theta & \cos\theta & -\sin\theta \\ 0 & 0 & 1 \end{bmatrix} \begin{bmatrix} T' \\ P' \\ 1 \end{bmatrix} \tag{5.4}$$

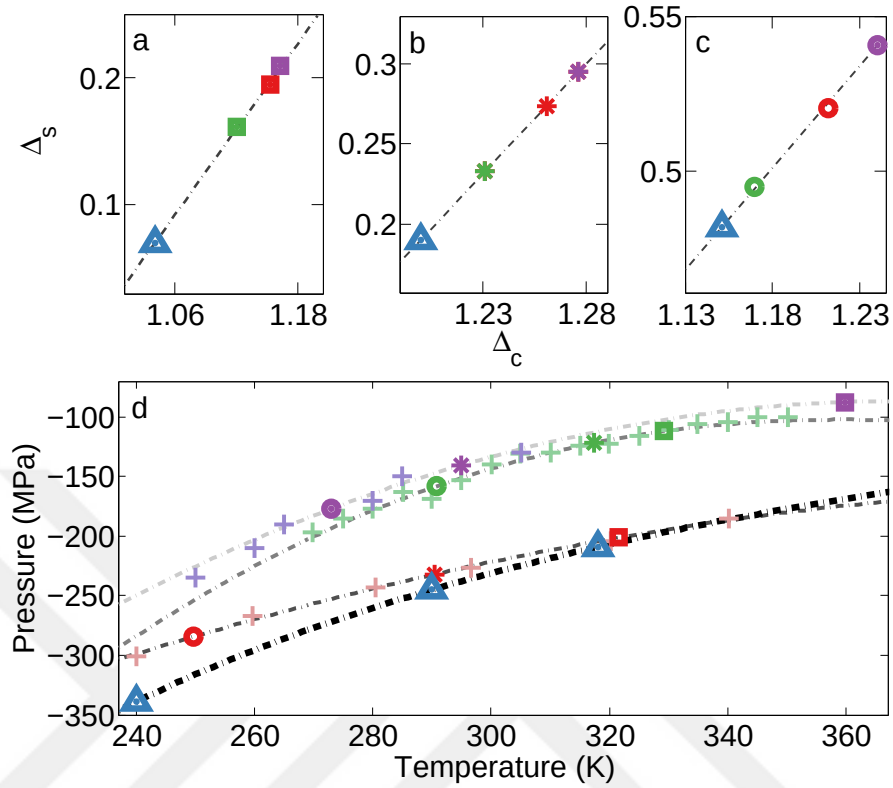

Figure 5.4: The correlation between the location of the liquid-liquid critical points, the loci of density extrema and liquid stability lines in rescaled coordinates. Δ_c is the distance between LLCP and the following points along the TMD locus: intersection with the (a) locus of C_P extrema, path L3; (b) point on the TMD locus having a pressure that is equal to the average of $P_{\min}$ and $P(T_{\max})$, path L2 in Figure 5.1; (c) locus of κ_T extrema, path L1, in Figure 5.1. Δ_s is the distance between the stability limits of water with respect to its vapor and the above-defined corresponding points on the density extrema locus. (d) Consistency of computed liquid-vapor stability limits with the linear correlations between Δ_c and Δ_s. The crosses (green for ST2 [285], red for TIP4P/2005 [289, 294], purple for TIP5P (Appendix 5.A) are kinetic stability limits obtained from simulations. Circles, stars, and squares are obtained from the correlations for molecular water models and the dot-dashed lines are quadratic fits to the symbols. Blue triangles are the prediction of the kinetic stability limit for real water from the correlations and the dot-dashed line is a quadratic fit to the data.

where θ is the rotation angle around the "nose" of the TMD line (see Table 5.2 for θ values, and Equation 5.7 to read back (T', P') from $(\tilde{T}, \tilde{P})$). By construction, this step aligns the LLCPs along a straight line (see the insert in Figure 5.3). The results in final rescaled coordinates are shown in Figure 5.3. We note that the rotation angles for the systems in Figure 5.3 are small since all of them are models representing the same substance (i. e., water). It is for this reason that rescaling without rotation leads to a satisfactory level of collapse in this analysis (Figure 5.A.8), but rotation would be essential for generalization to models with considerably different L1 slopes (see Figure 5.A.11).

The results in final rescaled coordinates are shown in Figure 5.3. It is remarkable that this rescaling achieves the degree of collapse one sees in going from Figure 5.2 to Figure 5.3. The shape of the TMD locus is not constrained by our scaling, and it can be seen from Figure 5.3 that (i) this locus departs from universality below $\tilde{T} \approx 0.75$, both at high and low pressures; (ii) there is better collapse for the loci of compressibility extrema than for the corresponding heat capacity extrema; (iii) the kinetic limits of stability with respect to the vapor exhibit interesting collapse, even if unconstrained by the choice of scaling. These observations apply to the molecular water models considered here (ST2, TIP4P/2005, TIP5P), and there is no implication as to their generality. In sum, the choice of proper scaling accomplishes a very satisfactory degree of collapse, including in features that are not constrained by scaling (e.g., kinetic limits of stability), suggesting "universality" in the overall picture. Although some global features imposed by thermodynamics are model-independent (e.g., the intersections between the TMD and the heat capacity and compressibility extrema, the former defining $P_{\min}$ and the latter defining $T_{\max}$, as can be seen in Figure 5.2), achieving satisfactory collapse through scaling is a non-trivial result.

5.2.2 Correlation with the Stability of the Liquid State

The rescaling of pressure and temperature coordinates brings to light an intriguing correlation between the liquid-liquid critical point, the TMD line and the kinetic liquid-vapor stability limit for molecular water models. Figure 5.4(a-c) shows the distance, in scaled coordinates, from the LLCP to the TMD line (Δ_c) displayed against the distance from the TMD line to the kinetic limit of liquid-vapor stability (Δ_s), along the three paths shown in Figure 1 by black dashed lines. We observe that these distances are linearly correlated (Figure 5.4(a-c)) for the molecular water models (green for ST2 [285], red for TIP4P/2005 [289, 294], purple for TIP5P (Appendix 5.A), which means that for a system that exhibits a satisfactory level of collapse with the molecular water models, we can predict Δ_s given Δ_c (or vice versa). Thus, we attempt to locate the kinetic stability limit for real water using the linear correlation for molecular water models (Figure 5.4(a-c)) to predict the distance from the TMD line to the kinetic limit of liquid-vapor stability (Δ_s), given the distance from the LLCP to the TMD line (Δ_c) (blue triangles in Figure 5.4(a-c)), computed using the LLCP and thermodynamic property extrema given by the TSEOS fit[84]. The predicted kinetic liquid-vapor stability limit for real water is shown in Figure 5.4(d) (blue triangles and the quadratic dot-dashed fit) as well as the kinetic stability limits for molecular water models. We note that the location of the hypothesized LLCP in real water (shown in Figure 5.2 at T_c≈223 K, P_c≈42 MPa) is highly uncertain (e.g., (T_c≈232 K, P_c≈27 MPa)[300], (T_c≈223 K, P_c≈50 MPa)[301], (T_c≈227 K, P_c≈13 MPa)[83], (T_c≈168 K, P_c≈195 MPa)[290], (T_c≈210 K, P_c≈100 MPa)[302]), which strongly affects the prediction of the stability line (see Figure 5.A.9 for how the prediction for the stability line shifts with the location of the LLCP).

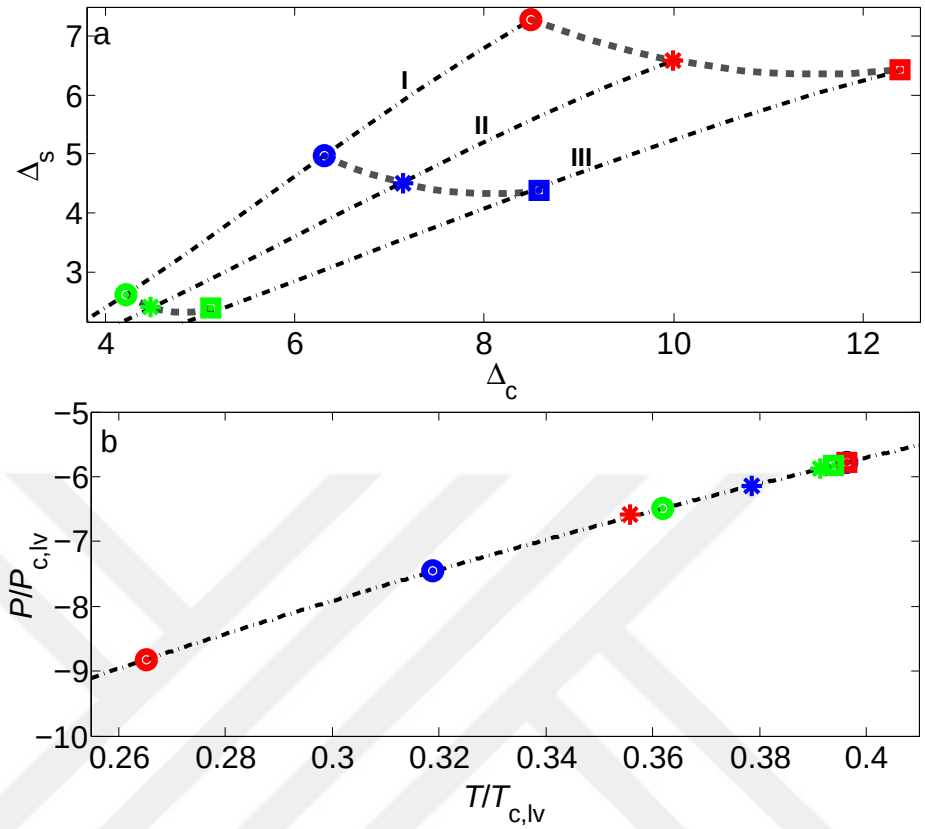

Figure 5.5: The correlation between the location of the liquid-liquid critical point, the locus of density extrema, and the liquid-vapor spinodal (LVS) upon tuning the location of the liquid-liquid critical point for the two-state van der Waals model. (a) Δ_c is the distance between LLCP and the points at which the density extrema intersect the locus of κ_T extrema (I); the Widom line (II), and the locus of C_P extrema (III). Δ_s is the distance between the liquid stability lines and points on density extrema loci along the same paths. (b) The reconstruction of the LVS from the correlations between Δ_c and Δ_s (green, blue, and red symbols correspond to three different values of the LLCP). $T_{c,lv}$ and $P_{c,lv}$ are the pressure and temperature of the LVCP. The dot-dashed line is the liquid-vapor spinodal for the two-state van der Waals model.

We also investigated two simple fluid models that incorporate a two-state formalism based on the underlying picture of interconversion between alternative molecular states, namely the van der Waals and lattice gas "two state" models[81]. For these models, we kept the Widom line and the absolute liquid-vapor stability limit constant by fixing the liquid-vapor critical point, and the energy, volume and entropy parameters in Equation 5.1 and constructed several scenarios by tuning the location of the LLCP along the Widom line by changing the nonideality in the Gibbs energy of mixing (see Anisimov et al.[81] for details). Upon applying the same rescaling procedure, we observed similar correlations between the distance from the LLCPs to the TMD line (Δ_c) and the distance from the TMD line to the liquid-vapor spinodal (Δ_s) along several paths, as shown in Figure 5.5a for the van der Waals model. Particularly, for the simple fluid models, we define the three paths along L1, L3 and the Widom line (Figure 5.1). The liquid vapor spinodal for these fluid models is constructed accurately from the observed correlations as shown in Figure 5.5b. Similar results are given for the lattice-gas model in Figure 5.A.10.

We note that the correlation between the distance to the LLCP and the liquid-vapor stability limit, and, more broadly, the interdependence of liquid-vapor and liquid-liquid transitions can be explained by considering the two-state formulation of polyamorphic fluids where the fluid is defined by the existence of two interconvertible states, A and B[81, 80]. In particular, in the thermodynamics of two competing structures[81, 80], the shape of the liquid-liquid transition line, the slope of the Widom line, and the location of LLCP are defined by the difference in the Gibbs energies between states B and A, while the shape of TMD is also affected by state A. Specifically, since the vapor-liquid spinodal is a part of state A[80], the anomalous behavior of the state A's density near the liquid-vapor spinodal modifies the shape of TMD significantly.

A correlation between the location of the LLCP, the shape of the TMD line, and the liquid-vapor kinetic spinodal is a generic feature of polyamorphic fluids. The quantitative correlation along three selected paths, suggested and verified in this work, is very simple (linear or very close to linear). It works well for three molecular water models. However, our procedure, in the specific form in which it has been formulated, cannot be generally applicable to polymorphic fluids with very different LLPT topologies. For example, when the slope of line L1 is less negative than that of the line joining the liquid-liquid and liquid-vapor critical points, L1 will not cross the liquid-vapor kinetic spinodal, and thus this particular path cannot be used in the prediction of LVS. Furthermore, the procedure fails in two special cases: the "bird's beak" in the LL coexistence[81] and a vertical LLPT. In both cases the TMD line collapses or disappears. Extension of our method so as to encompass these cases may necessitate modifications in the form of the correlation and/or the scaling procedure, and would require additional studies.

5.3 Conclusions

We present a rescaling of the thermodynamic property extrema of previously published and new simulation results for three commonly-used molecular models of water (ST2[100, 283, 295], TIP4P/2005[289, 294], and TIP5P). The rescaling procedure results in a satisfactory near-collapse of the property extrema loci for these three models. The rescaled coordinates bring forth an intriguing correlation between the location of the liquid-liquid critical point, the line of density extrema, and the *kinetic* stability limit of the liquid state with respect to the vapor (cavitation line). This underlines the interdependence of liquid-liquid and liquid-vapor transitions in polyamorphic fluids. Our results are supported by similar correlations between the location of the liquid-liquid critical point, the line of density extrema, and the *thermodynamic* stability limit

of the liquid state with respect to the vapor for two generic models that also exhibit a second critical point, namely, the van der Waals and lattice-gas "two-state" models. We utilize this general trend to predict the *kinetic* stability limit of the liquid state in simultaneously supercooled and stretched water, for which experimental data are currently unavailable. We note that the general trend identified in this work could also be potentially utilized for the prediction of the thermodynamic stability limit for real water by constructing the liquid-vapor spinodals for the water models and establishing similar correlations between them. The thermodynamic stability limit is not directly attainable, but there are theoretical studies that investigate the relationship between the kinetic and thermodynamic stability limits of water[80, 265, 303], and future work could utilize these studies to investigate the liquid-vapor spinodal for real water. It will be also interesting to explore the extent to which the present scaling procedure can be successfully applied to other tetrahedral systems exhibiting water-like behavior, such as tetrahedral patchy colloids[304], silicon[278, 94, 95] and silica[96]. We plan to pursue such studies in the future.

5.A Appendix

5.A.1 Simulation Details

The molecular dynamics simulations for TIP5P were performed using 216 water molecules in a cubic box in the isothermal-isobaric ensemble. The simulations were performed using the GROMACS 4.6.7 package[196, 206] with a time step of 2 fs. Periodic boundary conditions were applied. The temperature was maintained using a Nosé-Hoover thermostat[201, 202] (0.2 ps time constant). A Parrinello-Rahman barostat[203, 204] (2 ps time constant) was used to maintain the pressure. A 0.85 nm cutoff was used for short-ranged (electrostatic and Lennard-Jones) interactions. The smooth-particle mesh Ewald (PME) technique with a 0.12 nm grid spacing was

used to treat long-ranged electrostatic interactions. The standard long-range dispersion corrections were made for the pressure and energy. Bond constraints were maintained using the Linear Constraint Solver (LINCS) algorithm[196].

The simulations were performed in the pressure range 310 MPa down to -210 MPa and the temperature range 220 K to 330 K. The resulting EOS data for ρ(P, T) is shown in Figure 5.A.1.

Figure 5.A.2 shows the isothermal compressibility (κ_T) as a function of temperature for several isobars (for clarity only a few of the simulated isobars are depicted), computed from

$$\kappa_T = \frac{\langle (\Delta V)^2 \rangle}{k_B T \langle V \rangle} \tag{5.5}$$

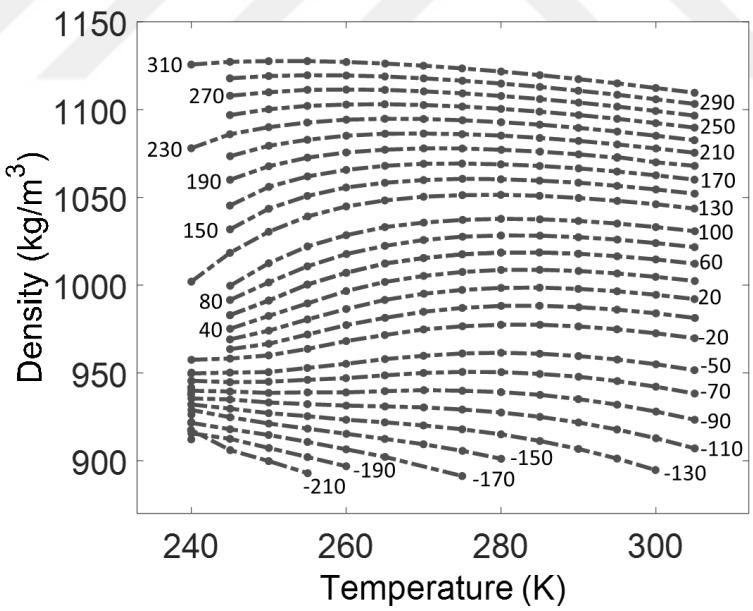

Figure 5.A.1: Density along isobars for the TIP5P water model. Circles are simulation data and lines are guides to the eye. Pressures for each isobar are shown in the figure, in MPa.

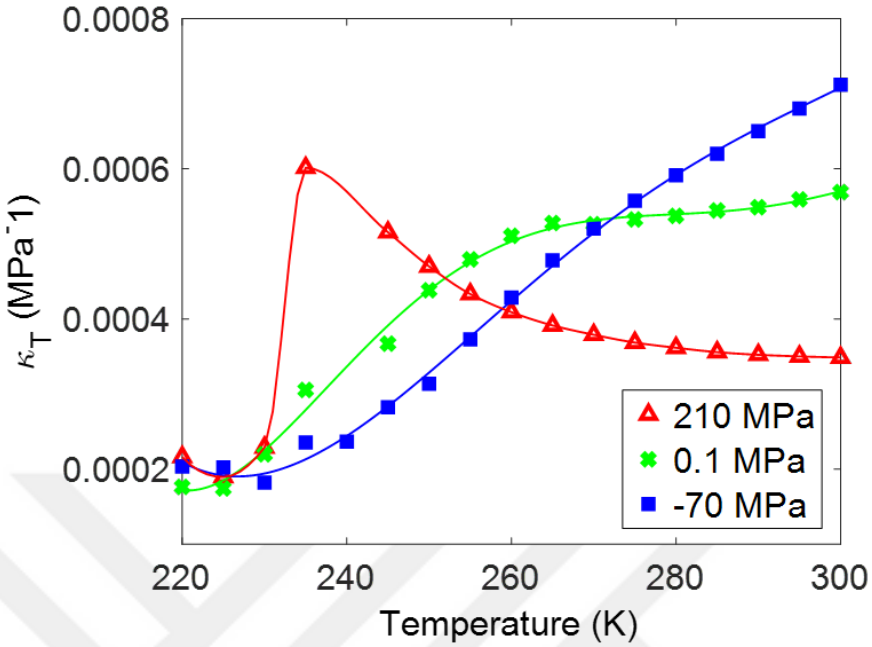

Figure 5.A.2: Isothermal compressibility (κ_T) as a function of temperature along isobars for the TIP5P water model computed from NPT simulations. Lines are guides to the eye.

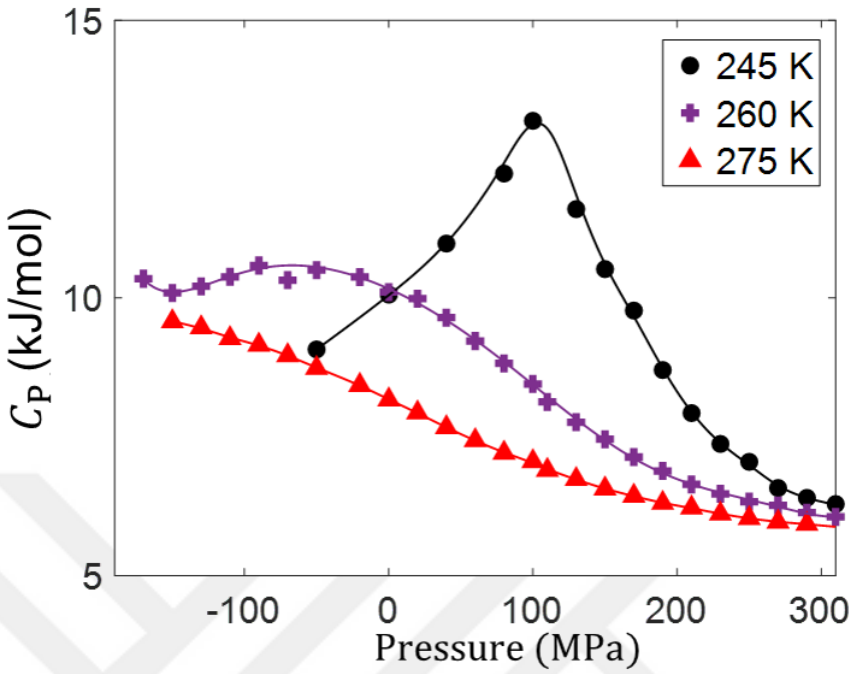

Figure 5.A.3: Isobaric heat capacity (C_P) as a function of pressure along isotherms for the TIP5P water model computed from NPT simulations. Lines are guides to the eye.

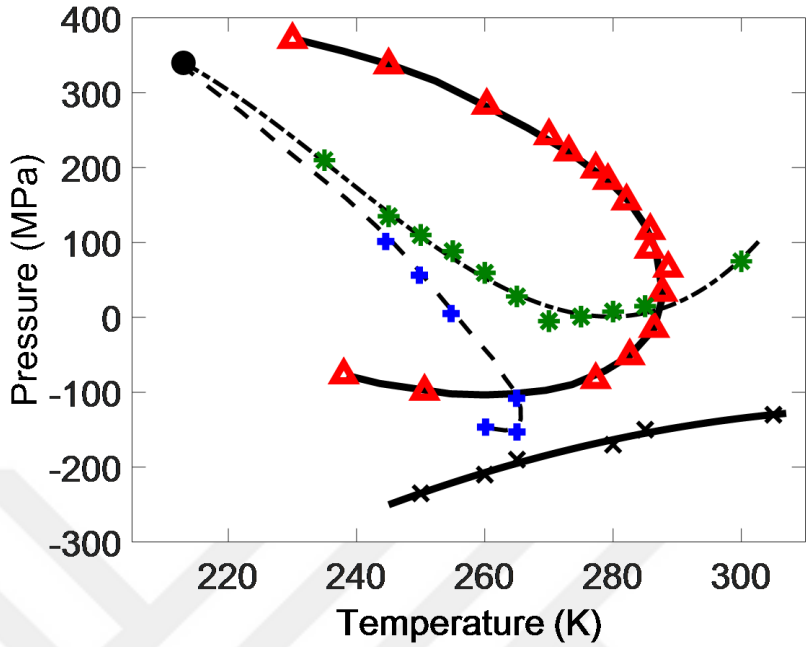

Figure 5.A.4: Symbols represent simulation data on the extrema of various thermodynamic properties for the TIP5P water model. Red triangles and solid line represent the density extrema, blue plus signs and dashed line represent the isobaric heat capacity extrema, and green stars and solid/dashed line represent the isothermal compressibility extrema. The black circle is the liquid-liquid critical point. The black crosses are where the cavitation was observed in simulations. All lines are guides to the eye.

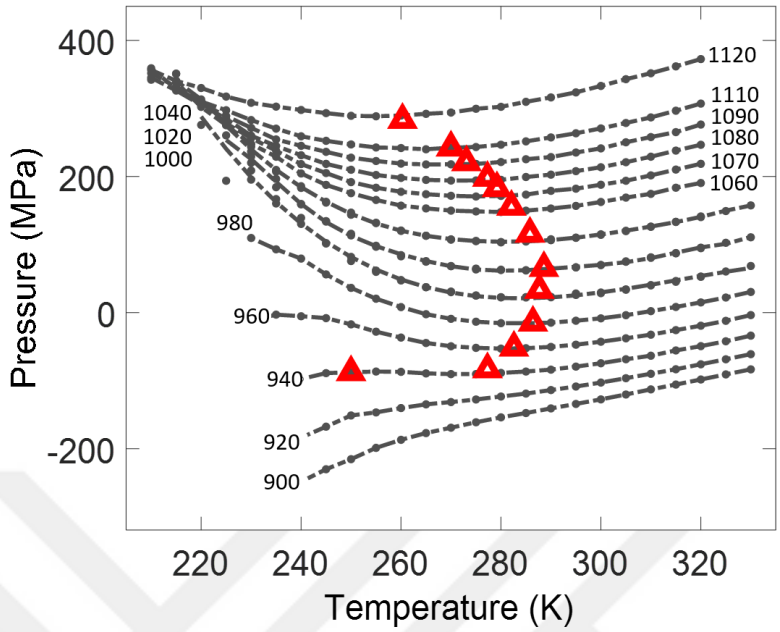

Figure 5.A.5: Pressure as a function of temperature along isochores for the TIP5P water model. Circles are simulation data and lines are guides to the eye. Densities for each isochore are shown in the figure. The red triangles represent the density maxima (pressure minima along isochores) and minima (pressure maxima along isochores).

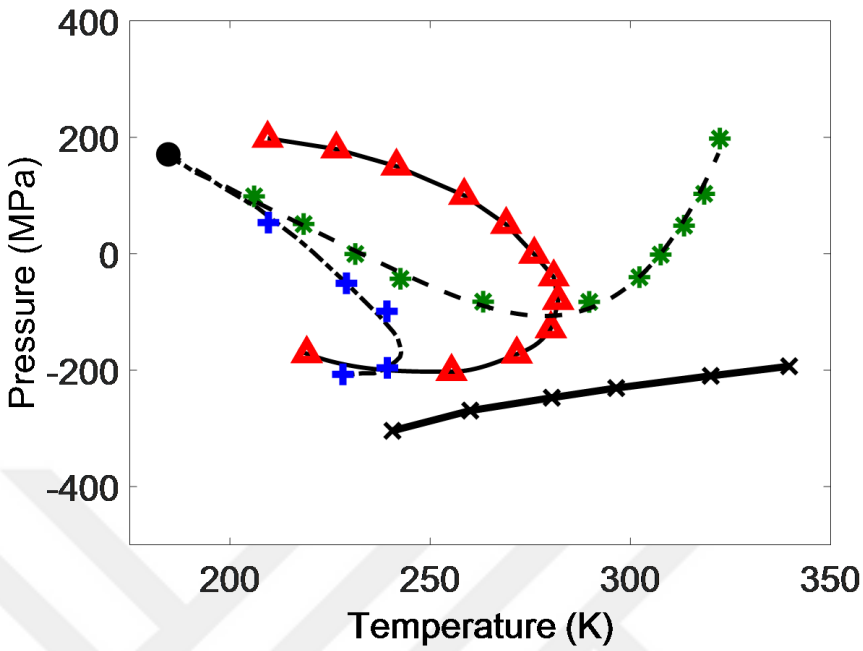

Figure 5.A.6: Symbols represent simulation data on the extrema of various thermodynamic properties for TIP4P/2005 water. Red triangles and solid line represent the density extrema, blue plus signs and dashed line represent the isobaric heat capacity extrema computed along isotherms, and green stars and solid/dashed line represent the isothermal compressibility extrema computed along isobars. The black circle is the liquid-liquid critical point. The black crosses are where the cavitation was observed in simulations. All lines are guides to the eye.

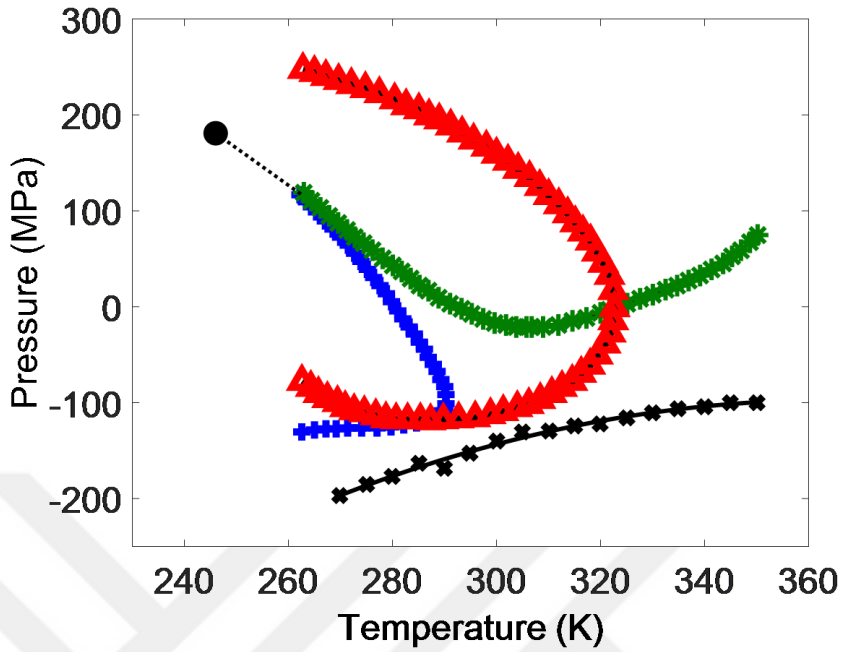

Figure 5.A.7: Symbols represent simulation data on the extrema of various thermodynamic properties for ST2 water model, with reaction field treatment of long-ranged electrostatic interactions[100]. Red triangles represent the density extrema, blue plus signs represent the isobaric heat capacity extrema, and green stars represent the isothermal compressibility extrema. The black circle is the liquid-liquid critical point. The black crosses are where the cavitation was observed in simulations. All lines are guides to the eye.

For pressures higher than about -20 MPa the isobars show the presence of a maximum and a minimum. At pressures slightly lower than -20 MPa, the maximum and minimum merge into an inflection point. At large negative pressures, κ_T increases monotonically with temperature. We fit cubic splines to κ_T data in Figure 5.A.2, and compute the locus of κ_T extrema (Figure 5.A.4) analytically.

The simulation results for C_P along isotherms are presented in Figure 5.A.3, computed from

$$C_P = \frac{\langle (\Delta H)^2 \rangle}{k_B T^2} \tag{5.6}$$

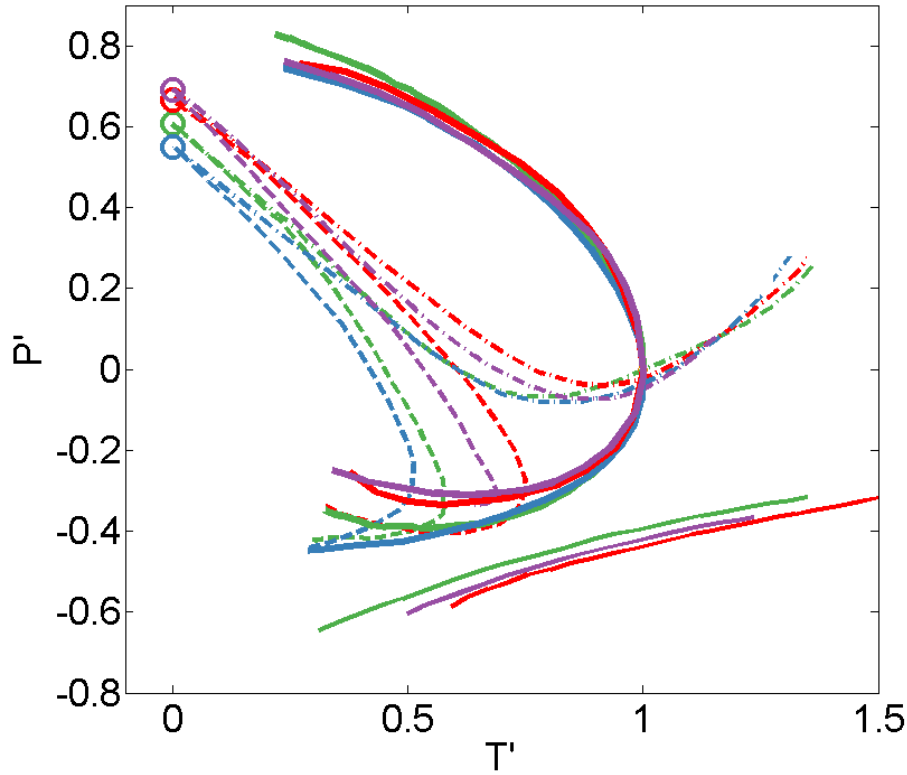

Figure 5.A.8: Extrema lines of various thermodynamic properties in the rescaled coordinates T' and P' (Green for ST2, red for TIP4P/2005, purple for TIP5P, and blue for real water, fitted and extrapolated with a two-structure equation of state13). The thick solid, dashed, and dot/dashed curves represent the loci of density, isobaric heat capacity (measured along isotherms) and isothermal compressibility (measured along isobars) extrema, respectively. The circles indicate the liquid-liquid critical points (LLCP). The thin solid lines are the cavitation lines which are observed in simulations for the water models.

The isotherms show both a maximum and a minimum below 265 K. At higher temperatures, the maximum and minimum merge into an inflection point and C_P becomes a monotonic function of pressure. We fit cubic splines to C_P data in Figure 5.A.3, and compute the locus of C_P extrema (Figure 5.A.4) analytically. The locus of C_P extrema along isotherms is shown in Figure 5.A.4. The kinetic limit of stability (cavitation) of stretched TIP5P is shown by crosses in Figure 5.A.4.

We also performed, for TIP5P, simulations in the canonical ensemble with 216 water molecules. We computed the properties of liquid water at 440 state points at densities ranging from 880 to 1160 kg/m3 and temperatures ranging from 210 K to

330 K in steps of 5 K. We observe that the isochores cross at ≈213 K, ≈340 MPa supporting the possibility of an LLCP in this model of water. The resulting EOS data for $P(\rho, T)$ is shown in Figure 5.A.5, together with the locus of density extrema computed as pressure extrema along the isochores.

Simulation data on the extrema of thermodynamic properties for ST2[100] and TIP4P/2005[289, 294] water models are given in Figure 5.A.6 and Figure 5.A.7.

Table 5.1: Critical temperature (T_c) and pressure (P_c) for the systems under consideration.

	T_c **(K)**	P_c **(MPa)**
water TSEOS[84]	222.7	41.7
ST2[100]	246.0	181.0
TIP4P/2005[289, 294]	184.6	170.7
TIP5P	213.0	340.0

5.A.2 Rescaling Analysis

Table 5.2: Rotation angle (θ) (see in Equation 5.7)

	θ **(radian)**
water TSEOS[84]	0
ST2[100]	0.0428
TIP4P/2005[289, 294]	0.0840
TIP5P	0.102

The conversion between (T', P') and ($\tilde{T}$,$\tilde{P}$) is given by

$$\begin{bmatrix} T' \\ P' \\ 1 \end{bmatrix} = \begin{bmatrix} \cos\theta & \sin\theta & 2\sin^2(\theta/2) \\ sin\theta & \cos\theta & \sin\theta \\ 0 & 0 & 1 \end{bmatrix} \begin{bmatrix} \tilde{T} \\ \tilde{P} \\ 1 \end{bmatrix} \tag{5.7}$$

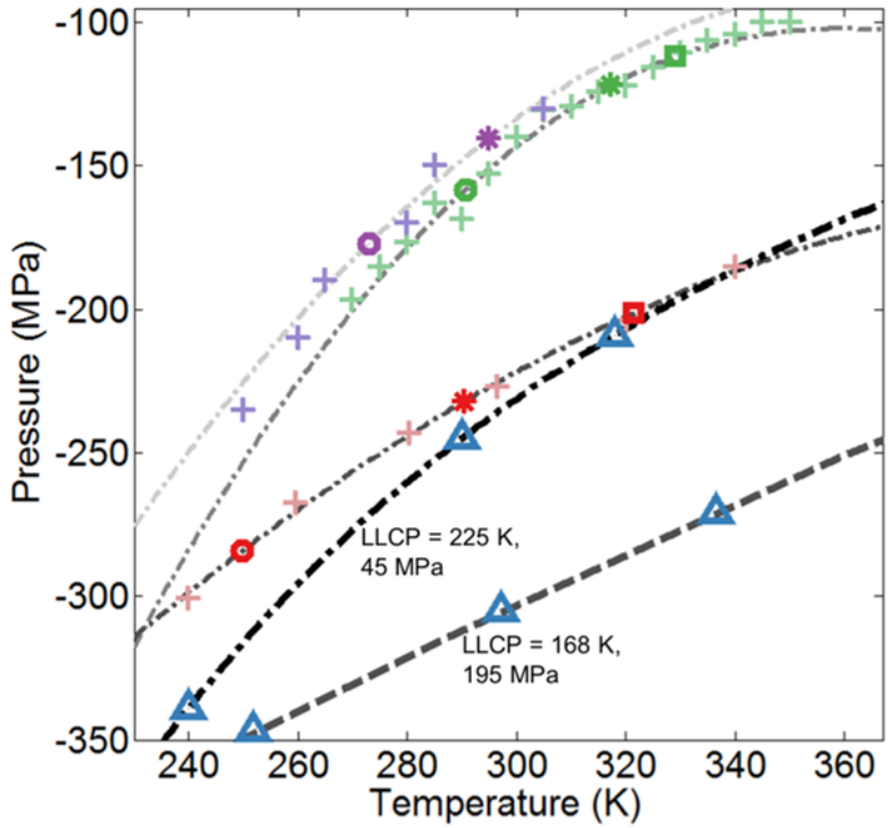

Figure 5.A.9: Consistency of computed liquid-vapor stability limits with the linear correlations between Δc and Δs. The crosses (green for ST2, red for TIP4P/2005, purple for TIP5P are kinetic stability limits (cavitation) obtained from simulations. Circles, stars, and squares are obtained from the correlations for molecular water models (green for ST2, red for TIP4P/2005, purple for TIP5P) and the dot-dashed lines are quadratic fits to the symbols. Blue triangles are the prediction of the kinetic stability limit for real water from the above correlations (for two different LLCPs) and the dashed and dot-dashed curves are quadratic fits to the data at the two different LLCPs.

5.A.3 Lattice-gas model

For the lattice gas model[81], the absolute liquid-vapor stability limit is kept fixed by setting the temperature and density of the liquid-vapor critical point, and the energy, entropy and volume differences between interconvertible structures (see Equation 5.1). For the "two-state" lattice-gas model, we tuned the location of the LLCP and applied the rescaling procedure similar to the two-state van der Waals model as

described in the main text. As shown in Figure S10, we observed similar linear correlations between the distance, in rescaled coordinates, from the LLCPs to the TMD line (Δc) and the distance from the TMD line to the liquid-vapor spinodal (Δs) along three different paths emanating from the LLCP, as in the "two-state" van der Waals model.

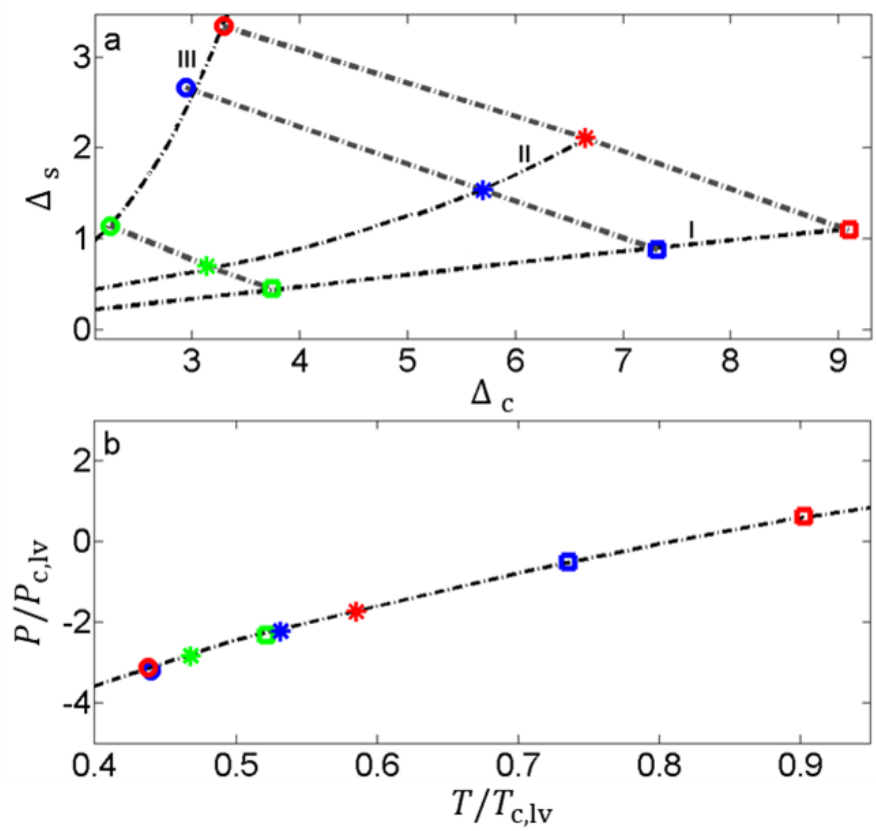

Figure 5.A.10: The correlation between the location of the liquid-liquid critical point, patterns of extrema and liquid vapor spinodal upon tuning the location of the liquid-liquid critical point for the lattice-gas model. (a) The parameter Δc is the distance between LLCP and the points at which the density extrema intersect the locus of κ_T extrema (I); the Widom line (II), and the locus of C_P extrema (III). The parameter Δs is the distance between the liquid stability lines and points on density extrema loci along the same paths. (b) The reconstruction of the LVS from the linear correlations between Δc and Δs (green, blue, and red symbols correspond to three different values of the LLCP). The dot-dashed line is the calculated spinodal. $T_{c,lv}$ and $P_{c,lv}$ are the critical temperature and pressure, respectively, for the vapor-liquid critical point.

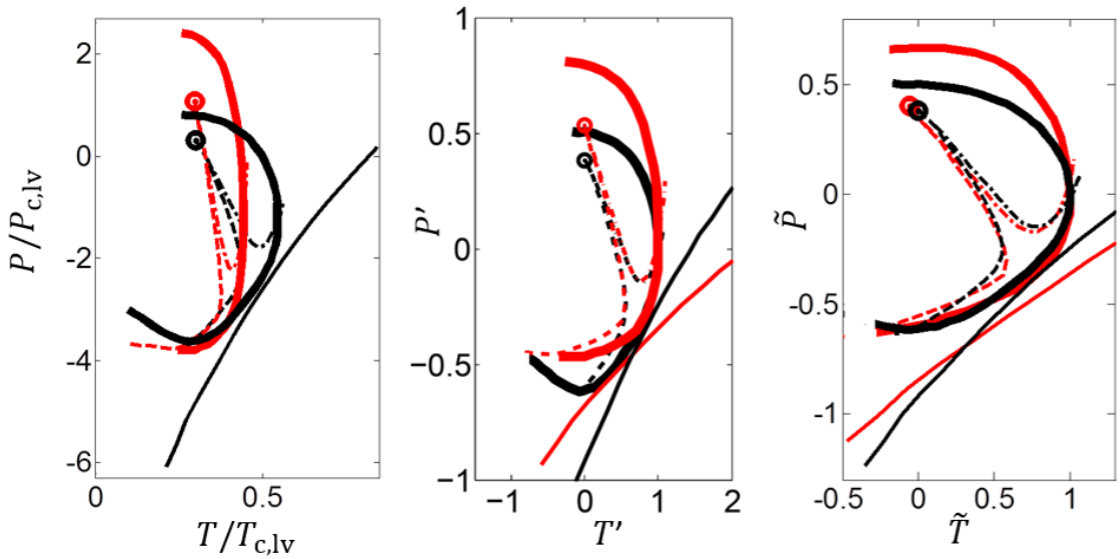

Figure 5.A.11: Extrema lines of various thermodynamic properties in the rescaled coordinates for two different values of LLCP and WL, (a) before rescaling, (b) in rescaled coordinates T', P', and (c) in rescaled coordinates $\tilde{T}$,$\tilde{P}$. The thick solid, dashed, and dot/dashed curves represent the loci of density, isobaric heat capacity (measured along isotherms) and isothermal compressibility (measured along isobars) extrema, respectively. The circles indicate the liquid-liquid critical points. The thin solid lines are the liquid vapor spinodal.

Chapter 6

Concluding Remarks

This dissertation is concerned with the use of computer simulations, when appropriate combined with model experiments, to understand the effect of environmental perturbations on soft matter systems. With tools and techniques derived from statistical mechanics providing the basis, we studied capacitive response at electrode/electrolyte interfaces, thermodynamics and mechanisms of protein folding, and anomalous properties of liquid water under environmental perturbations. Investigations of how these systems respond to changes in their environment not only have relevance to the development of biophysical and energy processes, but also aid in gaining a fundamental level understanding of life over broad ranges of thermodynamic conditions.

6.1 Concentration Fluctuations and Capacitive Response in Dense Ionic Solutions

In this work, we investigated the effects of electrolyte composition on the capacitive response of an electrical double layer capacitor using experimental and computational tools[113, 305]. First, we measured the double-layer capacitance of a glassy carbon-electrolyte interface using mixtures of RTILs and organic solvents over a wide

concentration range. We showed that the double-layer capacitance of the electrode-RTIL interface near the potential of zero charge reaches a maximum upon dilution of the RTIL with three different solvents (i.e., acetonitrile, dichloroethane, propoylene carbonate), and provided evidence that this capacitance maximum is not correlated with the mixture's bulk conductivity.

Next, we simulated a coarse-grained model to provide an explanation for the anomalous capacitance maximum[113]. In particular, we used a charge-frustrated Ising model that has been previously used in the context of ionic liquids[109], reproducing experimentally observed phase diagrams. Consistent with experiment, for certain parameter regimes of the lattice-model, we found a nonmonotonic dependence of the capacitance near the potential of zero charge to the ion concentration. While we recovered the square root dependence of capacitance ($C \propto \sqrt{\rho}$) predicted by GCS theory in the dilute regime, in the concentrated regime, we found that capacitance is proportional to solvent concentration ($C \propto \sqrt{1-\rho}$). Within this model, the capacitance maximum resulted from a competition between charge fluctuations at the electrode due to the uncorrelated motion of single free ions that dominates in the dilute regime, and those similarly free motions of dilute solvent molecules that can dominate in the highly concentrated limit. While the solvent molecules themselves did not carry a charge, due to the incompressibility of the lattice, solvent motion in a concentrated electrolyte occurred with the correlated swapping of a charge in the direction opposing its motion.

Finally, to gain insight into the molecular mechanisms that lead to capacitance enhancement upon dilution of RTILs in the concentrated regime, we peformed molecular dynamics simulations in the constant potential ensemble[305]. Specifically, we employed molecular simulations of butlymethylimidazolium hexafluorophosphate ([BMIM][PF6])-acetonitrile mixtures bounded by electrodes modeled as three parallel ideal conductor honeycomb lattices of carbon atoms on both sides. The constant po-

tential ensemble simulations allowed the electrode charges to fluctuate as a response the thermal fluctuations in the electrolyte, while maintaining a constant potential difference between electrodes. This method offered a physically transparent way to decompose the effects of microscopic correlations on electrochemical response. We showed that the concentration dependence of the capacitance results from the interplay between two different limiting behaviors. In the dilute ion concentration regime, charge fluctuations are simply proportional to the number of ions near the electrode, because their mean distances are larger than the electrostatic screening length, and so those fluctuations are uncorrelated. In the pure ionic liquid, ions are densely packed, and charge fluctuations are determined by steric constraints and interionic Coulomb correlations. The addition of a small amount of solvent mediates these constraints, increasing the magnitude of charge fluctuations. At a specific concentration, these effects are balanced, leading to an intermediate concentration where the capacitance is maximized. The analysis presented in ths work offered a general way to understand the molecular contributions to the electrochemical response of complex electrolyte solutions and enabled means to examine how molecular features such as polarity, size, and shape affect electrochemical responses, opening new directions for the optimization and rational design of energy storage devices.

6.2 A Computational Study of the Ionic Liquid-Induced Destabilization of the Miniprotein Trp-Cage

In this work, we investigated the effect of RTILs on the stability of an α-helical miniprotein with a hydrophobic core, Trp-cage, using fully atomistic replica exchange molecular dynamics (REMD) simulations[51], and compared our results to circular

dichroism measurements. We chose Trp-cage as our model protein due to its fast folding dynamics and the fact that it possesses secondary structural features similar to those found in larger globular proteins[188, 189, 190, 191, 192, 193]. We used guanidinium acetate ([Gdm][Act]) and 1-ethyl-3-methylimidazolium acetate ([EMIM][Act]) for solvating Trp-cage.

In particular, based on the two-state model of Anson[207], we constructed the stability diagram of Trp-cage in the concentration (C) - temperature (T) plane, which exhibits an elliptical shape in the 290-420 K range, suggesting destabilization of Trp-cage at constant ion concentration with increasing temperature, or at constant temperature with increasing ion concentration. Trp-cage's stability as a function of RTIL content obtained from our simulations was in qualitative agreement with fraction folded Trp-cage profiles from circular dichroism measurements.

In particular, we found that Trp-cage swells due to enhanced interaction with ionic liquid species, depicted by the increase in its solvent accessible surface area, widening of its hydrophobic core and the disruption of its salt bridge with RTIL content. This results in increasing the exposure of both hydrophilic and hydrophobic residues to the solvent, and consecutively, less favorable intramolecular protein-protein interactions as revealed by a decrease in the number of intramolecular H-bonds formed within Trp-cage's structure. Nevertheless, the partially unfolded states observed in these aqueous RTIL mixtures were populated by configurations that conserve secondary structure elements, as opposed to completely unraveled states. In fact, we found that the mechanism of RTIL-induced denaturation resembles cold unfolding, where the equilibrium of conformational states shifts toward partially unfolded configurations.

Despite this deformation, however, at temperatures above 420 K, we observed an apparent stabilization of Trp-cage with increasing ion content. This apparent stabilization was due to an overall increase in Trp-cage's α-helical content upon increasing

RTIL content at high temperatures. The fraction of α-helical content measured by circular dichroism also qualitatively captured this trend.

Denaturation of Trp-cage, which is entropically driven at ambient and higher temperatures in pure water despite unfavorable enthalpy, became less endothermic in the presence of RTILs. We showed that this is due to the formation of additional solvent-protein H-bonds in RTILs, that offset the positive ΔH from the disruption of intramolecular protein H-bonds. In this regard, the effect of RTIL content on the unfolding thermodynamics of Trp-cage is similar to the effect of decreasing the temperature in pure water in the subzero temperature range[40].

6.3 Computational Investigation of the Effect of Pressure on Protein Stability

In this work, we investigated the stability of the Trp-cage miniprotein in pure water at temperatures between 210 and 420 K in the pressure range 1 bar to 5 kbar using replica exchange molecular dynamics (REMD) simulations. We constructed the stability diagram in the (P,T) plane from fully atomistic simulation data using using the two-state protein folding model of Anson[207] where we defined the folded state with the order parameters root-mean-squared deviation of Trp-cage's Cα atoms from the fully folded reference NMR structure[46] (Cα rmsd) and the minimum distance between the tryptophan (W6) and serine (S14) residues (W6S14 distance). We showed that contours along which the folded fraction is constant display elliptical shapes that are characteristic of proteins which undergo both low- and high-temperature unfolding. Increasing the pressure destabilized Trp-cage's folded state at temperatures above ≈250K. On the other hand, below ≈250K, Trp-cage's stability exhibited a nonmonotonic dependence on pressure.

We observed that Trp-cage's stability decreases with increasing pressure at room temperature and above, but it exhibits a nonmonotonic dependence on pressure at lower temperatures. Cold unfolding and thermal denaturation mechanisms differed significantly at ambient pressure, but they became progressively similar at high pressures, consistent with a dome-shaped stability region. At ambient pressure, we observed that the dominant structure upon melting has both its tertiary and secondary structures disrupted, but Trp-cage cold-unfolds into a relatively compact state with elements of its secondary structure significantly conserved. On the other hand, at high pressures, the cold- and thermally-unfolded states share similar degrees of secondary and tertiary structural perturbation.

Trp-cage's unfolding exhibits a remarkable enthalpy-entropy compensation, whereby the change in enthalpy upon unfolding is largely compensated by a corresponding change in entropy, resulting in small ΔG. We depict that thermal denaturation of Trp-cage at temperatures above T_{fmax} is entropically driven with positive entropy and enthalpy changes upon unfolding. The $T \geq T_{\mathrm{fmax}}$ behavior of ΔH and ΔS is largely insensitive to pressure. On the other hand, below T_{fmax}, cold unfolding and thermal denaturation mechanisms differ significantly. While cold unfolding at 1 bar is enthalpically driven ($\Delta H < 0$) and entropically disfavored ($\Delta S < 0$), at elevated pressures ΔH and $T\Delta S$ become very small and largely balance each other.

To gain further structural insight into the differences between cold-unfolding and heat denaturation mechanisms at ambient and high pressures, we investigated the exposure of Trp-cage to the solvent upon unfolding. To this end, we computed the change in the solvent accessible surface area upon unfolding ($\Delta SASA_{\mathrm{u}}$) and the change in the number of water molecules around residue W6 upon unfolding (ΔNw_{u}). Independent of pressure, heat denaturation results in an increase in $\Delta SASA_{\mathrm{u}}$ and ΔNw_{u}. At sufficiently high temperatures, Trp-cage completely unravels, losing both

the secondary and tertiary structure elements of the native fold and exposing all residues to water. In contrast, cold unfolding exhibits quite different trends at ambient and high pressures. At elevated pressures, $\Delta SASA_{\mathrm{u}}$ and ΔNw_{u} increase with decreasing temperature. Thus, at elevated pressures, reducing or increasing temperature away from T_{fmax} lead to increases in $\Delta SASA_{\mathrm{u}}$ and ΔNw_{u}, similar to thermal unfolding. In contrast, at ambient pressure, we observed that cooling (heating) away from T_{fmax} led to progressively smaller (larger) increases in $\Delta SASA_{\mathrm{u}}$ and ΔNw_{u}.

Employing fully atomistic simulations to construct stability diagrams for larger globular proteins remains prohibitively expensive. We anticipate that progress in hardware, software and sampling algorithms will facilitate the study of cold denaturation of larger globular proteins and enable the calculation of full (P,T) stability diagrams, which cannot be easily obtained by experiment.

6.4 Pattern of Property Extrema in Supercooled and Stretched Water Models and a New Correlation for Predicting the Stability Limit of the Liquid State

In this work, we analyzed previously published and new simulation results for three commonly used molecular water models (ST2, TIP4P/2005, and TIP5P) that support the existence of the metastable liquid-liquid transition. For the systems that we considered, the loci of density, isothermal compressibility and isobaric heat capacity extrema, and the liquid-vapor spinodal exhibit strikingly similar patterns[88, 89, 99, 100, 101]. The location of the critical points and the thermodynamic property extrema are clearly system-dependent, but the various extrema loci exhibit many common features imposed by thermodynamics[99, 101]. In order to make these similar patterns

more informative and predictive, we employed a corresponding-states-like[297, 298] rescaling of the patterns of property extrema with an eye towards a unified description.

A preliminary attempt to collapse the extrema lines for two models, TIP4P/2005 and ST2, was made by Biddle [299]. In this work, we suggested a different, though conceptually similar procedure for rescaling the temperature and pressure coordinates. Specifically, the rescaling analysis in this work was guided by the generic two-state formulation of polyamorphic fluids in Anisimov et al.[81].

The rescaling procedure resulted in a satisfactory near-collapse of the property extrema loci for these three models. The rescaled coordinates brought forth an intriguing correlation between the location of the liquid-liquid critical point, the line of density extrema, and the *kinetic* stability limit of the liquid state with respect to the vapor (cavitation line). This underlines the interdependence of liquid-liquid and liquid-vapor transitions in polyamorphic fluids. Our results were supported by similar correlations between the location of the liquid-liquid critical point, the line of density extrema, and the *thermodynamic* stability limit of the liquid state with respect to the vapor for two generic models that also exhibit a second critical point, namely, the van der Waals and lattice-gas "two-state" models. We utilized this general trend to predict the *kinetic* stability limit of the liquid state in simultaneously supercooled and stretched water, for which experimental data are currently unavailable.

We note that the general trend identified in this work could also be potentially utilized for the prediction of the thermodynamic stability limit for real water by constructing the liquid-vapor spinodals for the water models and establishing similar correlations between them. The thermodynamic stability limit is not directly attainable, but there are theoretical studies that investigate the relationship between the kinetic and thermodynamic stability limits of water[80, 265, 303], and future work could utilize these studies to investigate the liquid-vapor spinodal for real water. It will be also interesting to explore the extent to which the present scaling procedure

can be successfully applied to other tetrahedral systems exhibiting water-like behavior, such as tetrahedral patchy colloids[304], silicon[278, 94, 95] and silica[96]. We plan to pursue such calculations in the future.

Bibliography

[1] David C. Grahame. The electrical double layer and the theory of electrocapillarity. *Chemical Reviews*, 41(3):441–501, 1947.

[2] Maxim V Fedorov and Alexei A Kornyshev. Ionic liquids at electrified interfaces. *Chemical reviews*, 114(5):2978–3036, 2014.

[3] H. Helmholtz. Ueber einige gesetze der vertheilung elektrischer strme in krperlichen leitern, mit anwendung auf die thierisch-elektrischen versuche (schluss.). *Annalen der Physik und Chemie*, 165(7):353–377, 1853.

[4] M. Gouy. Sur la constitution de la charge électrique à la surface dun électrolyte. *Journal de Physique Théorique et Appliquée*, 9(1):457–468, 1910.

[5] David Leonard Chapman. A contribution to the theory of electrocapillarity. *The London, Edinburgh, and Dublin Philosophical Magazine and Journal of Science*, 25(148):475–481, 1913.

[6] O. Stern. Zur theorie der elektrolytischen doppelschicht. *Z.Elektrochem.Angew.Phys.Chem.*, 30:508–516, 1924.

[7] J. J. Bikerman. Electrokinetic equations for gels and the absolute magnitude of electrokinetic potentials. *The Journal of Physical Chemistry*, 46(7):724–730, 1942.

[8] M. Dutta and S.N. Bagchi. On the distribution of ions in solutions of strong electrolytes. *Ind. J. Phys.*, 24, 1950.

[9] V Freise. Zur theorie der diffusen doppelschicht. *Zeitschrift fr Elektrochemie*, 56:822–827, 1952.

[10] E. Wicke and M. Eigen. Zum konzentrationsverlauf der aktivittskoeffizienten starker elektrolyte. *Die Naturwissenschaften*, 39(23):545–546, 1952.

[11] Itamar Borukhov, David Andelman, and Henri Orland. Steric effects in electrolytes: A modified poisson-boltzmann equation. *Physical Review Letters*, 79(3):435–438, 1997.

[12] Veronika Kralj-Iglic and Veronika Kralj-Iglic. Stability of membranous nanostructures: a possible key mechanism in cancer progression. *International Journal of Nanomedicine*, page 3579, 2012.

[13] Dmytro Antypov, Marcia C. Barbosa, and Christian Holm. Incorporation of excluded-volume correlations into poisson-boltzmann theory. *Physical Review E*, 71(6), 2005.

[14] Patrice Simon and Yury Gogotsi. Materials for electrochemical capacitors. *Nature Materials*, 7(11):845–854, 2008.

[15] M Revere and M P Tosi. Structure and dynamics of molten salts. *Reports on Progress in Physics*, 49(9):1001–1081, 1986.

[16] K.R. Painter, P. Ballone, M.P. Tosi, P.J. Grout, and N.H. March. Capacitance of metal-molten-salt interfaces. *Surface Science*, 133(1):89–100, 1983.

[17] Alexei A Kornyshev. Double-layer in ionic liquids: Paradigm change? *The Journal of Physical Chemistry B*, 111(20):5545–5557, 2007.

[18] Maxim V. Fedorov and Alexei A. Kornyshev. Ionic liquid near a charged wall: Structure and capacitance of electrical double layer. *The Journal of Physical Chemistry B*, 112(38):11868–11872, 2008.

[19] Maxim V. Fedorov and Alexei A. Kornyshev. Erratum: Ionic liquid near a charged wall: Structure and capacitance of electrical double layer. *The Journal of Physical Chemistry B*, 113(13):4500–4500, 2009.

[20] Maxim V. Fedorov and Alexei A. Kornyshev. Towards understanding the structure and capacitance of electrical double layer in ionic liquids. *Electrochimica Acta*, 53(23):6835 – 6840, 2008.

[21] Martin Z Bazant, Brian D Storey, and Alexei A Kornyshev. Double layer in ionic liquids: Overscreening versus crowding. *Physical Review Letters*, 106(4):046102, 2011.

[22] Martin Z. Bazant, Brian D. Storey, and Alexei A. Kornyshev. Erratum: Double layer in ionic liquids: Overscreening versus crowding [phys. rev. lett. 106, 046102 (2011)]. *Phys. Rev. Lett.*, 109(14):149903, 2012.

[23] Michel Armand, Frank Endres, Douglas R. MacFarlane, Hiroyuki Ohno, and Bruno Scrosati. Ionic-liquid materials for the electrochemical challenges of the future. *Nature Materials*, 8(8):621–629, 2009.

[24] Patrice Simon and Yury Gogotsi. Materials for electrochemical capacitors. *Nature materials*, 7(11):845–854, 2008.

[25] X. Yang, C. Cheng, Y. Wang, L. Qiu, and D. Li. Liquid-mediated dense integration of graphene materials for compact capacitive energy storage. *Science*, 341(6145):534–537, 2013.

[26] Y. Zhu, S. Murali, M. D. Stoller, K. J. Ganesh, W. Cai, P. J. Ferreira, A. Pirkle, R. M. Wallace, K. A. Cychosz, M. Thommes, D. Su, E. A. Stach, and R. S. Ruoff. Carbon-based supercapacitors produced by activation of graphene. *Science*, 332(6037):1537–1541, 2011.

[27] M. Arulepp, L. Permann, J. Leis, A. Perkson, K. Rumma, A. Jnes, and E. Lust. Influence of the solvent properties on the characteristics of a double layer capacitor. *Journal of Power Sources*, 133(2):320–328, 2004.

[28] Alan B. McEwen. Electrochemical properties of imidazolium salt electrolytes for electrochemical capacitor applications. *Journal of The Electrochemical Society*, 146(5):1687, 1999.

[29] V. Ruiz, T. Huynh, S. R. Sivakkumar, and A. G. Pandolfo. Ionic liquid–solvent mixtures as supercapacitor electrolytes for extreme temperature operation. *RSC Advances*, 2(13):5591, 2012.

[30] Michael A. Pope, Sibel Korkut, Christian Punckt, and Ilhan A. Aksay. Supercapacitor electrodes produced through evaporative consolidation of graphene oxide-water-ionic liquid gels. *Journal of The Electrochemical Society*, 160(10):A1653–A1660, 2013.

[31] Guang Feng, Jingsong Huang, Bobby G Sumpter, Vincent Meunier, and Rui Qiao. A counter-charge layer in generalized solvents framework for electrical double layers in neat and hybrid ionic liquid electrolytes. *Physical Chemistry Chemical Physics*, 13(32):14723–14734, 2011.

[32] Song Li, Guang Feng, and Peter T Cummings. Interfaces of dicationic ionic liquids and graphene: A molecular dynamics simulation study. *Journal of Physics: Condensed Matter*, 26(28):284106, 2014.

[33] Alan B. McEwen. Nonaqueous electrolytes for electrochemical capacitors: Imidazolium cations and inorganic fluorides with organic carbonates. *Journal of The Electrochemical Society*, 144(4):L84, 1997.

[34] Céline Merlet, Mathieu Salanne, Benjamin Rotenberg, and Paul A Madden. Influence of solvation on the structural and capacitive properties of electrical double layer capacitors. *Electrochimica Acta*, 101:262–271, 2013.

[35] Charles Tanford. Protein denaturation. *Adv. Protein Chem.*, 23:121–282, 1968.

[36] F. GOWLAND Hopkins. Denaturation of proteins by urea and related substances. *Nature*, 126(3175):383–384, 1930.

[37] Jing Zhang, Xiangdong Peng, Ana Jonas, and Jiri Jonas. NMR study of the cold, heat, and pressure unfolding of ribonuclease a. *Biochem.*, 34(27):8631–8641, 1995.

[38] P.L. Privalov. Stability of proteins small globular proteins. *Adv. Protein Chem.*, 33:167–241, 1979.

[39] Dietmar Paschek, Sascha Hempel, and Angel E. García. Computing the stability diagram of the trp-cage miniprotein. *Proc. Natl. Acad. Sci. U.S.A.*, 105(46):17754–17759, 2008.

[40] Sang Beom Kim, Jeremy C. Palmer, and Pablo G. Debenedetti. Computational investigation of cold denaturation in the trp-cage miniprotein. *Proc. Natl. Acad. Sci. U.S.A.*, 113(32):8991–8996, 2016.

[41] Sapna Sarupria, Tuhin Ghosh, Angel E. Garca, and Shekhar Garde. Studying pressure denaturation of a protein by molecular dynamics simulations. *Proteins: Struct., Funct., Bioinf.*, 78(7):1641–1651, 2010.

[42] Dagmar Ringe Gregory A. Petsko. *Protein Structure and Function.* New Science Press, 2004.

[43] Carl Ivar Branden. *Introduction to Protein Structure.* Garland Science, 2012.

[44] P. J. Halling. Proteins: Structures and molecular properties (2nd edition). by thomas e. creighton, w. h. freeman, new york, 1992, xiii + 512 pp, price 22.95. isbn 0-7167-7030-x. *Journal of Chemical Technology & Biotechnology*, 62(1):105–105.

[45] Ryan Day, Dietmar Paschek, and Angel E. Garcia. Microsecond simulations of the folding/unfolding thermodynamics of the trp-cage miniprotein. *Proteins: Struct., Funct., Bioinf.*, 78(8):1889–1899, 2010.

[46] Jonathan W. Neidigh, R. Matthew Fesinmeyer, and Niels H. Andersen. Designing a 20-residue protein. *Nature Structural Biology*, 9(6):425–430, 2002.

[47] Juan R. Perilla and Thomas B. Woolf. Towards the prediction of order parameters from molecular dynamics simulations in proteins. *The Journal of Chemical Physics*, 136(16):164101, 2012.

[48] Sang Beom Kim, Carmeline J. Dsilva, Ioannis G. Kevrekidis, and Pablo G. Debenedetti. Systematic characterization of protein folding pathways using diffusion maps: Application to trp-cage miniprotein. *The Journal of Chemical Physics*, 142(8):085101, 2015.

[49] Angel E. Garcia and Dietmar Paschek. Simulation of the pressure and temperature folding/unfolding equilibrium of a small RNA hairpin. *Journal of the American Chemical Society*, 130(3):815–817, 2008.

[50] Ken A. Dill, S. Banu Ozkan, M. Scott Shell, and Thomas R. Weikl. The protein folding problem. *Annual Review of Biophysics*, 37(1):289–316, 2008.

[51] Betul Uralcan, Sang Beom Kim, Chester E. Markwalter, Robert K. Prud'homme, and Pablo G. Debenedetti. A computational study of the ionic liquid-induced destabilization of the miniprotein trp-cage. *The Journal of Physical Chemistry B*, 122(21):5707–5715, 2018.

[52] Henry S. Ashbaugh, Thomas M. Truskett, and Pablo G. Debenedetti. A simple molecular thermodynamic theory of hydrophobic hydration. *The Journal of Chemical Physics*, 116(7):2907–2921, 2002.

[53] C Tanford. The hydrophobic effect and the organization of living matter. *Science*, 200(4345):1012–1018, 1978.

[54] C. B. Anfinsen. Principles that govern the folding of protein chains. *Science*, 181(4096):223–230, 1973.

[55] Steven S. Plotkin and José N. Onuchic. Understanding protein folding with energy landscape theory part i: Basic concepts. *Quarterly Reviews of Biophysics*, 35(02), 2002.

[56] Cyrus Levinthal. Are there pathways for protein folding? *Journal de Chimie Physique*, 65:44–45, 1968.

[57] Martin Karplus and David L. Weaver. Diffusion-collision model for protein folding. *Biopolymers*, 18(6):1421–1437, 1979.

[58] Martin Karplus and David L. Weaver. Protein folding dynamics: The diffusion-collision model and experimental data. *Protein Science*, 3(4):650–668, 2008.

[59] Alan R Fersht. Nucleation mechanisms in protein folding. *Current Opinion in Structural Biology*, 7(1):3–9, 1997.

[60] N Go. The consistency principle in protein structure and pathways of folding. *Advances in Biophysics*, 18:149–164, 1984.

[61] Morten Bertz, Andrea Kunfermann, and Matthias Rief. Navigating the folding energy landscape of green fluorescent protein. *Angewandte Chemie International Edition*, 47(43):8192–8195, 2008.

[62] RobertL. Baldwin. The nature of protein folding pathways: The classical versus the new view. *Journal of Biomolecular NMR*, 5(2), 1995.

[63] Christopher M. Dobson. Protein folding and misfolding. *Nature*, 426(6968):884–890, 2003.

[64] Ken A. Dill and Hue Sun Chan. From levinthal to pathways to funnels. *Nature Structural & Molecular Biology*, 4(1):10–19, 1997.

[65] Christopher M. Dobson, Andrej Šali, and Martin Karplus. Protein folding: A perspective from theory and experiment. *Angewandte Chemie International Edition*, 37(7):868–893, 1998.

[66] T. Cellmer, M. Buscaglia, E. R. Henry, J. Hofrichter, and W. A. Eaton. Making connections between ultrafast protein folding kinetics and molecular dynamics simulations. *Proceedings of the National Academy of Sciences*, 108(15):6103–6108, 2011.

[67] Robert H. Callender, R. Brian Dyer, Rudolf Gilmanshin, and William H. Woodruff. Fast events in protein folding: The time evolution of primary processes. *Annual Review of Physical Chemistry*, 49(1):173–202, 1998.

[68] A. R. Fersht and S. Sato. θ-value analysis and the nature of protein-folding transition states. *Proceedings of the National Academy of Sciences*, 101(21):7976–7981, 2004.

[69] T. R. Sosnick, R. S. Dothager, and B. A. Krantz. Differences in the folding transition state of ubiquitin indicated by θ and γ analysis. *Proceedings of the National Academy of Sciences*, 101(50):17377–17382, 2004.

[70] M KRISHNA. Hydrogen exchange methods to study protein folding. *Methods*, 34(1):51–64, 2004.

[71] Karen L. Maxwell, David Wildes, Arash Zarrine-Afsar, Miguel A. De Los Rios, Andrew G. Brown, Claire T. Friel, Linda Hedberg, Jia-Cherng Horng, Diane Bona, Erik J. Miller, Alexis Vallée-Bélisle, Ewan R.G. Main, Francesco Bemporad, Linlin Qiu, Kaare Teilum, Ngoc-Diep Vu, Aled M. Edwards, Ingo Ruczinski, Flemming M. Poulsen, Birthe B. Kragelund, Stephen W. Michnick, Fabrizio Chiti, Yawen Bai, Stephen J. Hagen, Luis Serrano, Mikael Oliveberg, Daniel P. Raleigh, Pernilla Wittung-Stafshede, Sheena E. Radford, Sophie E. Jackson, Tobin R. Sosnick, Susan Marqusee, Alan R. Davidson, and Kevin W. Plaxco. Protein folding: Defining a "standard" set of experimental conditions and a preliminary kinetic data set of two-state proteins. *Protein Science*, 14(3):602–616, 2005.

[72] C. Cecconi. Direct observation of the three-state folding of a single protein molecule. *Science*, 309(5743):2057–2060, 2005.

[73] Ron O. Dror, Robert M. Dirks, J.P. Grossman, Huafeng Xu, and David E. Shaw. Biomolecular simulation: A computational microscope for molecular biology. *Annual Review of Biophysics*, 41(1):429–452, 2012.

[74] Thomas J Lane, Diwakar Shukla, Kyle A Beauchamp, and Vijay S Pande. To milliseconds and beyond: challenges in the simulation of protein folding. *Current Opinion in Structural Biology*, 23(1):58–65, 2013.

[75] Stefano Piana, Kresten Lindorff-Larsen, and David E. Shaw. How robust are protein folding simulations with respect to force field parameterization? *Biophysical Journal*, 100(9):L47–L49, 2011.

[76] Stefano Piana, John L Klepeis, and David E Shaw. Assessing the accuracy of physical models used in protein-folding simulations: quantitative evidence from long molecular dynamics simulations. *Current Opinion in Structural Biology*, 24:98–105, 2014.

[77] Paola Gallo, Katrin Amann-Winkel, Charles Austen Angell, Mikhail Alexeevich Anisimov, Frédéric Caupin, Charusita Chakravarty, Erik Lascaris, Thomas Loerting, Athanassios Zois Panagiotopoulos, John Russo, Jonas Alexander Sellberg, Harry Eugene Stanley, Hajime Tanaka, Carlos Vega, Limei Xu, and Lars Gunnar Moody Pettersson. Water: A tale of two liquids. *Chemical Reviews*, 116(13):7463–7500, 2016.

[78] Peter H. Poole, Francesco Sciortino, Tor Grande, H. Eugene Stanley, and C. Austen Angell. Effect of hydrogen bonds on the thermodynamic behavior of liquid water. *Physical Review Letters*, 73(12):1632–1635, 1994.

[79] Pablo G. Debenedetti and H. Eugene Stanley. Supercooled and glassy water. *Physics Today*, 56(6):40–46, 2003.

[80] John W. Biddle, Rakesh S. Singh, Evan M. Sparano, Francesco Ricci, Miguel A. González, Chantal Valeriani, José L. F. Abascal, Pablo G. Debenedetti, Mikhail A. Anisimov, and Frédéric Caupin. Two-structure thermodynamics for the TIP4p/2005 model of water covering supercooled and deeply stretched regions. *The Journal of Chemical Physics*, 146(3):034502, 2017.

[81] Mikhail A. Anisimov, Michal Duška, Frédéric Caupin, Lauren E. Amrhein, Amanda Rosenbaum, and Richard J. Sadus. Thermodynamics of fluid polyamorphism. *Physical Review X*, 8(1):011004–011021, 2018.

[82] Hajime Tanaka. Simple physical model of liquid water. *The Journal of Chemical Physics*, 112(2):799–809, 2000.

[83] V. Holten and M. A. Anisimov. Entropy-driven liquid–liquid separation in supercooled water. *Scientific Reports*, 2(1):713–719, 2012.

[84] M. Duška, J. Hrubý, F. Caupin, and M. A. Anisimov. Communication: Two-structure thermodynamics unifying all scenarios for water anomalies. *ArXiv e-prints*, August 2017.

[85] Vincent Holten, David T. Limmer, Valeria Molinero, and Mikhail A. Anisimov. Nature of the anomalies in the supercooled liquid state of the mW model of water. *The Journal of Chemical Physics*, 138(17):174501, 2013.

[86] Vincent Holten, Jeremy C. Palmer, Peter H. Poole, Pablo G. Debenedetti, and Mikhail A. Anisimov. Two-state thermodynamics of the ST2 model for supercooled water. *The Journal of Chemical Physics*, 140(10):104502, 2014.

[87] Valeria Molinero and Emily B. Moore. Water modeled as an intermediate element between carbon and silicon. *The Journal of Physical Chemistry B*, 113(13):4008–4016, 2009.

[88] Jibao Lu, Charusita Chakravarty, and Valeria Molinero. Relationship between the line of density anomaly and the lines of melting, crystallization, cavitation, and liquid spinodal in coarse-grained water models. *The Journal of Chemical Physics*, 144(23):234507, 2016.

[89] Debdas Dhabal, Charusita Chakravarty, Valeria Molinero, and Hemant K. Kashyap. Comparison of liquid-state anomalies in stillinger-weber models of water, silicon, and germanium. *The Journal of Chemical Physics*, 145(21):214502, 2016.

[90] Frank H. Stillinger and Aneesur Rahman. Improved simulation of liquid water by molecular dynamics. *The Journal of Chemical Physics*, 60(4):1545–1557, 1974.

[91] J. L. F. Abascal and C. Vega. A general purpose model for the condensed phases of water: TIP4p/2005. *The Journal of Chemical Physics*, 123(23):234505, 2005.

[92] Martin Lísal, Ivo Nezbeda, and William R. Smith. Vapor-liquid equilibria in five-site (TIP5p) models of water. *The Journal of Physical Chemistry B*, 108(22):7412–7414, 2004.

[93] *Liquid-Liquid Phase Transition in Supercooled Silicon.* John Wiley & Sons, Inc., 2013.

[94] Srikanth Sastry and C. Austen Angell. Liquid–liquid phase transition in supercooled silicon. *Nature Materials*, 2(11):739–743, 2003.

[95] G. Zhao, J. L. Yan, Y. J. Yu, M. C. Ding, X. G. Zhao, and H. Y. Wang. Relationship between structural order and water-like anomalies in metastable liquid silicon: Ab initio molecular dynamics. *Scientific Reports*, 7:39952, 2017.

[96] R. Chen, E. Lascaris, and J. C. Palmer. Liquid–liquid phase transition in an ionic model of silica. *The Journal of Chemical Physics*, 146(23):234503, 2017.

[97] Ivan Saika-Voivod, Francesco Sciortino, Tor Grande, and Peter H. Poole. Phase diagram of silica from computer simulation. *Physical Review E*, 70(6):061507–061514, 2004.

[98] M. H. Bhat, V. Molinero, E. Soignard, V. C. Solomon, S. Sastry, J. L. Yarger, and C. A. Angell. Vitrification of a monatomic metallic liquid. *Nature*, 448(7155):787–790, 2007.

[99] Srikanth Sastry, Pablo G. Debenedetti, Francesco Sciortino, and H. E. Stanley. Singularity-free interpretation of the thermodynamics of supercooled water. *Physical Review E*, 53(6):6144–6154, 1996.

[100] Peter H Poole, Ivan Saika-Voivod, and Francesco Sciortino. Density minimum and liquid–liquid phase transition. *Journal of Physics: Condensed Matter*, 17(43):431–437, 2005.

[101] Vincent Holten, Chen Qiu, Emmanuel Guillerm, Max Wilke, Jaroslav Rička, Martin Frenz, and Frédéric Caupin. Compressibility anomalies in stretched water and their interplay with density anomalies. *The Journal of Physical Chemistry Letters*, 8(22):5519–5522, 2017.

[102] John R Miller and Patrice Simon. Electrochemical capacitors for energy management. *Science Magazine*, 321(5889):651–652, 2008.

[103] Markus Mezger, Roland Roth, Heiko Schröder, Peter Reichert, Diego Pontoni, and Harald Reichert. Solid-liquid interfaces of ionic liquid solutionsinterfacial layering and bulk correlations. *The Journal of chemical physics*, 142(16):164707, 2015.

[104] Markus Mezger, Sebastian Schramm, Heiko Schröder, Harald Reichert, Moshe Deutsch, Emerson J De Souza, John S Okasinski, Benjamin M Ocko, Veijo Honkimäki, and Helmut Dosch. Layering of [bmim]+-based ionic liquids at a charged sapphire interface. *The Journal of chemical physics*, 131(9):094701, 2009.

[105] Robert Hayes, Natalia Borisenko, Matthew K Tam, Patrick C Howlett, Frank Endres, and Rob Atkin. Double layer structure of ionic liquids at the au (111) electrode interface: An atomic force microscopy investigation. *The Journal of Physical Chemistry C*, 115(14):6855–6863, 2011.

[106] Rob Atkin, Natalia Borisenko, Marcel Drüschler, Sherif Zein El Abedin, Frank Endres, Robert Hayes, Benedikt Huber, and Bernhard Roling. An in situ stm/afm and impedance spectroscopy study of the extremely pure 1-butyl-1-methylpyrrolidinium tris (pentafluoroethyl) trifluorophosphate/au (111) interface: Potential dependent solvation layers and the herringbone reconstruction. *Physical Chemistry Chemical Physics*, 13(15):6849–6857, 2011.

[107] Timo Carstens, Robert Hayes, Sherif Zein El Abedin, Brendan Corr, Grant B Webber, Natalia Borisenko, Rob Atkin, and Frank Endres. In situ stm, afm and dts study of the interface 1-hexyl-3-methylimidazolium tris (pentafluoroethyl) trifluorophosphate/au (111). *Electrochimica Acta*, 82:48–59, 2012.

[108] Céline Merlet, David T Limmer, Mathieu Salanne, René Van Roij, Paul A Madden, David Chandler, and Benjamin Rotenberg. The electric double layer has a life of its own. *The Journal of Physical Chemistry C*, 118(32):18291–18298, 2014.

[109] David T Limmer. Interfacial ordering and accompanying divergent capacitance at ionic liquid-metal interfaces. *Physical review letters*, 115(25):256102, 2015.

[110] M Arulepp, L Permann, J Leis, A Perkson, K Rumma, A Jänes, and E Lust. Influence of the solvent properties on the characteristics of a double layer capacitor. *Journal of Power Sources*, 133(2):320–328, 2004.

[111] Wenwen Liu, Xingbin Yan, Junwei Lang, and Qunji Xue. Effects of concentration and temperature of emimbf 4/acetonitrile electrolyte on the supercapacitive behavior of graphene nanosheets. *Journal of Materials Chemistry*, 22(18):8853–8861, 2012.

[112] Liis Siinor, Carolin Siimenson, Vladislav Ivaništšev, Karmen Lust, and Enn Lust. Influence of cation chemical composition and structure on the double layer capacitance for bi (111)— room temperature ionic liquid interface. *Journal of Electroanalytical Chemistry*, 668:30–36, 2012.

[113] David J Bozym, Betul Uralcan, David T Limmer, Michael A Pope, Nicholas J Szamreta, Pablo G Debenedetti, and Ilhan A Aksay. Anomalous capacitance maximum of the glassy carbon–ionic liquid interface through dilution with organic solvents. *The journal of physical chemistry letters*, 6(13):2644–2648, june 2015.

[114] Michael A. Pope and Ilhan A. Aksay. Four-fold increase in the intrinsic capacitance of graphene through functionalization and lattice disorder. *The Journal of Physical Chemistry C*, 119(35):20369–20378, 2015.

[115] M. Grousson, G. Tarjus, and P. Viot. Monte carlo study of the three-dimensional coulomb frustrated ising ferromagnet. *Physical Review E*, 64(3), 2001.

[116] David T Limmer, Céline Merlet, Mathieu Salanne, David Chandler, Paul A Madden, René Van Roij, and Benjamin Rotenberg. Charge fluctuations in nanoscale capacitors. *Physical review letters*, 111(10):106102, 2013.

[117] Durba Roy and Mark Maroncelli. An improved four-site ionic liquid model. *The Journal of Physical Chemistry B*, 114(39):12629–12631, 2010.

[118] Duncan MF Edwards, Paul A Madden, and Ian R McDonald. A computer simulation study of the dielectric properties of a model of methyl cyanide: I. the rigid dipole case. *Molecular physics*, 51(5):1141–1161, 1984.

[119] Milton W Cole and James R Klein. The interaction between noble gases and the basal plane surface of graphite. *Surface Science*, 124(2):547–554, 1983.

[120] Céline Merlet, Mathieu Salanne, and Benjamin Rotenberg. New coarse-grained models of imidazolium ionic liquids for bulk and interfacial molecular simulations. *The Journal of Physical Chemistry C*, 116(14):7687–7693, 2012.

[121] Clarisse Péan, Céline Merlet, Benjamin Rotenberg, Paul Anthony Madden, Pierre-Louis Taberna, Barbara Daffos, Mathieu Salanne, and Patrice Simon. On the dynamics of charging in nanoporous carbon-based supercapacitors. *ACS nano*, 8(2):1576–1583, 2014.

[122] Mark Maroncelli, Xin-Xing Zhang, Min Liang, Durba Roy, and Nikolaus P Ernsting. Measurements of the complete solvation response of coumarin 153 in ionic liquids and the accuracy of simple dielectric continuum predictions. *Faraday discussions*, 154:409–424, 2012.

[123] Stewart K Reed, Oliver J Lanning, and Paul A Madden. Electrochemical interface between an ionic liquid and a model metallic electrode. *The Journal of chemical physics*, 126(8):084704, 2007.

[124] J Ilja Siepmann and Michiel Sprik. Influence of surface topology and electrostatic potential on water/electrode systems. *The Journal of chemical physics*, 102(1):511–524, 1995.

[125] Todd R Gingrich and Mark Wilson. On the ewald summation of gaussian charges for the simulation of metallic surfaces. *Chemical Physics Letters*, 500(1):178–183, 2010.

[126] John Bertrand Johnson. Thermal agitation of electricity in conductors. *Physical review*, 32(1):97, 1928.

[127] Harry Nyquist. Thermal agitation of electric charge in conductors. *Physical review*, 32(1):110, 1928.

[128] Roger Parsons. The electrical double layer: Recent experimental and theoretical developments. *Chemical Reviews*, 90(5):813–826, 1990.

[129] Frank H. Stillinger and Ronald Lovett. General restriction on the distribution of ions in electrolytes. *The Journal of Chemical Physics*, 49(5):1991–1994, 1968.

[130] Daniel JVA dos Santos, Florian Muller-Plathe, and Volker C Weiss. Consistency of ion adsorption and excess surface tension in molecular dynamics simulations of aqueous salt solutions. *The Journal of Physical Chemistry C*, 112(49):19431–19442, 2008.

[131] Dale E Otten, Patrick R Shaffer, Phillip L Geissler, and Richard J Saykally. Elucidating the mechanism of selective ion adsorption to the liquid water surface. *Proceedings of the National Academy of Sciences*, 109(3):701–705, 2012.

[132] Xinmin Liu, Hang Li, Rui Li, Deti Xie, Jiupai Ni, and Laosheng Wu. Strong non-classical induction forces in ion-surface interactions: General origin of hofmeister effects. *Scientific reports*, 4, 2014.

[133] Pavel Jungwirth and Douglas J Tobias. Specific ion effects at the air/water interface. *Chemical reviews*, 106(4):1259–1281, 2006.

[134] Guang Feng, Xikai Jiang, Rui Qiao, and Alexei A. Kornyshev. Water in ionic liquids at electrified interfaces: The anatomy of electrosorption. *ACS Nano*, 8(11):11685–11694, 2014.

[135] Jianzhong Wu, Tao Jiang, De-en Jiang, Zhehui Jin, and Douglas Henderson. A classical density functional theory for interfacial layering of ionic liquids. *Soft Matter*, 7(23):11222–11231, 2011.

[136] Ryan Day and Angel E. García. Water penetration in the low and high pressure native states of ubiquitin. *Proteins: Struct., Funct., Bioinf.*, 70(4):1175–1184, 2007.

[137] Revanur Ravindra and Roland Winter. On the temperature-pressure free-energy landscape of proteins. *ChemPhysChem*, 4(4):359–365, 2003.

[138] Vadim V. Mozhaev, Karel Heremans, Johannes Frank, Patrick Masson, and Claude Balny. High pressure effects on protein structure and function. *Proteins: Struct., Funct., Genet.*, 24(1):81–91, 1996.

[139] K. Meister, S. Ebbinghaus, Y. Xu, J. G. Duman, A. DeVries, M. Gruebele, D. M. Leitner, and M. Havenith. Long-range protein-water dynamics in hyperactive insect antifreeze proteins. *Proc. Natl. Acad. Sci. U.S.A.*, 110(5):1617–1622, 2012.

[140] D. A. Ledward. Effects of pressure on protein structure. *High Press. Res.*, 19(1-6):1–10, 2000.

[141] Federica Piccirilli, Nicoletta Plotegher, Maria Grazia Ortore, Isabella Tessari, Marco Brucale, Francesco Spinozzi, Mariano Beltramini, Paolo Mariani, Valeria Militello, Stefano Lupi, and et al. High-pressure-driven reversible dissociation of α -synuclein fibrils reveals structural hierarchy. *Biophys. J.*, 113(8):1685–1696, 2017.

[142] Silvina Matysiak, Pablo G. Debenedetti, and Peter J. Rossky. Role of hydrophobic hydration in protein stability: A 3d water-explicit protein model exhibiting cold and heat denaturation. *J. Phys. Chem. B*, 116(28):8095–8104, 2012.

[143] Monika Davidovic, Carlos Mattea, Johan Qvist, and Bertil Halle. Protein cold denaturation as seen from the solvent. *J. Am. Chem. Soc.*, 131(3):1025–1036, 2009. PMID: 19115852.

[144] Charles Babu, Vincent Hilser, and Joshua JWand. Direct access to the cooperative substructure of proteins and the protein ensemble via cold denaturation. *Nat. Struct. Mol. Biol.*, 11:352, 2004.

[145] J. Jonas, L. Ballard, and D. Nash. High-resolution, high-pressure nmr studies of proteins. *Biophys. J.*, 75(1):445 – 452, 1998.

[146] Miquel Adrover, Veronica Esposito, Gabriel Martorell, Annalisa Pastore, and Piero Andrea Temussi. Understanding cold denaturation: The case study of yfh1. *J. Am. Chem. Soc.*, 132(45):16240–16246, 2010.

[147] R.L. Baldwin. How hofmeister ion interactions affect protein stability. *Biophys. J.*, 71(4):2056–2063, 1996.

[148] Yanjie Zhang, Steven Furyk, David E. Bergbreiter, and Paul S. Cremer. Specific ion effects on the water solubility of macromolecules: Pnipam and the hofmeister series. *J. Am. Chem. Soc.*, 127(41):14505–14510, 2005.

[149] Deepak R. Canchi and Angel E. García. Cosolvent effects on protein stability. *Annu. Rev. Phys. Chem.*, 64(1):273–293, 2013.

[150] Thomas Welton. Room-temperature inic liquids. solvents for synthesis and catalysis. *Chem. Rev.*, 99(8):2071–2084, 1999.

[151] Kenneth R. Seddon. Ionic liquids for clean technology. *J. Chem. Technol. Biotechnol.*, 68(4):351–356, 1997.

[152] Peter Wasserscheid and Thomas Welton, editors. *Ionic liquids in synthesis.* Wiley-VCH Verlag GmbH & Co. KGaA, 2007.

[153] Nolene Byrne, Li Min Wang, Jean Philippe Belieres, and C. Austen Angell. Reversible folding-unfolding, aggregation protection, and multi-year stabilization, in high concentration protein solutions, using ionic liquids. *ChemComm*, (26):2714–2716, 2007.

[154] Kyoko Fujita, Douglas R. MacFarlane, and Maria Forsyth. Protein solubilising and stabilising ionic liquids. *ChemComm*, (38):4804–4806, 2005.

[155] Muhammad Moniruzzaman, Noriho Kamiya , Kazunori Nakashima, and Masahiro Goto. Formation of reverse micelles in a room-temperature ionic liquid. *ChemPhysChem*, 9(5):689–692, 2008.

[156] Muhammad Moniruzzaman, Kazunori Nakashima, Noriho Kamiya, and Masahiro Goto. Recent advances of enzymatic reactions in ionic liquids. *Biochem. Eng. J.*, 48(3):295–314, 2010.

[157] Sandeep Kumar, Chung-Jung Tsai, and Ruth Nussinov. Factors enhancing protein thermostability. *Protein Eng. Des. Sel.*, 13(3):179–191, 2000.

[158] Yuqing Wu, Wei Li, Ce Zhou, Fuzhao Lu, Tianhui Gao, Yingchun Liu, Junli Cao, Yongmei Zhang, Yong Zhang, and Chenghua Zhou. Ketamine inhibits lipopolysaccharide-induced astrocytes activation by suppressing TLR4/NF-kb pathway. *Cell. Physiol. Biochem.*, 30(3):609–617, 2012.

[159] Ze-Lin Huang, Tao-Xiang Yang, Jian-Zi Huang, and Zhen Yang. Enzymatic production of biodiesel from millettia pinnata seed oil in ionic liquids. *Bioenergy Res.*, 7(4):1519–1528, 2014.

[160] Ying Wang, Mark Radosevich, Douglas Hayes, and Nicole Labbé. Compatible ionic liquid-cellulases system for hydrolysis of lignocellulosic biomass. *Biotechnol. Bioeng.*, 108(5):1042–1048, 2011.

[161] Feng Xu, Yong-Cheng Shi, and Donghai Wang. Enhanced production of glucose and xylose with partial dissolution of corn stover in ionic liquid, 1-ethyl-3-methylimidazolium acetate. *Bioresour. Technol.*, 114:720–724, 2012.

[162] Olga Ulbert, Tamás Fráter, Katalin Bélafi-Bakó, and László Gubicza. Enhanced enantioselectivity of candida rugosa lipase in ionic liquids as compared to organic solvents. *J. Mol. Catal., B Enzym.*, 31(1-3):39–45, 2004.

[163] M. Erbeldinger, A.J. Mesiano, and A.J. Russell. Enzymatic catalysis of formation of z-aspartame in ionic liquid - an alternative to enzymatic catalysis in organic solvents. *Biotechnol. Prog.*, 16(6):1129–1131, 2000.

[164] Rajan Patel, Meena Kumari, and Abbul Bashar Khan. Recent advances in the applications of ionic liquids in protein stability and activity: A review. *Appl. Biochem. Biotechnol.*, 172(8):3701–3720, 2014.

[165] Gloria D. Elliott, Regina Kemp, and Douglas R MacFarlane. The development of ionic liquids for biomedical applications - prospects and challenges. pages 95–105, 2009.

[166] Kim D. Collins and Michael W. Washabaugh. The hofmeister effect and the behaviour of water at interfaces. *Q. Rev. Biophys.*, 18(04):323–422, 1985.

[167] Werner Kunz, Pierandrea Lo Nostro, and Barry W. Ninham. The present state of affairs with hofmeister effects. *Curr. Opin. Colloid Interface Sci.*, 9(1):1–18, 2004.

[168] S. Finet, F. Skouri-Panet, M. Casselyn, F. Bonneté, and A. Tardieu. The hofmeister effect as seen by SAXS in protein solutions. *Curr. Opin. Colloid Interface Sci.*, 9(1-2):112–116, 2004.

[169] Y. Zhang and P. S. Cremer. The inverse and direct hofmeister series for lysozyme. *Proc. Natl. Acad. Sci. U.S.A.*, 106(36):15249–15253, 2009.

[170] Erik M. Nordwald and Joel L. Kaar. Stabilization of enzymes in ionic liquids via modification of enzyme charge. *Biotechnol. Bioeng.*, 110(9):2352–2360, 2013.

[171] Diana Constantinescu, Hermann Weingrtner, and Christian Herrmann. Denaturierung von proteinen durch ionische flssigkeiten und hofmeister-reihe: eine fallstudie wssrigerlsungen von ribonuclease a. *Angew. Chem. Int. Ed.*, 119(46):9044–9046, 2007.

[172] Meena Kumari, Neeraj Dohare, Neha Maurya, Ravins Dohare, and Rajan Patel. Effect of 1-methyl-3-octyleimmidazolium chloride on the stability and activity of lysozyme: a spectroscopic and molecular dynamics studies. *J. Biomol. Struct. Dyn.*, 35(9):2016–2030, 2016.

[173] Vance W. Jaeger and Jim Pfaendtner. Structure, dynamics, and activity of xylanase solvated in binary mixtures of ionic liquid and water. *ACS Chem. Biol.*, 8(6):1179–1186, 2013.

[174] Erik M. Nordwald, Roman Brunecky, Michael E. Himmel, Gregg T. Beckham, and Joel L. Kaar. Charge engineering of cellulases improves ionic liquid tolerance and reduces lignin inhibition. *Biotechnol. Bioeng.*, 111(8):1541–1549, 2014.

[175] Vance Jaeger, Patrick Burney, and Jim Pfaendtner. Comparison of three ionic liquid-tolerant cellulases by molecular dynamics. *Biophys. J.*, 108(4):880–892, 2015.

[176] Patrick R. Burney, Erik M. Nordwald, Katie Hickman, Joel L. Kaar, and Jim Pfaendtner. Molecular dynamics investigation of the ionic liquid/enzyme interface: Application to engineering enzyme surface charge. *Proteins: Struct., Funct., Bioinf.*, 83(4):670–680, 2015.

[177] Patrick R. Burney and Jim Pfaendtner. Structural and dynamic features of candida rugosa lipase 1 in water, octane, toluene, and ionic liquids BMIM-PF_6 and BMIM-NO_3, journal = J. Phys. Chem. B. 117(9):2662–2670, 2013.

[178] Paul W. Wolski, Craig M. Dana, Douglas S. Clark, and Harvey W. Blanch. Engineering ionic liquid-tolerant cellulases for biofuels production. *Protein Eng. Des. Sel.*, 29(4):117–122, 2016.

[179] Lucas B. Johnson, Lucas P. Gintner, Sehoo Park, and Christopher D. Snow. Discriminating between stabilizing and destabilizing protein design mutations via recombination and simulation. *Protein Eng. Des. Sel.*, 28(8):259–267, 2015.

[180] Lucas B. Johnson and Christopher D. Snow. Molecular dynamics simulations of cellulase homologs in aqueous 1-ethyl-3-methylimidazolium chloride. *J. Biomol. Struct. Dyn.*, 35(9):1990–2002, 2016.

[181] Meena Kumari, Jitendra Kumar Maurya, Upendra Kumar Singh, Abbul Bashar Khan, Maroof Ali, Prashant Singh, and Rajan Patel. Spectroscopic and docking studies on the interaction between pyrrolidinium based ionic liquid and bovine serum albumin. *Spectrochim. Acta A*, 124:349–356, 2014.

[182] Meena Kumari, Jitendra Kumar Maurya, Munazzah Tasleem, Prashant Singh, and Rajan Patel. Probing HSA-ionic liquid interactions by spectroscopic and molecular docking methods. *J. Photochem. Photobiol.*, 138:27–35, 2014.

[183] Vance W. Jaeger and Jim Pfaendtner. Destabilization of human serum albumin by ionic liquids studied using enhanced molecular dynamics simulations. *J. Phys. Chem. B*, 120(47):12079–12087, 2016.

[184] Vance Jaeger, Patrick Burney, and Jim Pfaendtner. Comparison of three ionic liquid-tolerant cellulases by molecular dynamics. *Biophys. J.*, 108(4):880–892, 2015.

[185] Kinetics and mechanism of ionic-liquid induced protein unfolding: application to the model protein hp35. *Mol. Syst. Des. Eng.*, 1(3):382–390, 2016.

[186] Angel E. Garcia, Henry Herce, and Dietmar Paschek. Simulations of temperature and pressure unfolding of peptides and proteins with replica exchange molecular dynamics. volume 2 of *Annual Reports in Computational Chemistry*, pages 83–95. Elsevier, 2006.

[187] Changwon Yang, Soonmin Jang, and Youngshang Pak. A fully atomistic computer simulation study of cold denaturation of a β-hairpin. *Nat. Commun.*, 5:5773, 2014.

[188] Dietmar Paschek and Angel E. García. Reversible temperature and pressure denaturation of a protein fragment: a replica exchange molecular dynamics simulation study. *Phys. Rev. Lett.*, 93:238105, 2004.

[189] D. Paschek, S. Gnanakaran, and A. E. Garcia. Simulations of the pressure and temperature unfolding of an α-helical peptide. *Proc. Natl. Acad. Sci. U.S.A.*, 102(19):6765–6770, 2005.

[190] Dietmar Paschek, Ryan Day, and Angel E. García. Influence of water–protein hydrogen bonding on the stability of trp-cage miniprotein. a comparison between the TIP3p and TIP4p-ew water models. *Phys. Chem. Chem. Phys.*, 13(44):19840, 2011.

[191] Ryan Day, Dietmar Paschek, and Angel E. Garcia. Microsecond simulations of the folding/unfolding thermodynamics of the trp-cage miniprotein. *Proteins: Struct., Funct., Bioinf.*, 78(8):1889–1899, 2010.

[192] Jan Heyda, Milan Koek, Lucie Bednrova, Gary Thompson, Jan Konvalinka, Ji Vondrek, and Pavel Jungwirth. Urea and guanidinium induced denaturation of a trp-cage miniprotein. *J. Phys. Chem. B*, 115(28):8910–8924, 2011.

[193] Harold W. Hatch, Frank H. Stillinger, and Pablo G. Debenedetti. Computational study of the stability of the miniprotein trp-cage, the gb1 -hairpin, and the ak16 peptide, under negative pressure. *J. Phys. Chem. B*, 118(28):7761–7769, 2014.

[194] Robert B. Best and Jeetain Mittal. Protein simulations with an optimized water model: cooperative helix formation and temperature-induced unfolded state collapse. *J. Phys. Chem. B*, 114(46):14916–14923, 2010.

[195] Yong Duan, Chun Wu, Shibasish Chowdhury, Mathew C. Lee, Guoming Xiong, Wei Zhang, Rong Yang, Piotr Cieplak, Ray Luo, and et al. Taisung Lee. A

point-charge force field for molecular mechanics simulations of proteins based on condensed-phase quantum mechanical calculations. *J. Comput. Chem.*, 24(16):1999–2012, 2003.

[196] Berk Hess. P-LINCS: A parallel linear constraint solver for molecular simulation. *J. Chem. Theory Comput.*, 4(1):116–122, 2008.

[197] K. Anton Feenstra, Berk Hess, and Herman J. C. Berendsen. Improving efficiency of large time-scale molecular dynamics simulations of hydrogen-rich systems. *J. Comput. Chem.*, 20(8):786–798, 1999.

[198] H. J. C. Berendsen, J. P. M. Postma, W. F. van Gunsteren, A. DiNola, and J. R. Haak. Molecular dynamics with coupling to an external bath. *J. Chem. Phys.*, 81(8):3684–3690, 1984.

[199] Shuichi Miyamoto and Peter A. Kollman. Settle: An analytical version of the SHAKE and RATTLE algorithm for rigid water models. *J. Comput. Chem.*, 13(8):952–962, 1992.

[200] Ulrich Essmann, Lalith Perera, Max L. Berkowitz, Tom Darden, Hsing Lee, and Lee G. Pedersen. A smooth particle mesh ewald method. *J. Chem. Phys.*, 103(19):8577–8593, 1995.

[201] Shuichi Nosé. A unified formulation of the constant temperature molecular dynamics methods. *J. Chem. Phys.*, 81(1):511–519, 1984.

[202] William G. Hoover. Canonical dynamics: equilibrium phase-space distributions. *Phys. Rev. A*, 31(3):1695–1697, 1985.

[203] M. Parrinello and A. Rahman. Polymorphic transitions in single crystals: A new molecular dynamics method. *J. Appl. Phys.*, 52(12):7182–7190, 1981.

[204] Shuichi Nosé and M.L. Klein. Constant pressure molecular dynamics for molecular systems. *Mol. Phys.*, 50(5):1055–1076, 1983.

[205] H. Flyvbjerg and H. G. Petersen. Error estimates on averages of correlated data. *J. Chem. Phys.*, 91(1):461–466, 1989.

[206] David van der Spoel, Paul J. van Maaren, Per Larsson, and Nicusor Timneanu. Thermodynamics of hydrogen bonding in hydrophilic and hydrophobic media. *J. Phys. Chem. B*, 110(9):4393–4398, 2006.

[207] M.L. Anson. Protein denaturation and the properties of protein groups. 2:361–386, 1945.

[208] Pedro Lozano, Rungtiwa Piamtongkam, Kevin Kohns, Teresa De Diego, Michel Vaultier, and Jos? L. Iborra. Ionic liquids improve citronellyl ester synthesis catalyzed by immobilized candida antarctica lipase b in solvent-free media. *Green Chem.*, 9(7):780, 2007.

[209] Jia Lin Huang, Michael E. Noss, Karson M. Schmidt, Leigh Murray, and Michelle R. Bunagan. The effect of neat ionic liquid on the folding of short peptides. *ChemComm*, 47(28):8007–8009, 2011.

[210] John F. Brandts. The thermodynamics of protein denaturation. i. the denaturation of chymotrypsinogen. *J. Am. Chem. Soc.*, 86(20):4291–4301, 1964.

[211] Mary Struthers, Jennifer J Ottesen, and Barbara Imperiali. Design and NMR analysis of compact, independently folded BBA motifs. *Fold. Des.*, 3(2):95–103, 1998.

[212] Xavier Daura, Karl Gademann, Bernhard Jaun, Dieter Seebach, Wilfred F. van Gunsteren, and Alan E. Mark. Peptide folding: When simulation meets experiment. *Angewandte Chemie International Edition*, 38(1/2):236–240, 1999.

[213] Ken A. Dill. Theory for the folding and stability of globular proteins. *Biochemistry*, 24(6):1501–1509, 1985.

[214] Gunda Panick, Gediminas J. A. Vidugiris, Ralf Malessa, G. Rapp, Roland Winter, and Catherine A. Royer. Exploring the temperature-pressure phase diagram of staphylococcal nuclease. *Biochemistry*, 38(13):4157–4164, 1999.

[215] J. Wiedersich, S. Kohler, A. Skerra, and J. Friedrich. Temperature and pressure dependence of protein stability: The engineered fluorescein-binding lipocalin FluA shows an elliptic phase diagram. *Proceedings of the National Academy of Sciences*, 105(15):5756–5761, 2008.

[216] Adam Zipp and Walter Kauzmann. Pressure denaturation of metmyoglobin. *Biochemistry*, 12(21):4217–4228, 1973.

[217] John F. Brandts, Robert J. Oliveira, and Chester Westort. Thermodynamics of protein denaturation. effect of pressure on the denaturation on ribonuclease a. *Biochemistry*, 9(4):1038–1047, 1970.

[218] K Heremans. High pressure effects on proteins and other biomolecules. *Annual Review of Biophysics and Bioengineering*, 11(1):1–21, 1982.

[219] D. Paschek, S. Hempel, and A. E. Garcia. Computing the stability diagram of the trp-cage miniprotein. *Proceedings of the National Academy of Sciences*, 105(46):17754–17759, 2008.

[220] J. Roche, J. A. Caro, D. R. Norberto, P. Barthe, C. Roumestand, J. L. Schlessman, A. E. Garcia, B. Garcia-Moreno E., and C. A. Royer. Cavities determine the pressure unfolding of proteins. *Proceedings of the National Academy of Sciences*, 109(18):6945–6950, 2012.

[221] Soichiro Kitazawa, Martin J. Fossat, Scott A. McCallum, Angel E. Garcia, and Catherine A. Royer. NMR and computation reveal a pressure-sensitive folded conformation of trp-cage. *The Journal of Physical Chemistry B*, 121(6):1258–1267, 2017.

[222] Harold W. Hatch, Frank H. Stillinger, and Pablo G. Debenedetti. Computational study of the stability of the miniprotein trp-cage, the GB1 β-hairpin, and the AK16 peptide, under negative pressure. *The Journal of Physical Chemistry B*, 118(28):7761–7769, 2014.

[223] Rainer Jaenicke. Protein stability and molecular adaptation to extreme conditons. *European Journal of Biochemistry*, 202(3):715–728, 1991.

[224] S N Timasheff. The control of protein stability and association by weak interactions with water: How do solvents affect these processes? *Annual Review of Biophysics and Biomolecular Structure*, 22(1):67–97, 1993.

[225] G. Somero. Proteins and temperature. *Annual Review of Physiology*, 57(1):43–68, 1995.

[226] G. Somero. Adaptations to high hydrostatic pressure. *Annual Review of Physiology*, 54(1):557–577, 1992.

[227] Débora Foguel and Jerson L. Silva. New insights into the mechanisms of protein misfolding and aggregation in amyloidogenic diseases derived from pressure studies. *Biochemistry*, 43(36):11361–11370, 2004.

[228] Wei Wang. Lyophilization and development of solid protein pharmaceuticals. *International Journal of Pharmaceutics*, 203(1-2):1–60, 2000.

[229] F. Franks and R. H. M. Hatley. Stability of proteins at subzero temperatures: thermodynamics and some ecological consequences. *Pure Appl. Chem.*, 63(10), 1991.

[230] Ken A. Dill. Dominant forces in protein folding. *Biochemistry*, 29(31):7133–7155, 1990.

[231] W. Kauzmann. Some factors in the interpretation of protein denaturation. In *Advances in Protein Chemistry*, pages 1–63. Elsevier, 1959.

[232] George I. Makhatadze and Peter L. Privalov. Energetics of protein structure. In *Advances in Protein Chemistry*, pages 307–425. Elsevier, 1995.

[233] Marie-Claire Bellissent-Funel, Ali Hassanali, Martina Havenith, Richard Henchman, Peter Pohl, Fabio Sterpone, David van der Spoel, Yao Xu, and Angel E Garcia. Water determines the structure and dynamics of proteins. *Chemical Reviews*, 116(13):7673–7697, 2016.

[234] S. A. Hawley. Reversible pressure-temperature denaturation of chymotrypsinogen. *Biochemistry*, 10(13):2436–2442, 1971.

[235] Heinz Herberhold and Roland Winter. Temperature- and pressure-induced unfolding and refolding of ubiquitin: a static and kinetic fourier transform infrared spectroscopy study†. *Biochemistry*, 41(7):2396–2401, 2002.

[236] Harald Lesch, Hans Stadlbauer, Josef Friedrich, and Jane M. Vanderkooi. Stability diagram and unfolding of a modified cytochrome c: What happens in the transformation regime? *Biophysical Journal*, 82(3):1644–1653, 2002.

[237] Wolfgang Doster and Josef Friedrich. Pressure-temperature phase diagrams of proteins. In *Protein Folding Handbook*, pages 99–126. Wiley-VCH Verlag GmbH, 2008.

[238] Charles A. English and Angel E. García. Folding and unfolding thermodynamics of the TC10b trp-cage miniprotein. *Physical Chemistry Chemical Physics*, 16(7):2748, 2014.

[239] P.L. Privalov, E.I. Tiktopulo, S.Yu. Venyaminov, Yu.V. Griko, G.I. Makhatadze, and N.N. Khechinashvili. Heat capacity and conformation of proteins in the denatured state. *Journal of Molecular Biology*, 205(4):737–750, 1989.

[240] G.I. Makhatadze and P.L. Privalov. Heat capacity of proteins. *Journal of Molecular Biology*, 213(2):375–384, 1990.

[241] Ross H. M. Hatley and Felix Franks. Cold destabilisation of enzymes. *Faraday Discussions*, 93:249, 1992.

[242] Ken A. Dill, Darwin O. V. Alonso, and Karen Hutchinson. Thermal stabilities of globular proteins. *Biochemistry*, 28(13):5439–5449, 1989.

[243] Chung-Jung Tsai, Jacob V. Maizel, and Ruth Nussinov. The hydrophobic effect: A new insight from cold denaturation and a two-state water structure. *Critical Reviews in Biochemistry and Molecular Biology*, 37(2):55–69, 2002.

[244] Cristiano L. Dias, Tapio Ala-Nissila, Mikko Karttunen, Ilpo Vattulainen, and Martin Grant. Microscopic mechanism for cold denaturation. *Physical Review Letters*, 100(11), 2008.

[245] Carlos F. Lopez, Richard K. Darst, and Peter J. Rossky. Mechanistic elements of protein cold denaturation. *The Journal of Physical Chemistry B*, 112(19):5961–5967, 2008.

[246] Arieh Ben-Naim. Theory of cold denaturation of proteins. *Advances in Biological Chemistry*, 03(01):29–39, 2013.

[247] N. Vajpai, L. Nisius, M. Wiktor, and S. Grzesiek. High-pressure NMR reveals close similarity between cold and alcohol protein denaturation in ubiquitin. *Proc. Natl. Acad. Sci. U.S.A.*, 110(5):E368–E376, 2013.

[248] Annalisa Pastore, Stephen R. Martin, Anastasia Politou, Kalyan C. Kondapalli, Timothy Stemmler, and Piero A. Temussi. Unbiased cold denaturation: low- and high-temperature unfolding of yeast frataxin under physiological conditions. *J. Am. Chem. Soc.*, 129(17):5374–5375, 2007.

[249] Ginka S. Buchner, Natalie Shih, Amy E. Reece, Stephan Niebling, and Jan Kubelka. Unusual cold denaturation of a small protein domain. *Biochemistry*, 51(33):6496–6498, 2012.

[250] Peter L. Privalov. Cold denaturation of proteins. *Critical Reviews in Biochemistry and Molecular Biology*, 25(4):281–306, 1990.

[251] Wade D. Van Horn, Alana K. Simorellis, and Peter F. Flynn. Low-temperature studies of encapsulated proteins. *Journal of the American Chemical Society*, 127(39):13553–13560, 2005.

[252] Bryan A. Patel, Pablo G. Debenedetti, Frank H. Stillinger, and Peter J. Rossky. A water-explicit lattice model of heat-, cold-, and pressure-induced protein unfolding. *Biophysical Journal*, 93(12):4116–4127, 2007.

[253] K Akimoto, M Hattori, K Uematsu, and C Kato. The deepest living foraminifera, challenger deep, mariana trench. *Marine Micropaleontology*, 42(1-2):95–97, may 2001.

[254] Werner W. Streicher and George I. Makhatadze. Unfolding thermodynamics of trp-cage, a 20 residue miniprotein, studied by differential scanning calorimetry and circular dichroism spectroscopy. *Biochemistry*, 46(10):2876–2880, 2007.

[255] H.J.C. Berendsen, D. van der Spoel, and R. van Drunen. GROMACS: A message-passing parallel molecular dynamics implementation. *Computer Physics Communications*, 91(1-3):43–56, 1995.

[256] Berk Hess, Carsten Kutzner, David van der Spoel, and Erik Lindahl. GROMACS 4: algorithms for highly efficient, load-balanced, and scalable molecular simulation. *Journal of Chemical Theory and Computation*, 4(3):435–447, 2008.

[257] William Humphrey, Andrew Dalke, and Klaus Schulten. VMD: Visual molecular dynamics. *Journal of Molecular Graphics*, 14(1):33–38, 1996.

[258] R. J. Speedy and C. A. Angell. Isothermal compressibility of supercooled water and evidence for a thermodynamic singularity at -45c. *The Journal of Chemical Physics*, 65(3):851–858, 1976.

[259] C. A. Angell, W. J. Sichina, and M. Oguni. Heat capacity of water at extremes of supercooling and superheating. *The Journal of Physical Chemistry*, 86(6):998–1002, 1982.

[260] D. E. Hare and C. M. Sorensen. Densities of supercooled h2o and d2o in 25 glass capillaries. *The Journal of Chemical Physics*, 84(9):5085–5089, 1986.

[261] Peter H. Poole, Francesco Sciortino, Ulrich Essmann, and H. Eugene Stanley. Phase behaviour of metastable water. *Nature*, 360(6402):324–328, 1992.

[262] Osamu Mishima and H. Eugene Stanley. Decompression-induced melting of ice IV and the liquid–liquid transition in water. *Nature*, 392(6672):164–168, 1998.

[263] Alan K. Soper and Maria Antonietta Ricci. Structures of high-density and low-density water. *Physical Review Letters*, 84(13):2881–2884, 2000.

[264] Hajime Tanaka. Simple view of waterlike anomalies of atomic liquids with directional bonding. *Physical Review B*, 66(6):064202–064209, 2002.

[265] Frédéric Caupin. Liquid-vapor interface, cavitation, and the phase diagram of water. *Physical Review E*, 71(5):051605–051609, 2005.

[266] Frédéric Caupin and Eric Herbert. Cavitation in water: a review. *Comptes Rendus Physique*, 7(9-10):1000–1017, nov 2006.

[267] Katrin Winkel, Michael S. Elsaesser, Erwin Mayer, and Thomas Loerting. Water polyamorphism: Reversibility and (dis)continuity. *The Journal of Chemical Physics*, 128(4):044510, 2008.

[268] K. Stokely, M. G. Mazza, H. E. Stanley, and G. Franzese. Effect of hydrogen bond cooperativity on the behavior of water. *Proceedings of the National Academy of Sciences*, 107(4):1301–1306, 2010.

[269] Giancarlo Franzese and H Stanley. Understanding the unusual properties of water. In *Water and Life*, pages 101–117. CRC Press, 2010.

[270] G. N. I. Clark, G. L. Hura, J. Teixeira, A. K. Soper, and T. Head-Gordon. Small-angle scattering and the structure of ambient liquid water. *Proceedings of the National Academy of Sciences*, 107(32):14003–14007, 2010.

[271] Emily B. Moore and Valeria Molinero. Structural transformation in supercooled water controls the crystallization rate of ice. *Nature*, 479(7374):506–508, 2011.

[272] C. Austen Angell. Two phases? *Nature Materials*, 13(7):673–675, 2014.

[273] C. Qiu, Y. Krger, M. Wilke, D. Marti, J. Rička, and M. Frenz. Exploration of the phase diagram of liquid water in the low-temperature metastable region using synthetic fluid inclusions. *Physical Chemistry Chemical Physics*, 18(40):28227–28241, 2016.

[274] Y. Elia Altabet, Rakesh S. Singh, Frank H. Stillinger, and Pablo G. Debenedetti. Thermodynamic anomalies in stretched water. *Langmuir*, 33(42):11771–11778, 2017.

[275] M. A. Morales, C. Pierleoni, E. Schwegler, and D. M. Ceperley. Evidence for a first-order liquid-liquid transition in high-pressure hydrogen from ab initio simulations. *Proceedings of the National Academy of Sciences*, 107(29):12799–12803, 2010.

[276] Mohamed Zaghoo, Ashkan Salamat, and Isaac F. Silvera. Evidence of a first-order phase transition to metallic hydrogen. *Physical Review B*, 93(15):155128–155134, 2016.

[277] Philip Dalladay-Simpson, Ross T. Howie, and Eugene Gregoryanz. Evidence for a new phase of dense hydrogen above 325 gigapascals. *Nature*, 529(7584):63–67, 2016.

[278] Vishwas V. Vasisht and Srikanth Sastry. Liquid-liquid phase transition in supercooled silicon. In *Liquid Polymorphism*, pages 463–517. John Wiley & Sons, Inc., 2013.

[279] James N. Glosli and Francis H. Ree. Liquid-liquid phase transformation in carbon. *Physical Review Letters*, 82(23):4659–4662, 1999.

[280] A. Cadien, Q. Y. Hu, Y. Meng, Y. Q. Cheng, M. W. Chen, J. F. Shu, H. K. Mao, and H. W. Sheng. First-order liquid-liquid phase transition in cerium. *Physical Review Letters*, 110(12):125503–125507, 2013.

[281] Yoshinori Katayama, Takeshi Mizutani, Wataru Utsumi, Osamu Shimomura, Masaaki Yamakata, and Ken ichi Funakoshi. A first-order liquid–liquid phase transition in phosphorus. *Nature*, 403(6766):170–173, 2000.

[282] K. Amann-Winkel, C. Gainaru, P. H. Handle, M. Seidl, H. Nelson, R. Bohmer, and T. Loerting. Waters second glass transition. *Proceedings of the National Academy of Sciences*, 110(44):17720–17725, 2013.

[283] Frank Smallenburg, Peter H. Poole, and Francesco Sciortino. Phase diagram of the ST2 model of water. *Molecular Physics*, 113(17-18):2791–2798, 2015.

[284] Jeremy C. Palmer, Fausto Martelli, Yang Liu, Roberto Car, Athanassios Z. Panagiotopoulos, and Pablo G. Debenedetti. Metastable liquid–liquid transition in a molecular model of water. *Nature*, 510(7505):385–388, 2014.

[285] Peter H. Poole, Richard K. Bowles, Ivan Saika-Voivod, and Francesco Sciortino. Free energy surface of ST2 water near the liquid-liquid phase transition. *The Journal of Chemical Physics*, 138(3):034505, 2013.

[286] Yang Liu, Jeremy C. Palmer, Athanassios Z. Panagiotopoulos, and Pablo G. Debenedetti. Liquid-liquid transition in ST2 water. *The Journal of Chemical Physics*, 137(21):214505, 2012.

[287] Jeremy C. Palmer, Roberto Car, and Pablo G. Debenedetti. The liquid–liquid transition in supercooled ST2 water: a comparison between umbrella sampling and well-tempered metadynamics. *Faraday Discussions*, 167:77, 2013.

[288] Y. Li, J. Li, and F. Wang. Liquid-liquid transition in supercooled water suggested by microsecond simulations. *Proceedings of the National Academy of Sciences*, 110(30):12209–12212, 2013.

[289] Rakesh S. Singh, John W. Biddle, Pablo G. Debenedetti, and Mikhail A. Anisimov. Two-state thermodynamics and the possibility of a liquid-liquid phase transition in supercooled TIP4p/2005 water. *The Journal of Chemical Physics*, 144(14):144504, 2016.

[290] Yicun Ni and J. L. Skinner. Evidence for a liquid-liquid critical point in supercooled water within the e3b3 model and a possible interpretation of the kink in the homogeneous nucleation line. *The Journal of Chemical Physics*, 144(21):214501, 2016.

[291] H. Pathak, J. C. Palmer, D. Schlesinger, K. T. Wikfeldt, J. A. Sellberg, L. G. M. Pettersson, and A. Nilsson. The structural validity of various thermodynamical models of supercooled water. *The Journal of Chemical Physics*, 145(13):134507, 2016.

[292] Limei Xu, Pradeep Kumar, S. V. Buldyrev, S.-H. Chen, P. H. Poole, F. Sciortino, and H. E. Stanley. Relation between the widom line and the dynamic crossover in systems with a liquid–liquid phase transition. *Proceedings of the National Academy of Sciences*, 102(46):16558–16562, 2005.

[293] Jeremy C. Palmer, Peter H. Poole, Francesco Sciortino, and Pablo G. Debenedetti. Advances in computational studies of the liquidliquid transition in water and water-like models. *Chemical Reviews*, 118(18):9129–9151, 2018.

[294] Miguel A. González, Chantal Valeriani, Frédéric Caupin, and José L. F. Abascal. A comprehensive scenario of the thermodynamic anomalies of water using the TIP4p/2005 model. *The Journal of Chemical Physics*, 145(5):054505, 2016.

[295] Francesco Sciortino, Ivan Saika-Voivod, and Peter H. Poole. Study of the ST2 model of water close to the liquid–liquid critical point. *Physical Chemistry Chemical Physics*, 13(44):19759, 2011.

[296] P. G. Debenedetti. *Metastable Liquids. Concepts and Principles.* Princeton University Press, 1996.

[297] E. A. Guggenheim. The principle of corresponding states. *The Journal of Chemical Physics*, 13(7):253–261, 1945.

[298] Thomas W. Leland and Patsy S. Chappelear. The corresponding states principle - a review of the current theory and practice, journal = Industrial & Engineering Chemistry. 60(7):15–43, 1968.

[299] John Biddle. In *Two-State Thermodynamics of Supercooled Water*, pages 233–235. Doctoral dissertation, University of Maryland, College Park, 2016.

[300] D. A. Fuentevilla and M. A. Anisimov. Scaled equation of state for supercooled water near the liquid-liquid critical point. *Physical Review Letters*, 97(19), 2006.

[301] Osamu Mishima. Volume of supercooled water under pressure and the liquid-liquid critical point. *The Journal of Chemical Physics*, 133(14):144503, 2010.

[302] Nicholas J. Hestand and J. L. Skinner. Perspective: Crossing the widom line in no man's land: Experiments, simulations, and the location of the liquid-liquid critical point in supercooled water. *The Journal of Chemical Physics*, 149(14):140901, 2018.

[303] Georg Menzl, Miguel A. Gonzalez, Philipp Geiger, Frédéric Caupin, José L. F. Abascal, Chantal Valeriani, and Christoph Dellago. Molecular mechanism for cavitation in water under tension. *Proceedings of the National Academy of Sciences*, 113(48):13582–13587, nov 2016.

[304] Frank Smallenburg, Laura Filion, and Francesco Sciortino. Erasing no-man's land by thermodynamically stabilizing the liquid–liquid transition in tetrahedral particles. *Nature Physics*, 10(9):653–657, jul 2014.

[305] Betul Uralcan, Ilhan A. Aksay, Pablo G. Debenedetti, and David T. Limmer. Concentration fluctuations and capacitive response in dense ionic solutions. *The Journal of Physical Chemistry Letters*, 7(13):2333–2338, 2016.